Waveguide quantum electrodynamics: Collective radiance and photon-photon correlations

Alexandra S. Sheremet[*]

Russian Quantum Center, Skolkovo, 143025 Moscow, Russia
and Department of Physics and Engineering, ITMO University, St. Petersburg 197101, Russia

Mihail I. Petrov and Ivan V. Iorsh●

Department of Physics and Engineering, ITMO University, St. Petersburg 197101, Russia

Alexander V. Poshakinskiy

Ioffe Institute, St. Petersburg 194021, Russia

Alexander N. Poddubny●[†]

Department of Physics of Complex Systems, Weizmann Institute of Science,
Rehovot 7610001, Israel

(published 10 March 2023)

This review describes the emerging field of waveguide quantum electrodynamics concerned with the interaction of photons propagating in a waveguide with localized quantum emitters. The collective emitter-photon interactions can lead to both enhanced and suppressed coupling compared to the case of independent emitters. Here the focus is on guided photons and ordered emitter arrays, manifesting superradiant and subradiant states, bound photon states, and quantum correlations with promising quantum information applications. Recent groundbreaking experiments performed with different quantum platforms, including cold atoms, superconducting qubits, semiconductor quantum dots, and quantum solid-state defects, are highlighted. The review also provides a comprehensive introduction to theoretical techniques to study the interactions and dynamics of these emitters and the photons in the waveguide.

CONTENTS

[*]a.sheremet@metalab.ifmo.ru
[†]a.poddubny@fastmail.com

I. INTRODUCTION

Atomic systems are well known to manifest collective effects in their interaction with light (Guerin, Rouabah, and Kaiser, 2017). If the light wavelength is much larger than the interatomic distance, atoms can interact with light in a coherent and collective way; i.e., emitted photons experience interference that results in enhancement or suppression of the spontaneous emission. This interference is manifested both in a single-photon regime and in a nonlinear regime, when a large number of atoms is excited. It is most easily understood in the case of a single resonant excitation of $N = 2$ closely spaced atoms by one photon. Namely, the electromagnetic field reradiated by one atom will act upon the other one. This photon-mediated coupling results in the formation of two collective atomic states: the superradiant one and the subradiant one. The superradiant (symmetric) state corresponds to in-phase oscillations of the two atomic dipole moments and radiates twice as fast. Conversely, the subradiant (antisymmetric) state has atomic dipole moments with opposite phases and corresponds to the reduced emission rate. Such enhanced and suppressed spontaneous emission for two ions in free space was observed for the first time in 1996 (DeVoe and Brewer, 1996).

A paradigmatic model for collective emission enhancement, superradiance, is the Dicke model (Dicke, 1954), which describes photon radiation from a cloud of initially fully excited atoms when the cloud size is much smaller than the photon wavelength. Because of collective effects, the excited N-atom cloud emits light as a high intensity pulse with a characteristic time shorter than that of an individual atom by a factor of N and an intensity that is larger by a factor of $\sim N^2$ (Dicke, 1954; Gross and Haroche, 1982; Benedict *et al.*, 2018). This is the essence of Dicke superradiance. Such collective radiation is drastically different from the independent behavior expected for a dilute ensemble of atoms, where the spontaneous emission rate remains unchanged and the intensity scales $\propto N$.

However, in realistic atomic clouds collective effects are hard to observe because of the disorder that leads to random phases for propagating photons and masks the collective interference. In this regard, ordered arrays are of special interest. Recently the rapid development of quantum technologies (Hammerer, Sørensen, and Polzik, 2010; Chang, Vuletić, and Lukin, 2014) has led to the emergence of novel experimental platforms where regular arrays of various emitters are controllably coupled to a few photons propagating in a waveguide. These systems can be based on natural or artificial atoms, such as superconducting qubits or solid-state quantum dots and defects, and can employ different types of optical and microwave waveguides (Lodahl, Mahmoodian,

and Stobbe, 2015; Nieddu, Gokhroo, and Chormaic, 2016; Roy, Wilson, and Firstenberg, 2017; Chang *et al.*, 2018). The resulting emerging field of research is termed waveguide quantum electrodynamics (WQED). It offers novel opportunities both for fundamental physics and for quantum information processing.

Since photons are confined within the waveguide, atom-photon interactions become much stronger than in free space, which is similar to the case of cavity QED. The WQED is also closely linked to circuit QED, which studies networks of coupled superconducting qubits interacting with microwave photons (Gu *et al.*, 2017; Carusotto *et al.*, 2020; Blais *et al.*, 2021). The distinguishing feature of WQED is the coupling of quantum emitters to only a single or several propagating photon modes. This inherently one-dimensional geometry is beneficial for the cascaded processing of photons, enabling an efficient generation and detection of quantum states of light (Prasad *et al.*, 2020). From the fundamental side, WQED systems can be viewed as artificial media with strong optical nonlinearities at a single-photon level (Chang, Vuletić, and Lukin, 2014). The combination of a strong atom-photon interaction with the light-mediated coupling between atoms at large distances also makes WQED setups unusual from the point of view of condensed matter physics. They can act as quantum simulators of many-body effects ranging from superfluid–Mott insulator transitions (Shi *et al.*, 2018) to topological states of matter (Kim *et al.*, 2021) and many-body localization (Fayard *et al.*, 2021).

There are already a number of topical reviews related to the waveguide quantum electrodynamics (Roy, Wilson, and Firstenberg, 2017; Chang *et al.*, 2018; Türschmann *et al.*, 2019), quantum optics with atoms and fibers (Nieddu, Gokhroo, and Chormaic, 2016), quantum light-matter interfaces (Hammerer, Sørensen, and Polzik, 2010; Lodahl, Mahmoodian, and Stobbe, 2015), quantum simulations, and many-body physics with light (Noh and Angelakis, 2017). State-of-the-art structures for single-photon processing were reviewed by Uppu *et al.* (2021). The goal of this review is twofold. First, we discuss in detail several recent representative experiments in the WQED setups and beyond, including demonstrations of tunable photon bunching and antibunching from atomic arrays (Prasad *et al.*, 2020), generation and detection of collective entangled atom-photon states (Corzo *et al.*, 2019), and subradiant atom-made mirrors (Rui *et al.*, 2020). We also compare different state-of-the-art experimental WQED platforms. Second, we provide a comprehensive theoretical background on the cooperative emission effects and photon-photon interactions for one-dimensional ordered atomic arrays, starting with the basics and proceeding to advanced theoretical techniques. Owing to certain similarities between the Dicke model of quantum optics and the Kondo model (Leggett *et al.*, 1987), many techniques have been adopted from condensed matter physics (the Bethe *Ansatz*) and quantum field theory (the functional integral approach). While the Dicke model for photons scattering on two-level atoms located at exactly the same point can be solved with the Bethe *Ansatz* (Rupasov and Yudson, 1984; Yudson, 1985), the generalized case of nonzero interatomic spacing is still far from completely understood despite significant recent
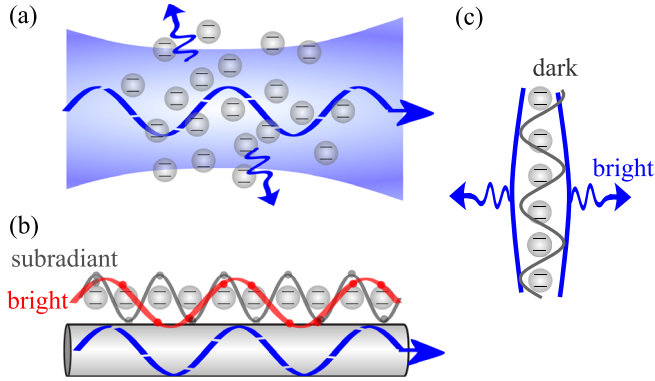
(a)

(c)

dark

bright

(b)

subradiant

bright

FIG. 1. Schematic of light-matter interactions in various atomic ensembles. (a) Light beam propagation and scattering in a disordered dilute atomic array in free space. (b) Interaction of an ordered atomic array with the guided photon mode. Subradiant and bright collective array excitations that are out of phase and in phase with the photon mode (blue, long-dashed wavy arrow) are shown. (c) Interaction of an ordered atomic array with a photon mode propagating through a waveguide in the transverse direction. As in (b), bright and dark collective excitations are shown.

theoretical progress. It manifests a plethora of phenomena familiar from other fields, such as the formation of bound photon states, the fermionization of photons, interaction-induced topological states, and analogs of quantum Hall phases.

We start in Sec. II.B with a comparison of various experimental platforms for the waveguide quantum electrodynamics that differ according to the choice of natural or artificial atoms and waveguide realizations. We take a universal perspective based on the typical numbers of emitters and the light-matter coupling strength and also provide an outlook by discussing emerging platforms in Sec. II.C. Section III presents a detailed theoretical consideration of hybridized atom-photon states (polaritonic states) in the waveguide with periodic arrays of emitters. We discuss collective superradiant and subradiant states and the resulting correlations between photons scattered on such structures. Several experimental demonstrations for different platforms are reviewed in Sec. IV, where we emphasize the demonstrations of superradiance (Sec. IV.A) and subradiance (Sec. IV.D), the generation of quantum states of light (Sec. IV.B), quantum memory applications (Sec. IV.C), and the physics of Bragg-spaced atomic arrays (Sec. IV.E). Finally, Sec. V presents the summary and outlook. To make the main text more accessible, we reserve most of the theoretical details for Appendixes A–J.

II. WAVEGUIDE-QED SYSTEMS

A. Tuning light-matter coupling in atomic arrays

In this section, we consider various WQED platforms that have different advantages depending on the waveguide realization and the type of quantum emitter. For example, both cold atom arrays and solid-state emitters can be used to generate and detect quantum light. The former are especially beneficial for quantum memory due to their high coherence.

Superconducting qubit structures operating in the microwave spectral range have tremendous tunability that can be exploited to process quantum states. Before proceeding to the specifics, it is instructive to first discuss the general advantages of waveguide coupling for a specific case of a cold atom ensemble as compared to atoms in free space.

The main idea behind WQED is to controllably enhance or suppress the light-matter interaction of an N-atom ensemble with a given propagating photon mode. As such, the two most important parameters are the number of atoms N and the coupling efficiency β. We define the latter as the ratio of the radiative decay rate of an individual emitter into the waveguide mode Γ_{1D} to its total decay rate $\Gamma_{tot} = \Gamma_{1D} + \Gamma_{nonrad} + \Gamma_{ng}$ (Arcari *et al.*, 2014; Scarpelli *et al.*, 2019),

$$\beta = \frac{\Gamma_{1D}}{\Gamma_{1D} + \Gamma_{ng} + \Gamma_{nonrad}}. \tag{1}$$

In Eq. (1) Γ_{ng} is the radiative decay rate into all other electromagnetic modes (nonguided modes) and Γ_{nonrad} is the homogeneous nonradiative decay rate. It is instructive to discuss how the values of Γ_{1D} and Γ_{ng} can be tailored to increase β.

We start with the beam propagation in a dilute disordered atomic array in free space; see Fig. 1(a). In this case, the efficiency of the light interaction with an atom can be estimated as $\beta = \sigma_0/A$, where σ_0 is the light scattering cross section and A is the effective beam area. For an ideal two-level atom at the electric dipole resonance, one has $\sigma_0 = 3\lambda_0^2/2\pi$. The area of A is limited from below by the diffraction limit or the sample area, and it is typically much larger than λ_0^2 (Hammerer, Sørensen, and Polzik, 2010). For instance, in a Cs atom sample with a diameter of 60 μm, which was considered by Windpassinger *et al.* (2008), the effective β factor was low, on the order of 10^{-4}. The crude estimation of the β factor as $\beta = \sigma_0/A$ indicates that it can be enhanced by reducing the effective area of the photon mode A, which can be done by confining photons to the waveguide; see Fig. 1(b). In realistic atomic arrays near a fiber waveguide with a radius of 400 nm, this factor is on the order of $\beta \sim 10^{-2}$, which is larger by 2 orders of magnitude than in free space.

One more important parameter that should be minimized to increase the β factor is the decay rate of the nonguided modes in the transverse direction Γ_{ng}; see Fig. 1(b). In typical disordered fiber-coupled arrays, this rate is on the order of the spontaneous decay rate of a single atom in free space, the decay rate of the atom in vacuum Γ_0 (Le Kien *et al.*, 2005), but it can be optimized in ordered arrays. Namely, only the collective modes that are inside the light cone, i.e., have a wave vector k along an array smaller than ω_0/c, can emit into free space. The modes with $|k| > \omega_0/c$ are evanescent in the direction transverse to the array. Provided that the array spacing is smaller than the light wavelength, most of the modes will be guided ones.

Another crucial figure of merit for the light interaction strength in the entire array is the resonant optical depth (OD) given by $OD = -\ln T(\omega_0) \approx 2N\Gamma_{1D}/\Gamma_0$, where $T(\omega_0)$ is the transmission coefficient at the resonance frequency ω_0.

TABLE I. Light-matter coupling phenomena in various quantum optical systems.

System	Enhanced interaction	Long-range coupling	Collective eigenmodes		Details
			Superradiant	Subradiant	
Two atoms in free space	×	×	✓	✓	Section IV.A
Two atoms near a waveguide	✓	✓	✓	✓	Section IV.A
Dense array near a waveguide	✓	×	×	×	Sections III.A.2, IV.B, and IV.D
Bragg-spaced array near the waveguide	✓	✓	✓	✓	Section IV.E
Array in a cavity	✓	×	✓	✓	
Ordered 2D array in free-space	✓	✓	✓	✓	Section III.C

Note that the expression $OD = 2N\Gamma_{1D}/\Gamma_0$ is valid only for non-Bragg arrays; see Asenjo-Garcia, Hood *et al.* (2017). In free space, if the atoms are far apart, the OD emerges from forward propagation and can be expressed as $OD = 2n\sigma_0 L$, where $n = N/A$ is the density of atoms in an ensemble of length L. Increasing the OD is important for many quantum information applications, such as quantum memory (Gorshkov *et al.*, 2007). However, achieving a high OD is challenging, and an OD ~ 10 for an atomic ensemble in free space requires $\sim 10^5 - 10^6$ atoms (Windpassinger *et al.*, 2008). In Eq. (1), one can see that the optical depth can also be expressed as $OD = 2N\beta$. As previously mentioned, in realistic atomic arrays near a fiber waveguide the β factor is on the order of $\beta \sim 10^{-2}$, which means that an OD ~ 10 can already be reached for $N \sim 1000$ of atoms, which is smaller by 2 to 3 orders of magnitude than in free space (Corzo *et al.*, 2019).

At the same time the coupling between the emitters mediated by the waveguide photons is enhanced and becomes long-range. If the position of emitters along the waveguide can be controlled, as in the case of solid-state quantum emitters and superconducting qubits, the formation of collective atomic excitations becomes important, and their interaction with light can be further optimized. The basic idea is that only the array excitations that are in phase with the guided wave couple to light efficiently. For the rest modes, the interaction is suppressed and they become subradiant, as illustrated in Fig. 1(b). This allows one to increase the lifetime of a stored quantum state that is beneficial for quantum information and, in particular, quantum memory applications. In additional, subradiant states have an enhanced sensitivity to external fields and suppressed decoherence, making themselves important in metrology. Note that $OD = 2N\beta$ in fact treats the atomic array as a homogeneous medium: the entire role of inhomogeneity is reduced to the scattering losses. The formation of collective atomic excitations, which can have decay rates different from the free-space atomic decay rate Γ_0, is also not captured by the concept of OD. However, in disordered dilute arrays this effect is relatively unimportant (Andreoli *et al.*, 2021).

Since the concepts of waveguide-enhanced coupling, long-range photon-mediated interactions, and collective superradiant and subradiant excitations are extensively used in the rest of the review, in Table I we summarize how these phenomena are manifested in various systems. Specifically, collective excitations can already form for two atoms in free space (DeVoe and Brewer, 1996; Guerin, Araújo, and Kaiser, 2016), but photon-mediated coupling between two atoms decays with distance. On the other hand, if such a pair of atoms is placed near a waveguide, the coupling between them is enhanced and becomes long-range. The situation with a dense atomic array near the waveguide is more subtle. If the waveguide-enhanced β factor remains much smaller than unity, the interaction of light with the atoms can still be considered independently, as in 1D free space, and is characterized by the concept of the OD. For a large OD the transmission of photons between atoms on the opposite sides of the array is suppressed, so the role of long-range interaction and collective modes is less important. In another words, most of the phenomena can still be described by treating the array as an effective homogeneous resonant optical medium. Thus, while long-range coupling is inherent to this problem, it is not directly manifested in a dense array. A more detailed discussion is given in Sec. III.A.2. For a large β factor collective subradiant modes can form and can be experimentally observed if the β factor is high; see Sec. IV.D for details. The situation drastically changes in a Bragg-spaced array, where a collective superradiant mode is formed due to the waveguide-mediated interaction between all the atoms. This is somewhat similar to the cavity-QED setup, where collective states can also form, but the interaction is not long-range. An ordered 2D array in free space presents one more flexible setup [illustrated in Fig. 1(c)]. Depending on the lattice period one can tune the strength of atom-photon interactions for various collective modes of this array. This is discussed in more detail in Sec. III.C.

Having stated these basic principles of light-matter coupling engineering, we now present a more specific overview of the different WQED platforms shown in Fig. 2. Typical values of the parameters N, β, and others are listed in Table II. We now discuss them in more detail.

B. Established platforms

We start with artificial atoms, semiconductor quantum dots (QDs) (Versteegh *et al.*, 2014; Thyrrestrup *et al.*, 2018; Foster *et al.*, 2019; Le Jeannic *et al.*, 2021), which operate in the near-infrared or visible spectral range; see Fig. 2. The main advantage of the QD platform is the fact that the dots are incorporated into the bulk of the photonic structure, which results in a relatively high coupling factor β of up to 99% (Scarpelli *et al.*, 2019). Precise control over the position of the quantum dot within the photonic structure allows for a flexible
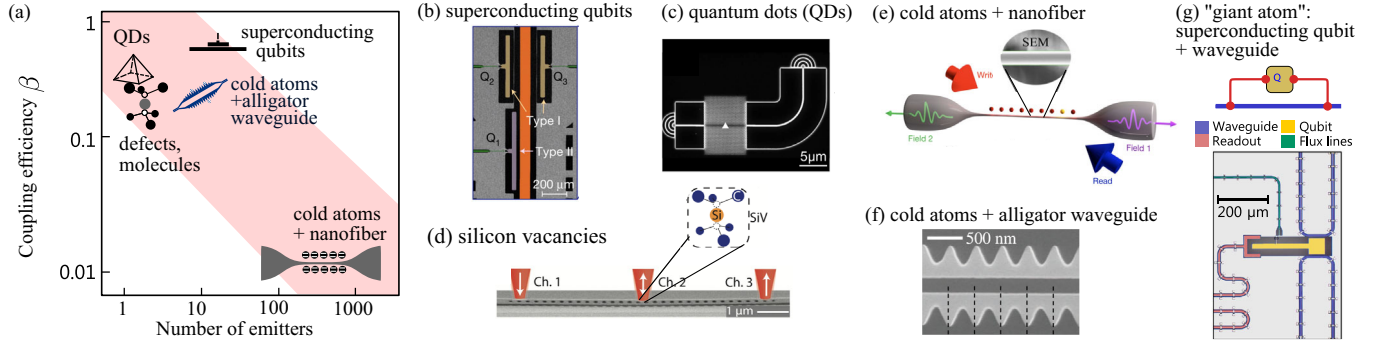
FIG. 2. (a) Comparison of a waveguide coupling efficiency β and number of emitters N for different platforms of waveguide quantum electrodynamics. (b)–(e) Schematics of different platforms. More information is given in Table II. (b) From Mirhosseini *et al.*, 2019. (c) From Foster *et al.*, 2019. (d) From Sipahigil *et al.*, 2016. (e) From Corzo *et al.*, 2019. (f) From Goban *et al.*, 2015. (g) From Kannan *et al.*, 2020.

tuning of the local field properties at the dot position that facilitates effective Purcell factor engineering (Lodahl *et al.*, 2004; Liu *et al.*, 2018). Foster *et al.* (2019) reported an increase of the radiative decay rate for a quantum dot coupled to a photonic crystal waveguide by a Purcell factor of 5. Another interesting direction in quantum optics is the chiral light-matter interaction. This can be realized by tuning the polarization properties of the local electromagnetic field near the quantum dot (Söllner *et al.*, 2015; Coles *et al.*, 2016; Lodahl *et al.*, 2017) and applying a static magnetic field or inducing spin polarization (Javadi *et al.*, 2018). This is discussed in more detail in Sec. III.B. Quantum dots have numerous decoherence mechanisms that are typical for a solid-state system, including charge and spin fluctuations and phonon-mediated decoherence. These factors lead to fluctuations of the resonant frequency and, even when not affecting the strength of the coupling to a given photon mode directly, they limit the coherence of the system and the indistinguishability of the emitted photons. In a crude approximation the decoherence can be incorporated into the extra nonradiative decay term Γ_{nonrad} in the denominator of the β factor in Eq. (1) (Arcari *et al.*, 2014). Thus, the β factor in Eq. (1) depends not only on the electromagnetic properties of the environment but also on the QD material properties and temperature. The record value $\beta \sim 99\%$ is reached at cryogenic temperatures when Γ_{nonrad} is quenched (Scarpelli *et al.*, 2019). While the nonradiative decay and decoherence can be suppressed relatively effectively using a combination of specific techniques (Kuhlmann *et al.*, 2015; Dreessen *et al.*, 2018), the main challenge for the scaling of the self-organized quantum dot platform is the inhomogeneous broadening. WQED structures with a large number of QDs do not seem feasible because the strong inhomogeneous broadening typically greatly exceeds the radiative linewidth.

An alternative solid-state platform is presented by solid-state defects such as silicon vacancies (Sipahigil *et al.*, 2016) and germanium vacancies (Bhaskar *et al.*, 2017); see Fig. 2(d). In this case, defects can be selectively placed in diamond waveguides using the focused ion beam implantation. This results in enhancement of the light-matter interaction and a Purcell factor $\Gamma_{1D}/\Gamma_0 \sim 2$ to 3, as reported by Sipahigil *et al.* (2016). Inhomogeneous broadening seems to be less of an issue than in the quantum dot system: the generation of entangled states of two excited qubits has already been demonstrated (Sipahigil *et al.*, 2016). However, the overall coupling efficiency β is lower than it is for quantum dots. We have estimated $\beta \sim 0.5$ for Sipahigil *et al.* (2016) using the experimentally reported cooperativity value $C \sim 1$, which is related to the β factor as $C = \beta/(1 - \beta)$ (Arcari *et al.*, 2014). The reasons for a lower β factor may involve the complex energy structure of an individual vacancy with many optical transitions of close energies, as well as the interaction with the phonon environment and nonradiative decay processes (Becker and Becher, 2017).

Another interesting system is offered by organic molecules such as dibenzoterrylene (DBT) (Faez *et al.*, 2014) or terrylene (Skoff *et al.*, 2018) coupled to a waveguide. Like quantum dots, molecular arrays exhibit strong inhomogeneous

TABLE II. Parameters of different state-of-the-art WQED platforms. The indicated numerical values are approximate and were taken from Corzo *et al.* (2016), Solano *et al.* (2017), Goban *et al.* (2015), Mirhosseini *et al.* (2019), Foster *et al.* (2019), Sipahigil *et al.* (2016), and Faez *et al.* (2014), respectively.

Material system	Number of resonant emitters N	Transition energy $\hbar\omega_0$	Free-space radiative linewidth $\Gamma_0/2\pi$	Coupling efficiency β
Cs atoms + nanofiber	$1\ldots10^3$	1.5 eV	5.2 MHz	10^{-2}
Rb atoms + nanofiber	$1\ldots6$	1.6 eV	6.1 MHz	10^{-1}
Cs atoms + alligator waveguide	$1\ldots3$	1.4 eV	4.6 MHz	0.5
Superconducting transmon qubits	10	0.03 meV (7 GHz)	$10\ldots100$ MHz	0.999
Quantum dots	1	1.4 eV	0.2 GHz	0.99
Si vacancies in diamonds	2	1.7 eV	100 MHz	~0.5
Organic molecules	1	1.6 eV	30 MHz	0.2

broadening, which limits the scalability of the system. About 5000 spectral lines, corresponding to different molecules, were revealed in the experiment described by Faez *et al.* (2014), who put the DBT molecules in naphthalene, filling a nanocapillary waveguide. Individual lines that demonstrate relatively high coupling efficiency and strong antibunching could be resolved spectrally. Apparently, the homogeneous nonradiative decay Γ_{nonrad} is not an issue for molecules. The β factor given by Faez *et al.* (2014) was determined solely by electromagnetic properties, the competition of the emission into the waveguide, and the emission into free space. The maximum value $\beta = 0.18$ has been reached for emitters positioned in the center of the fiber and the optimal fiber core radius was equal to 300 nm.

We now turn to superconducting transmon qubits operating at microwave frequencies, which are shown in Fig. 2(b). In a simplified description, such qubits each present a high-quality transmission-line resonator with a Josephson junction providing strong nonlinearity on a single-photon level (Koch *et al.*, 2007; Jung, Ustinov, and Anlage, 2014). The typical resonance frequency of the qubits is on the order of $5 - 10$ GHz. Thus, to suppress thermal noise they operate at low temperatures on the order of 10 mK. The first experimental demonstrations of a single-photon scattering, Mollow triplet formation, and generation of quantum states of microwave photons were made over a decade ago (Astafiev, Zagoskin *et al.*, 2010; Hoi *et al.*, 2011, 2012). Superconducting qubits have become the leading architecture for quantum information processing in circuit QED (Blais *et al.*, 2021). Their main advantage is the possibility of individual control of every qubit. This also makes them suitable for quantum information processing and quantum simulations in the waveguide QED, where the waveguide coupling efficiencies β can exceed 99.9% (Mirhosseini *et al.*, 2019). Most recent experimental WQED studies with superconducting qubit arrays have focused on the single-excited states (Mirhosseini *et al.*, 2019; Brehm *et al.*, 2021; Kim *et al.*, 2021). The reason for this is that it is hard to selectively access higher-excited quantum states using just a single waveguide mode. Moreover, large amount of higher-excited states are strongly subradiant (Zhang and Mølmer, 2019; Poshakinskiy *et al.*, 2021) and weakly coupled to the waveguide photons. To excite them selectively, one could drive the qubits from the side of the waveguide. This requires more complicated samples but is technologically possible. Double-excited subradiant states in the four-qubit array have recently been observed in such a way (Zanner *et al.*, 2022).

However, potential challenges limiting the performance of state-of-the-art circuits include individual defects such as charged two-level systems residing in the tunnel barrier of the Josephson junction or weakly coupling defects on the surfaces and interfaces of circuit electrodes (Barends *et al.*, 2013; Burnett *et al.*, 2019; Bilmes *et al.*, 2020). As a result, the maximum coherence time of qubits is still on the order of hundreds of microseconds (Rigetti *et al.*, 2012; Bilmes *et al.*, 2020).

Another waveguide quantum electrodynamics platform is presented by arrays of laser-cooled atoms of cesium (Vetsch *et al.*, 2010; Goban *et al.*, 2012; Corzo *et al.*, 2016; Sørensen *et al.*, 2016) or rubidium (Solano *et al.*, 2017) that are trapped

near an optical nanofiber (Nieddu, Gokhroo, and Chormaic, 2016); see Fig. 2(e). The main idea is that the evanescent field surrounding the fiber creates a trapping potential for atoms near the fiber wall. The resulting values of the β factor and the number of trapped atoms are sensitive to the specific trap design. One of the designs includes two pairs of counter-propagating beams in the fiber, one that is attractive red detuned and another that is repulsive blue detuned, operating at the specific wavelengths (Le Kien, Balykin, and Hakuta, 2004). The entire system overlaps with a magneto-optical trap. When compared with the superconducting qubit platforms or the solid-state structures, the waveguide coupling efficiency is relatively low ($\beta \sim 1\%$). It is controlled by the competition of the emission into free space Γ_{ng} and into the waveguide Γ_{1D}, $\beta = \Gamma_{1D}/(\Gamma_{1D} + \Gamma_{ng})$, while the homogeneous broadening Γ_{nonrad} is negligible. Access to individual atoms near the fiber is challenging, which rules out many applications for quantum information processing. On the positive side, the traps can host thousands of atoms. The waveguide-mediated interactions between atoms are much stronger than in free space and involve all atoms in the array while coherence remains high. The inhomogeneous broadening is weak, on the order of the free-space atom linewidth Γ_0 (Corzo *et al.*, 2016). This makes the fiber-coupled arrays beneficial for quantum memory applications (Corzo *et al.*, 2019) and for the generation and detection of quantum light (Prasad *et al.*, 2020). Another possibility, created when the external magnetic field is applied, induces chiral one-way interactions between the atoms. In this case, one can develop nonreciprocal devices and deterministic light-matter interfaces that can be useful in quantum communications (Lodahl *et al.*, 2017).

The optical trapping scheme can be tailored to decrease the distance from atoms to the nanofiber, which leads to larger coupling efficiency $\beta = 0.13$ (Solano *et al.*, 2017). However, the number of atoms studied in this experiment has been considerably smaller, up to just $N = 6$. The atom positions have been random, so different collective superradiant or subradiant states were observed for subsequent experimental realizations. A more detailed calculation of the β factor for realistic multilevel atoms, coupled to the fiber waveguide, is presented in Sec. III.A.5. It shows that the maximum value reached for atoms at the waveguide surface is $\beta \sim 0.3$.

The β factor can be increased even further up to $\beta \sim 50\%$ by replacing a nanofiber with the alligator photonic crystal waveguide illustrated in Fig. 2(f). The distinct near-field maxima between the "alligator scales," which are close to the waveguide surface, enable an efficient trapping of atoms with a high coupling efficiency. However, the delivery of atoms to submicron-size optical traps of an alligator waveguide is even more challenging and requires a careful engineering of the trapping beams (Béguin *et al.*, 2020). The number of trapped atoms realized in practice is small; for example, Goban *et al.* (2014, 2015) reported an atomic number of $N \sim 3$ on average. In the parameter space of Fig. 2(a), the alligator waveguide platform seems to be closer to solid-state quantum emitters. The possibility of creating photonic band gaps in the alligator waveguide also provides more possibilities to tailor light-matter interactions and atom-photon bound states; see Sec. II.C for a more detailed discussion.

One more interesting waveguide-QED platform is based on giant atoms, i.e., atoms that are coupled to a waveguide at multiple points that can be spaced by a wavelength distance or more; see Fig. 2(g). The main advantage of such a system is that multiple coupling points of giant atoms give rise to interference effects that are not present in quantum optics with pointlike atoms. These interference effects can lead to a coherent exchange interaction between atoms mediated by a waveguide, and it can result in suppression of relaxation of one or more atoms into the waveguide (Frisk Kockum, Delsing, and Johansson, 2014; Kockum, Johansson, and Nori, 2018; Guo *et al.*, 2020). Such systems can be implemented with superconducting qubits coupled to either microwave transmission lines (Kannan *et al.*, 2020) or surface acoustic waves (Gustafsson *et al.*, 2014) [see Fig. 2(g)] and cold atoms (Frisk Kockum, 2021). Specifically, the spontaneous decay rate for a superconducting qubit shown in Fig. 2(g), which is linked to the waveguide in the two points, is proportional to $1 + \cos 2\varphi$, where φ is a phase gained by photons traveling between these points. Thus, by tuning the phase φ (for example, by changing the qubit resonance frequency) it is possible to control the decay rate. One can also realize configurations with braided coupling between giant atoms and the waveguide so that the atoms will be coherently coupled to each other and, at the same time, protected from spontaneous decay into the waveguide (Kannan *et al.*, 2020).

A generalization of the giant atom concept was put forward by Karg *et al.* (2019), who showed that coherent light-mediated coupling between two distant quantum systems can be realized when light interacts twice with each quantum system and the second interaction is the time reversal of the first. A proof-of-concept experiment was reported by Karg *et al.* (2020), where a mechanical oscillator was entangled with atomic spins located at a 1 m distance due to the interaction mediated by a laser beam in a loop geometry. More details on specific experiments for different platforms can be found in Sec. IV.

C. Emerging waveguide-QED platforms

Despite tremendous achievements in waveguide-QED technology, there is still a room for improvement. We illustrate some of the emerging structures in Fig. 3.

As demonstrated by Fig. 2(a), there seems to be a trade-off between the individual emitter coupling efficiency and the number of emitters, so their product for state-of-the-art structures is roughly the same (see the shaded region). There is still a lack of structures with large number of resonant emitters $N \gtrsim 20$ that have at the same time a high coupling efficiency of the order of unity, so substantial progress can be expected. One of the avenues to go in the large-N, large-β direction could be offered by so-called Rydberg superatoms (Paris-Mandoki *et al.*, 2017; Stiesdal *et al.*, 2018, 2021); see Fig. 3(a). Each superatom is formed by a cloud of thousands of individual atoms such as ^{87}Rb. Owing to the Rydberg blockade, every cloud can absorb only one photon in a collective superradiant Dicke mode. Thus, the entire cloud acts as an effective two-level system that demonstrates characteristic two-photon (Paris-Mandoki *et al.*, 2017) and
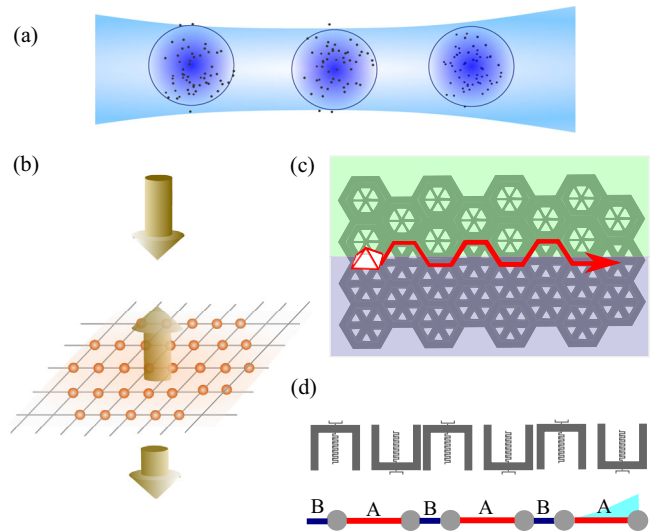

FIG. 3. Schematics of potential future platforms for WQED. (a) Three clouds of Rydberg atoms in free space. From Stiesdal *et al.*, 2021. (b) Planar two-dimensional atomic array. From Rui *et al.*, 2020. (c) Top panel: array of superconducting LC resonators with alternating short and long spacings. From Kim *et al.*, 2021. Bottom panel: schematics of the topologically nontrivial Su-Schrieffer-Heeger model and the edge state realized in this array. (d). Topologically nontrivial photonic state excited by a quantum dot and propagating between two photonic crystals. From Barik *et al.*, 2018.

three-photon (Stiesdal *et al.*, 2018) quantum correlations. Cascaded coupling of light to three clouds of Rydberg atoms was demonstrated by Stiesdal *et al.* (2021). At first glance, these three coupled atomic clouds, which are illustrated in Fig. 3(a), have nothing in common with WQED since they are trapped in free space and there is no waveguide at all. However, every cloud scatters almost all light in the forward direction. Thus, it is preferentially coupled to only one photon mode, and the scattering directionality, being larger than 0.85, plays the role of an effective β factor. The structure given by Stiesdal *et al.* (2021) was proposed for controllable substraction of up to $n = 3$ photons from the input light pulse. The drawback of the setup is unwanted scattering from the bright collective eigenstates of the cloud to its dark eigenstates. This process is more efficient than the forward emission by about an order of magnitude.

Another idea of a "waveguide QED without a waveguide" could be offered by ordered two-dimensional atomic arrays (Rui *et al.*, 2020) in an optical lattice (Bloch, Dalibard, and Nascimbène, 2012); see Fig. 3(b). If the spacing between atoms is smaller than the light wavelength, the array scatters light in the far field only in the forward or backward direction and light diffraction is not possible. In this case, the entire array can be viewed as an effective atom coupled to photons propagating only in one dimension, perpendicular to the array plane: a sort of an atom-array "antenna" (Shahmoon *et al.*, 2017). The parameters of such an effective atom can be controlled by changing the lattice period. For example, subradiant behavior of the planar array of ^{87}Rb atoms with the period $\approx 0.7\lambda_0$ was recently demonstrated by Rui *et al.* (2020). The measured linewidth of an optical resonance
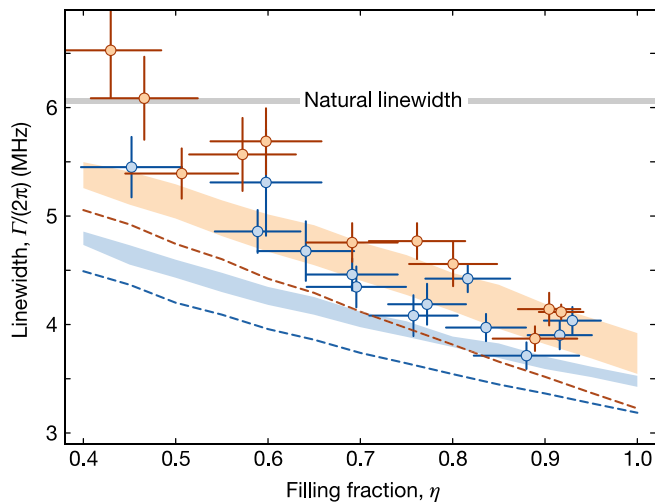
FIG. 4. Linewidth of the optical resonance of the atomic array with the period $a/\lambda_0 \approx 0.7$ depending on the array filling fraction. Decrease of the linewidth with the filling fraction indicates a collective subradiant response. From Rui *et al.*, 2020.

depending on the filling factor of the lattice is shown in Fig. 4. As the filling factor increases, the measured linewidth becomes smaller and approaches the theoretical prediction $\Gamma_{2D} \approx 0.5\Gamma_0$ corresponding to this spacing; see also the discussion in Sec. III.C.

Constructive interference between atoms in an array enhances the coupling with light, which is beneficial for quantum memory applications. According to Manzoni *et al.* (2018), the memory storage error is determined by the competition between the emission in the photonic mode propagating perpendicular to the array plane and the undesired diffraction, which is possible for finite-size arrays. It has been predicted that the error is quickly suppressed with the number of atoms N as $(\log N)^2/N^2$, and an array of only $N = 4 \times 4$ atoms could have a storage error below 1%, which is comparable to a disordered ensemble with an optical depth of around 600.

Studies of two-dimensional atomic arrays are now rapidly developing. It is technologically possible to assemble high-quality defect-free atomic lattices in arrays of tweezer microtraps (Barredo *et al.*, 2016; Ebadi *et al.*, 2021; Scholl *et al.*, 2021) containing up to a few hundred atoms. The limitation of this technique is that the lattice spacing cannot be subwavelength but is on the order of several microns. Complicated atomic arrangements have also been considered theoretically (Alaee, Gurlek *et al.*, 2020; Ballantine and Ruostekoski, 2020a). The unit cell with a quadrumer of atoms, each of which has the electric dipole optical transition, exhibits both electric and magnetic dipole responses (Ballantine and Ruostekoski, 2020b). Interference of electric and magnetic dipole emissions is constructive in the forward direction and destructive in the backward direction. As a result, the bilayer atomic array acts as a Huygens surface: it transmits light with a phase shift of π while the light reflection is suppressed. The directional forward or backward scattering by atomic arrays, called the Kerker effect, was also considered by Alaee, Safari *et al.* (2020). This research direction was inspired by the

recent significant progress in classical optics with conventional metamaterials (Kivshar, 2018). The atomic arrays feature high-quality resonances with vanishing inhomogeneous broadening and could be ideal for the realization of complicated optical states. It may be only a matter of time before optical bound states in continuum (Hsu *et al.*, 2016) or high-quality subradiant states (Koshelev *et al.*, 2020) are realized on the atomic platforms. Collective subradiant states of the array have already been proposed to store and manipulate quantum correlations (Facchinetti, Jenkins, and Ruostekoski, 2016; Ballantine and Ruostekoski, 2020c) and engineer entanglement (Guimond *et al.*, 2019). Quantum atom-made metasurfaces have been also proposed for the generation of highly entangled photon states (Bekenstein *et al.*, 2020; Bettles *et al.*, 2020), as discussed in more detail in Sec. III.C.

Thus far we have considered arrays of emitters coupled to conventional waveguides with linear light dispersion or to free-space photons. However, emitters can be embedded in more complicated photonic structures. For example, the development of future WQED platforms could be inspired by topological photonics (Khanikaev and Shvets, 2017; Ozawa *et al.*, 2019); we now review some of the considered systems.

First, it is possible to use the propagating topologically protected edge states of the two-dimensional photonic structure as the photonic modes, linking the quantum emitters (Barik *et al.*, 2020; Jalali Mehrabad *et al.*, 2020; Mehrabad *et al.*, 2020). Since the propagation of topological edge states is inherently unidirectional and robust against the backscattering on the imperfections, such structures could be beneficial for chiral quantum optics. One of the important recent milestones in this field was the demonstration of on-chip coupling of a single semiconductor quantum dot to the topological states propagating along the boundary between two photonic crystals (Barik *et al.*, 2018); see Fig. 3(c). The generation of entangled photon pairs via spontaneous four-wave mixing in topological photonic crystals made of coupled ring cavities and propagation of these pairs along the structure edge was demonstrated by Mittal, Goldschmidt, and Hafezi (2018). This could be potentially useful to protect quantum correlations.

Second, it has been proposed to create topological edge states from atom-photon interactions. For example, two-dimensional atomic arrays subjected to a perpendicular magnetic field were theoretically studied by Bettles *et al.* (2017) and Perczel *et al.* (2017). Like the conventional quantum Hall effect, the magnetic field leads to the formation of single-photon topological edge states that propagate along the edges of the array and that are protected against the disorder. More recently Perczel *et al.* (2020) proposed considering a lattice of nonlinear quantum emitters embedded in a photonic crystal slab. Again, this structure should feature band gaps induced by magnetic field, robust edge states, and also a nearly photonic flat band with a nonzero Chern number. This flat band should be sensitive to interactions, and this proposal could potentially be used to probe the many-body fractional quantum Hall states in quantum optical setups.

In addition to atoms coupled by propagating edge states of photons and propagating atom-photon edge states, one can also study atoms embedded in the bulk of topological photonic crystals (Song *et al.*, 2018; Mirhosseini *et al.*, 2019;

G.-Z. Song *et al.*, 2019; Kim *et al.*, 2021). If the energy of quantum emitters is in the band of propagating states, subradiant and superradiant states can form, as in a conventional waveguide. On the other hand, if the emitter energy falls into the photonic band gap of the array, it can act as a defect that leads to the formation of a localized photonic state bound to the emitter. This was experimentally observed for a superconducting qubit coupled to a microwave metamaterial waveguide by Mirhosseini *et al.* (2018).

The situation becomes even more interesting when the emitter is embedded in a topologically nontrivial structure such as the Su-Schrieffer-Heeger array of coupled cavities A-$B = A$-$B = A$-$B…$ (Bello *et al.*, 2019), which is shown in Fig. 3(d). The resulting bound states inherit the topological features of the underlying array. First, they are directional (i.e., they decay to either the left or the right from the emitter, depending on the sublattice that the emitter is coupled to); see Fig. 5(a). Second, the localized states have nonzero photon amplitudes at only one of the sublattices. The formation of photonic states bound to the emitters has recently been understood as a general feature of many topological photonic structures (Leonforte, Carollo, and Ciccarello, 2021). They have been termed vacancylike states due to the following unifying feature: the photon amplitude is zero at the site and is directly coupled to the emitter.

If the two emitters are coupled to different sublattices, the corresponding topological localized states can overlap and mediate their interaction, and the coupling will be directional as well. The proposal by Bello *et al.* (2019) was recently realized in the array of coupled superconducting qubits (Kim *et al.*, 2021). Figure 5(b) shows the experimentally measured directional coupling depending on the relative position of the two qubits in the array $i - j$. The coupling is zero when $i > j$, and the coupling decays exponentially for $i < j$. The range of the interaction depends on the width of the band gap of the lattice, which is controlled by the differences between the strong and weak couplings of the two qubits in the array. The smaller the band gap is, the longer the interaction range. Thus, one can also expect interesting physics for the 2D setup when the emitter is resonant with the photonic Dirac point.

Indeed, unusual quantum optical features have been predicted for an emitter embedded in a honeycomb lattice of coupled cavities in the tight-binding model (González-Tudela and Cirac, 2018). This structure features Dirac dispersion like that in graphene; see Fig. 5(c). Novel effects appear even for such simple problems as spontaneous emission when the emitter is resonant with the Dirac point. Owing to the vanishing density of photonic states at the Dirac point, within the Fermi golden rule approximation the emitter does not spontaneously decay at all. As a result, the non-Markovian effects start playing a decisive role in the spontaneous decay and the decay kinetics remains slow, and in the infinite system the emitter population decays with time t as $\propto 1/\ln^2 t$ (González-Tudela and Cirac, 2018). When two emitters are resonant with the Dirac point, their interaction becomes strongly sensitive to the sublattices they are coupled to; see Fig. 5(d). If emitters are coupled to the same sublattice, the interaction is dissipative and collective subradiant states can form. If they are coupled to different sublattices, as in the case
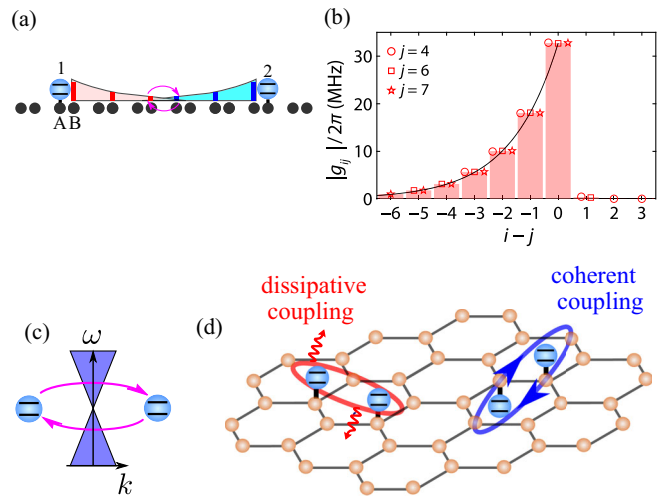

FIG. 5. (a) Schematics of two quantum emitters interacting via directional bound states in a Su-Schrieffer-Heeger lattice of coupled cavities. Vertical bars show the amplitudes of the photon wave function. (b) Measured directional coupling between two emitters in the topological Su-Schrieffer-Heeger superconducting qubit array. From Kim *et al.*, 2021. (c),(d) Schematics of two emitters coupled via the photonic graphene bath and tuned to the Dirac point. Depending on whether emitters are in the same sublattice or a different sublattice, the coupling is either dissipative or long-range coherent. From González-Tudela and Cirac, 2018.

shown in Fig. 5(a), the coupling becomes coherent and can be long-range. The results for the discrete tight-binding model given by González-Tudela and Cirac (2018) were recently also confirmed for a photonic crystal structure by Perczel and Lukin (2020). It has been predicted that such a system should feature long-range coherent light-mediated interactions between the emitters, which are essential for exploring exotic many-body phases (Richerme *et al.*, 2014).

Thus far most of the studies of the topological photonic structures have focused on a single-photon regime. However, Bello *et al.* (2019) considered many-body spin quantum phases emerging for an array of emitters coupled to the Su-Schrieffer-Heeger array. Recently it was predicted that hybridization of chiral photons in a topological two-dimensional cavity array with quantum emitters results in an entire zoo of interacting magnetic lattice models (De Bernardis *et al.*, 2021).

III. LIGHT-MATTER INTERACTIONS IN A WAVEGUIDE

In this section, we present a general overview of light-matter interactions in a waveguide setup. We start our consideration in Sec. III.A with regular periodic arrays of atoms that are symmetrically coupled to a waveguide. In Appendix A, we present the effective Hamiltonian of the problem. In Sec. III.A.2, we discuss single-photon scattering and collective single-excited states of the atomic array arising from waveguide-mediated interactions. Special attention is paid to long-living collective subradiant states in closely spaced atomic arrays and to Bragg-spaced atomic arrays, where the period is an integer multiple of half light wavelength at the atomic resonance. When measuring the reflected

and transmitted intensities for low input power, the results are similar to those in the regime of linear classical optics. The reason is that the quantum correlations are not directly probed by intensity measurements. More precisely, the quantum scattering theory in a single-photon regime yields results identical to those for a classical light scattered from a semiconductor quantum well (Ivchenko, Nesvizhskii, and Jorda, 1994a) or a resonator coupled to a waveguide (Fan, 2002). One more relevant but more exotic experimental realization is offered by arrays of Mössbauer nuclei such as ^{57}Fe, with sharp scattering resonances in the 10 keV spectral range (Röhlsberger *et al.*, 2010); see Lentrodt *et al.* (2020) for theoretical details on quantum optics with nuclei and Röhlsberger and Evers (2021) for a recent dedicated review. Thus, the results in Sec. III.A.2 for single-photon scattering spectra and eigenstates of waveguide-coupled atomic arrays could be applied to different setups with resonant scatterers coupled via a propagating photonic mode.

Light-matter interactions become especially interesting when more than one photon is present in the waveguide. Since a single atom cannot resonantly absorb two identical photons at the same time due to the strong anharmonicity of the atomic potential, there appears to be an effective photon-photon repulsion. This leads to nontrivial quantum correlations in the scattered light, photon bunching and antibunching. This is discussed in Sec. III.A.3. We present a comprehensive overview of different theoretical techniques while considering two-photon scattering. There has also been significant progress in theoretical studies of two-photon states in atomic arrays in recent years, including the structure of two-photon subradiant states (Albrecht *et al.*, 2019; Zhang and Mølmer, 2019) and the existence of bound two-photon states (Zhang, Yu, and Mølmer, 2020); we try to put these results in a universal perspective. We also examine the ultrastrong coupling regime in Sec. III.A.4. In addition to the simplified model of the idealized two-level atom, in Sec. III.A.5 we consider a more realistic situation in which an atom has a multilevel structure.

In most of this section, we discuss reciprocal symmetric waveguides, in which the atom is equally coupled to forward- and backward-propagating photons. However, it is possible to make coupling to forward- and backward-propagating photons asymmetric by breaking the electromagnetic reciprocity (by means of applying an external magnetic field, spin polarizing the atoms, or using the nonlinearity). This special chiral regime is reviewed in Sec. III.B, where we proceed from the basics of chiral coupling (Secs. III.B.1 and III.B.2) to the collective polariton eigenstates (Sec. III.B.3) to the advanced experiments on tunable photon bunching and antibunching in this setup (Sec. III.B.4).

Section III.C considers a new promising platform of regular two-dimensional atomic arrays in the free space (Rui *et al.*, 2020) that, as discussed in Sec. II, shares many similar concepts with the waveguide quantum electrodynamics.

A. Arrays with symmetric coupling

1. General formalism

We start this section with a general model for light interaction with an array of atoms that is embedded in an arbitrary structure with the dielectric permittivity $\varepsilon(\boldsymbol{r}, \omega)$, where ω is the light frequency and $\boldsymbol{r}$ is the radius vector. The linear electromagnetic properties of the dielectric environment can be characterized by the Green's function satisfying the equation

$$\boldsymbol{\nabla}_{\boldsymbol{r}} \times \boldsymbol{\nabla}_{\boldsymbol{r}} \times \mathbf{G}(\boldsymbol{r}, \boldsymbol{r}', \omega) = \left(\frac{\omega}{c}\right)^2 \varepsilon(\boldsymbol{r}, \omega)\mathbf{G}(\boldsymbol{r}, \boldsymbol{r}', \omega) + \delta(\boldsymbol{r} - \boldsymbol{r}').$$

$$(2)$$

In vacuum, when $\varepsilon = 1$ the Green's function is given by $G(\mathbf{r}, \mathbf{r}') = G^{(0)}(\mathbf{r} - \mathbf{r}')$, where

$$G_{\mu\nu}^{(0)}(\boldsymbol{r}, \omega) = \left[\delta_{\mu\nu} + \left(\frac{c}{\omega}\right)^2 \frac{\partial^2}{\partial x_\mu \partial x_\nu}\right] \frac{e^{i\omega r/c}}{4\pi r}, \qquad (3)$$

where $\mu, \nu = x, y, z$. For a waveguide, the Green's function can be separated into two parts,

$$\mathbf{G} = \mathbf{G}^{(\mathrm{guid})} + \mathbf{G}^{(\mathrm{leaky})}, \qquad (4)$$

corresponding to the interaction with guided and leaky modes. In particular, because of the translational symmetry, the wave vector along the waveguide axis k_z is a good quantum number. Depending on whether $|k_z|$ is smaller or larger than ω/c, either the mode can leak into free space or it is evanescent in the direction transverse to the waveguide corresponding to the two terms in Eq. (4). We now consider the interaction of light with an array of two-level atoms located at points $\boldsymbol{r}_m$ and having the same resonant frequency ω_0. The light-atom coupling is treated in the dipole approximation. It is described by a Hamiltonian $-\hat{\boldsymbol{d}} \cdot \boldsymbol{E}(\boldsymbol{r}_m)$, where $\boldsymbol{E}(\boldsymbol{r}_m)$ is the electric field at the atom and $\hat{\boldsymbol{d}}$ is the dipole momentum operator, $\hat{\boldsymbol{d}} = \boldsymbol{d}\sigma + \boldsymbol{d}^*\sigma^\dagger$, with $\boldsymbol{d}$ the matrix element of electric dipole momentum between the ground and excited states of the atom. Here and in the rest of the review we consider a pointlike atom, where this dipole approximation is reasonable. There are also "giant atoms" based on superconducting qubits that are connected to the waveguide in multiple distant points; see Frisk Kockum (2021) and Karg *et al.* (2019). We also assume the Markovian approximation, which means that the photon degrees of freedom are fast and can be traced out. The effective Hamiltonian of the atomic array assumes the form

$$H_{\mathrm{eff}} = \sum_{m=1}^{N} \omega_0 \sigma_m^\dagger \sigma_m + \sum_{m,n=1}^{N} \sigma_m^\dagger \sigma_n V_{mn}. \qquad (5)$$

We use the units with $\hbar = 1$ and the Gaussian units system. The operator $\sigma_m^\dagger$ describes excitation of the atom m and $\sigma_m \equiv |e_m\rangle\langle g_m|$, where $|g_m\rangle$ and $|e_m\rangle$ are the ground and excited states of atom m and

$$V_{mn} = -4\pi \frac{\omega_0^2}{c^2} \boldsymbol{d}_m^* \cdot \mathbf{G}(\boldsymbol{r}_m, \boldsymbol{r}_n, \omega_0)\boldsymbol{d}_n. \qquad (6)$$

The derivation of Eq. (6) and details of Green's tensor calculations for atoms near a realistic nanofiber waveguide can be found in the work of Kornovan, Sheremet, and Petrov (2016) and Pivovarov *et al.* (2018). The Hamiltonian (5)

describes the interactions between the atoms mediated by photons. It also assumes the rotating wave approximation, which holds provided that the array is excited resonantly and the atom-photon coupling is reasonably weak. An ultrastrong coupling regime in which the effective light-atom coupling constant is on the order of ω_0 and the counterrotating terms cannot be ignored is considered in Sec. III.A.4.

The Hamiltonian (5) assumes an especially simple form in the fully one-dimensional case when the leaky part of the Green's function is neglected and only one guided mode with the wave vector k_z along the waveguide is taken into account in the guided part. The guided term can be then presented as (Saravi *et al.*, 2017)

$$G_{\alpha\beta}^{(\text{guid})}(\boldsymbol{r},\boldsymbol{r}') = ig_0 \times \begin{cases} E_\alpha(\boldsymbol{\rho})E_\beta(\boldsymbol{\rho}')e^{ik_z(z-z')}, & z > z', \\ E_\alpha(\boldsymbol{\rho})E_\beta(\boldsymbol{\rho}')e^{-ik_z(z-z')}, & z < z'. \end{cases} \quad (7)$$

where $\boldsymbol{E}(\boldsymbol{\rho})$ is the electric field of the guided mode depending on the transverse coordinates $\boldsymbol{\rho} = (x, y)$ and g_0 is a constant factor. As a result, Eq. (5) reduces to

$$H_{\text{eff}} = \sum_{m=1}^{N} \omega_0 \sigma_m^\dagger \sigma_m - i\gamma_{1D} \sum_{m,n=1}^{N} \sigma_m^\dagger \sigma_n e^{ik_z|z_m-z_n|}, \quad (8)$$

where

$$\gamma_{1D} = 4\pi \left(\frac{\omega_0}{c}\right)^2 \text{Im}[\boldsymbol{d}^* \cdot \mathbf{G}^{(\text{guid})}(\boldsymbol{r},\boldsymbol{r},\omega_0)\boldsymbol{d}] \equiv g_0 |\boldsymbol{d} \cdot \boldsymbol{E}(\boldsymbol{\rho})|^2. \quad (9)$$

See Gruner and Welsch (1996) and Asenjo-Garcia, Hood *et al.* (2017) for more details. The non-Hermitian part of this Hamiltonian describes spontaneous decay due to the emission into the waveguide, and γ_{1D} is the spontaneous emission rate of an atom into the guided mode. Here and in the rest of the review we use lowercase γ letters for contributions to the imaginary part of complex eigenfrequencies, and capital letters for the corresponding decay rates ($\Gamma = 2\gamma$), i.e., $\gamma_{1D} \equiv \Gamma_{1D}/2$, etc.

In this section, we consider the case of a nonchiral light-atom interaction, where emission to the left and to the right has the same probability. The chiral scenario is analyzed in Sec. III.B. The Hamiltonian in Eq. (8) explicitly demonstrates distant long-range couplings between the atoms mediated by the waveguide mode. The non-Hermitian Hamiltonians (5) and (8) are useful for understanding collective quasistationary eigenstates of the atomic array with one or two excitations, which are considered in Secs. III.A.2 and III.A.3. These eigenstates can be probed as resonances for the incident photons. The problem of photon scattering on the atomic array can be considered using the general input-output formalism; see Lalumière *et al.* (2013), Caneva *et al.* (2015), and Das *et al.* (2018). In this case, instead of using the non-Hermitian Hamiltonian, one can directly solve the Heisenberg equations for the atomic operators σ_n or the master equation for the density matrix of the atomic array. In particular, Das *et al.* (2018) addressed the linear optical response in a general situation of multilevel atoms in an arbitrary dielectric environment. Note that in this review we focus on the case of

continuous input. We refer the interested reader to Kiilerich and Mølmer (2019, 2020) and references therein for an application of cascaded quantum theory (Gardiner, 1993) to the study of the interaction of quantum systems with the pulses of radiation.

In a case with many excitations, the eigenproblem and scattering problem are difficult due to the large size of the Hilbert space. In a few particular cases (for example, when all the atoms are located in one point), the scattering problem can be solved analytically, as discussed in Sec. III.A.3. A more general case can be considered using the matrix product state (MPS) approach, which is an established and powerful method for many-body effects in one-dimensional condensed matter systems (Schollwöck, 2011; Orús, 2014). The MPS technique is based on the following representation of the wave function of the many-body quantum state as a product of the auxiliary matrices A:

$$\psi(s_1, s_2, s_3, \ldots) = A_{\alpha_0\alpha_1}(s_1)A_{\alpha_1\alpha_2}(s_2)A_{\alpha_2\alpha_3}(s_3)\ldots, \quad (10)$$

where the indices α run in a finite range, $\alpha = 1, \ldots, M$, and the indices $s_1, s_2, \ldots$ describe quantum states of different particles $1, 2, \ldots$. In the case in which $M = 1$, the wave function factorizes, which means that the particles are independent. In the case in which $M > 1$, the quantum states of different particles become entangled with each other. It has been proven that the *Ansatz* (10) quickly convergences in the nondegenerate ground state of quantum systems with nearest-neighbor interactions such as spin chains (Orús, 2014). The Markovian MPS technique has been successfully applied to model atomic interactions in waveguides formed by coupled cavities (Manzoni, Mathey, and Chang, 2017). Photon scattering on an atomic array with the Langevin-MPS formalism was considered by Manasi and Roy (2018). To go beyond the Markovian regime and take into account retarded long-range interactions, it was proposed to discretize the problem in space and time (Grimsmo, 2015; Pichler and Zoller, 2016). The MPS technique can also be applied in the ultrastrong coupling regime (Peropadre *et al.*, 2013); see Sec. III.A.4 for more details. A detailed recent comparison of the MPS approach with another powerful technique, quantum trajectories method, was given by Arranz Regidor *et al.* (2021). This area is now rapidly developing, and we expect further powerful and practical calculation tools to soon become available.

2. Single-excited states

a. Polariton eigenstates

The effective Hamiltonian (5) commutes with the total number of excitation operators $\sum_{m=1}^{N} \sigma_m^\dagger \sigma_m$. Thus, subspaces with different excitation numbers can be analyzed separately. In this section, we consider single-excited eigenstates. They can be found by projecting the full Hamiltonian (5) onto the states $\sigma_n|0\rangle$, $H_{mn} = \langle m|H|n\rangle$. In Fig. 6, we present the real and imaginary parts of the eigenfrequencies ω found by diagonalizing the matrix H_{mn}; see Kornovan, Sheremet, and Petrov (2016). Figure 6(a) corresponds to an array with 40 atoms in free space, Fig. 6(b) refers to the same array interacting only via the waveguide mode, with collective coupling with the free space neglected, and Fig. 6(c)
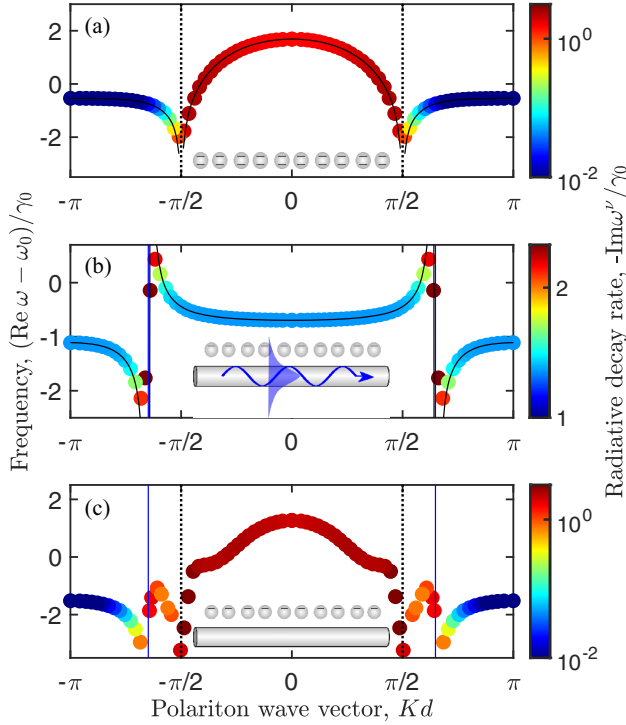
FIG. 6. Real and imaginary parts of the eigenmodes calculated for (a) an atomic array in free space, (b) an atomic array near the fiber waveguide, with collective emission into the free space neglected, and (c) the full model. The vertical dotted lines in (a) and (c) show the light cone boundaries ($K = \pm\omega/c$). The vertical solid blue lines in (b) and (c) show the guided mode wave vector $\pm\beta$. The black solid curves in (a) and (b) show the analytical results of Eqs. (11) and (12) for an infinite array. The eigenmodes have been calculated for $N = 40$ atoms perpendicularly polarized to the fiber. The polariton wave vector has been extracted from the Fourier transform of the eigenmodes. The other parameters are given in the text.

represents a full calculation for an array located close to the dielectric fiber waveguide. The parameters of the calculation follow Asenjo-Garcia, Moreno-Cardoner *et al.* (2017): the fiber permittivity is 4, $\omega_0 d/c = \pi/2$, $\omega_0 R/c = 1.2$, where d and R are the array period and the waveguide radius, the distance of the array from the fiber center is $\rho = 1.5R$, and $k_z \approx 1.56\omega_0/c$ is the guided mode wave vector. We now discuss these results in more detail.

The calculation in Fig. 6(a) was performed including only the free-space Green's function (3) in Eq. (6), thereby determining the effective Hamiltonian. The distribution of the real parts of the eigenfrequencies can be understood by comparing them to the eigenfrequencies for an infinite array, where the eigenstates are characterized with the wave vector $K(\omega)$ and can be sought in the form $\sum_n e^{iKn}\sigma_n^\dagger|0\rangle$. Their eigenfrequencies are well described by the following analytical expression (Asenjo-Garcia, Moreno-Cardoner *et al.*, 2017), which is shown as a black solid curve in Fig. 6(a):

$$\mathrm{Re}\,\omega(K) = \omega_0 + \frac{3\gamma_0}{4(\omega_0 d/c)^3}\mathrm{Re}\sum_{\sigma=\pm}[\mathrm{Li}_3(\xi_\sigma)$$
$$- i(\omega_0 d/c)\mathrm{Li}_2(\xi_\sigma) + (\omega_0 d/c)^2 \ln(1 - \xi_\sigma)], \quad (11)$$

where $\xi_\pm = \exp[i(\omega_0 d/c) \pm iKd/c]$ and Li are the polylogarithm functions.

The radiative decay rate of the eigenmodes, denoted in color in Fig. 6(a), strongly depends on the polariton wave vector along the array K. Namely, the emission in the direction transverse to the array is suppressed when $|K| > \omega_0/c$, which is outside the light cone. In the infinite array, the decay rate for $|K| > \omega_0/c$ would have been exactly zero. In the finite array, emission is still possible at the array edge in the longitudinal direction, but the eigenstates are strongly subradiant. The most subradiant eigenstates are close to the Brillouin zone edge ($|K| \approx \pm\pi/d$). The spontaneous emission rate quickly decreases with the array size as $-\mathrm{Im}\,\omega \propto \Gamma_0/N^3$ (Zhang and Mølmer, 2020). Moreover, Zhang and Mølmer (2020) proved that this decay law is universal. If the dispersion law close to the band edge behaves as $\omega(K) - \omega(\pi/d) \propto (K - \pi/d)^s$, the emission rate decreases as $1/N^{s+1}$. This result has a transparent interpretation: the larger the power s is, the "heavier" the polaritons and the harder it is for them to escape the array (Figotin and Vitebskiy, 2011; Poddubny, 2020).

We now take the interaction with the guided mode into account. To elucidate the role of the guided mode, we first use a simplified Hamiltonian

$$H_{\mathrm{eff}} + (\delta\omega - i\gamma)\sum_{n=1}^{N}\sigma_n^\dagger\sigma_n,$$

where H_{eff} is given by Eq. (8) and the $\delta\omega - i\gamma$ term describes the shift of the individual atom resonance and the modification of its decay rate due to the interaction with the nonguided mode. In other words, this model takes into account the Purcell factor for individual atoms and their collective coupling through the waveguide mode but ignores the collective emission into free space. The real part of the eigenfrequencies is well described by the dispersion law (Mahan and Obermair, 1969)

$$\omega - \omega_0 - \delta\omega + i\gamma = \gamma_{1\mathrm{D}}\frac{\sin\varphi}{\cos Kd - \cos\varphi}, \quad (12)$$

where $\varphi = k_z d$ is determined by the wave vector of the guided mode. Equation (12) is relatively easy to obtain by looking for the eigenstates of Eq. (8) in the form $\sum_n e^{iKn}\sigma_n^\dagger|0\rangle$. The infinite sum over n can be split into two parts, with $n < m$ or $n \geq m$, and each part is simply a geometric series. In the case in which the period of the atomic array is much smaller than the wavelength ($\omega d/c \ll 1$), Eq. (12) can be written as $K^2 = (\omega/c)^2\varepsilon(\omega)$, where (Ivchenko, 1991)

$$\varepsilon(\omega) = 1 + \frac{2\gamma_{1\mathrm{D}}}{\varphi(\omega_0 + \delta\omega - \omega - i\gamma)} \quad (13)$$

is the effective permittivity. The more dense the array is, the smaller φ and the stronger the resonance in the permittivity. We note that while the permittivity equation (13) captures the enhancement of the light-matter interaction due to the waveguide, it is a local characteristic. Therefore, the long-range waveguide-mediated interactions, while inherent to the
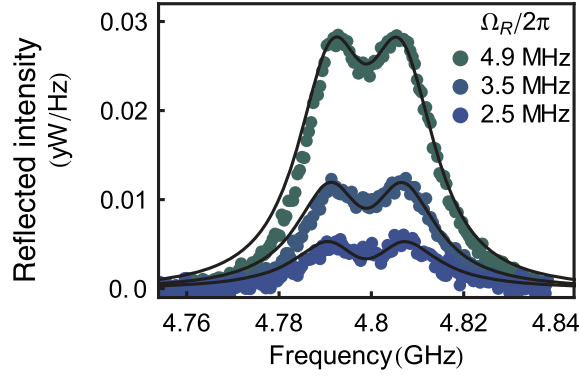
FIG. 7. Spectrum of light reflection from two superconducting qubits with the spacing $3\lambda(\omega_0)/4$ coupled to the waveguide depending on the driving. The driving strength is characterized by the Rabi frequencies Ω_R, shown in the graph; larger reflection corresponds to larger driving. From van Loo *et al.*, 2013.

Hamiltonian (8), are not directly manifested in the dense arrays; see also the previous discussion of Table I.

The dispersion curve manifests a characteristic avoided crossing of the free light dispersion $K = \omega/c$ with the atomic resonance. The polaritonic band gap is located in the frequency range

$$\omega_0 + \delta\omega - \gamma_{1D}\tan\frac{\varphi}{2} < \omega < \omega_0 + \delta\omega - \gamma_{1D}\cot\frac{\varphi}{2}. \quad (14)$$

The radiative decay rate dependence on K is significantly different than the free-space case. The largest decay rate corresponds to the states with $|K| \approx k_z$, which are in phase with the guided mode. We note that the eigenstates of the sole guided Hamiltonian (8) are also strongly subradiant for $K \approx \pm\pi/d$ and obey the same universal $-\text{Im}\omega \propto 1/N^3$ scaling with the array size. The only reason the decay rates are not small in Fig. 6(b) is the presence of the constant free-space emission term γ.

In fact, as pointed out by Asenjo-Garcia, Moreno-Cardoner *et al.* (2017), using the constant term to describe interaction with free-space photons is only a crude approximation. The results of the full calculation, including exactly both free-space and guided modes and following Kornovan, Sheremet, and Petrov (2016) and Asenjo-Garcia, Moreno-Cardoner *et al.* (2017), are presented in Fig. 6(c). The result inherits the features of both Figs. 6(a) and 6(b). Inside the light cone the dispersion of the eigenmodes is mostly due to free-space interactions and the spontaneous decay rate is large. There also is a resonant feature at the guided mode wave vector, shown as a thin vertical blue line in Fig. 6(c). It is absent for an array in free space and stems from the long-range waveguide-mediated couplings between the atoms. Close to the Brillouin zone edges ($K \approx \pm\pi/d$), the modes are strongly subradiant. As suggested by Asenjo-Garcia, Moreno-Cardoner *et al.* (2017) and Kornovan *et al.* (2019), these strongly subradiant modes could be relevant for quantum memory applications. While the decay modes obey the usual $1/N^3$ scaling for the parameters of Asenjo-Garcia, Moreno-Cardoner *et al.* (2017), the previously mentioned general results of Zhang and Mølmer (2020) suggest that by engineering the polariton

dispersion it should be possible to further suppress the decay rate. For example, it was numerically found by Kornovan *et al.* (2019) that the collective emission rate can be strongly suppressed for a certain lattice period $d/\lambda_0 \approx 0.24 \times 2\pi c/\omega_0$ and a specific fiber permittivity. The scaling $\sim 1/N^8$ has been extracted from the results of numerical calculation. By varying the lattice period d, one can achieve the degenerate band edge condition. Namely, the dispersion curve at the band edge appears to have quartic rather than quadratic dependence on the wave vector (Figotin and Vitebskiy, 2011; Zhang and Mølmer, 2020), resulting in a $1/N^5$ scaling. Moreover, by further tuning of the distance parameter $d(N)$ for each array size N, even stronger suppression of radiation can be observed due to the destructive interference of the two band edge modes (Kornovan *et al.*, 2021). However, once the atoms are distributed in a non-periodic manner, even exponential decays of the emission rate become possible by forming the Bragg-mirror atomic cavities (Asenjo-Garcia, Moreno-Cardoner *et al.*, 2017).

Note that even a small disorder in the atomic array leads to a significant modification of the collective decay rate. As shown by Kornovan *et al.* (2019), the disorder $\sim 10^{-3}\lambda_0$ modifies the collective decay rate scaling to $1/N^{3.7}$.

b. Eigenmodes mediated by the interaction via the waveguide

We now consider in more detail the case in which the interaction with free-space modes can be totally neglected and the coupling between the atoms in the array is fully determined by the interaction with the guided mode. We also assume for simplicity that the wave vector of the guided mode is given by $k_z = \omega/c$. The effective Hamiltonian (8) in the subspace of single-excited states $\sigma_n^\dagger|0\rangle$, where $|0\rangle \equiv |gg...g\rangle$ is the ground state of all the atoms, is then reduced to the following matrix (Ivchenko, 2005; Caneva *et al.*, 2015):

$$H_{mn} = \omega_0\delta_{mn} - i\gamma_{1D}e^{i\varphi|m-n|}, \quad (15)$$

where $\varphi = \omega_0 d/c$. This simplified model allows many instructive analytical solutions. It is also directly applicable to arrays of superconducting qubits, where the β factor is close to unity and interactions with free-space modes can be ignored.

We start our analysis of the waveguide-mediated coupling with the illustrative case of $N = 2$ qubits, where the matrix (15) assumes the form

$$H = \begin{pmatrix} \omega_0 - i(\gamma_{1D} + \gamma) & -i\gamma_{1D}e^{i\varphi} \\ -i\gamma_{1D}e^{i\varphi} & \omega_0 - i(\gamma_{1D} + \gamma) \end{pmatrix}. \quad (16)$$

The eigenfrequencies are given by

$$\omega_\pm = \omega_0 - i\gamma - i(\gamma_{1D} \pm \gamma_{1D}e^{i\varphi}), \quad (17)$$

and the eigenvectors correspond to symmetric and antisymmetric excitation ($[1, \pm 1]/\sqrt{2}$). The splitting between the eigenfrequencies of the qubit array (17) can be observed experimentally by measuring the reflection spectra. This was first done for two $[3\lambda(\omega_0)/4]$-spaced superconducting qubits,
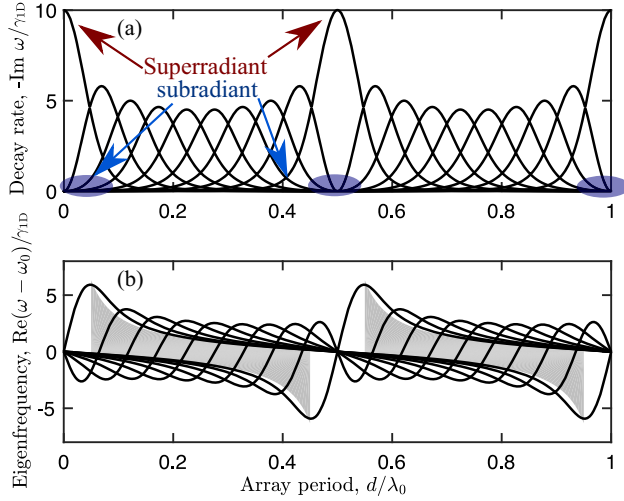
FIG. 8. (a) Imaginary and (b) real parts of the complex eigenfrequencies of the array of $N = 10$ atoms coupled to a waveguide depending on the period of the array d. The shaded areas in (b) show the edges of the polariton band gaps, calculated using a diagonalization of the Hamiltonian (15) for the vanishing nonradiative decay rate Γ. Each value of d/λ corresponds to $N = 10$ eigenvalues.

coupled to a waveguide, by van Loo *et al.* (2013); see the illustration in Fig. 7.

The dependence of the real and imaginary parts of the eigenfrequencies ω^ν for $N = 10$ qubits on the array period d is shown in Fig. 8. The real parts of the $N = 10$ eigenfrequencies in Fig. 8(b) periodically depend on d and concentrate near the two band gap edges given by Eq. (14) for $\delta\omega = \gamma = 0$ and $k_z d = \varphi$. The matrix H_{mn} is non-Hermitian but symmetric, which leads to the nonconjugated orthogonality condition $\sum_{n=1}^{N} P_n^\nu P_n^\mu = \delta_{\nu,\mu}$ for the eigenvectors P_n^ν. There is an exact analytical representation of the eigenvectors as a superposition of two-polariton Bloch waves (Voronov *et al.*, 2007),

$$P_n \propto \rho e^{iKn} + e^{-iKn} \propto e^{iK(n-N-1)} + \rho e^{-iK(n-N-1)}, \quad (18)$$

where $\rho = -(1 - e^{i(\varphi-K)})/(1 - e^{i(\varphi+K)})$ is the reflection coefficient of polaritons from the internal boundary of the array and K is the polariton eigenvector found in Eq. (12) with $\delta\omega = \gamma = 0$ and $k_z d = \varphi$. The two representations in Eq. (18) are equivalent because an analog of the Fabry-Perot condition $\rho^2 e^{2iK(N+1)} = 1$ holds at the eigenfrequencies ω^ν.

The eigenfrequencies ω_ν are complex, and the decay rate of the corresponding modes is equal to $-2\text{Im}\,\omega^\nu$. The center of mass of the eigenmodes does not depend on the spacing and is equal to $\omega_0 - i\gamma_{1D}$ (Vladimirova, Ivchenko, and Kavokin, 1998). In the limiting case where $d \to 0$, we obtain a single superradiant mode with $P_{\text{SR},n} = 1/\sqrt{N}$ and the eigenfrequency $\omega_{\text{SR}} = \omega_0 - iN\gamma_{1D}$. All other $N - 1$ modes are degenerate for $d = 0$ with the eigenfrequency ω_0. Their eigenvectors are found using the condition $\sum_{n=1}^{N} P_n = 0$, and all these modes are dark; i.e., they cannot be excited by the waveguide mode. When the spacing between atoms increases ($d \neq 0$), the dark modes stop being degenerate and acquire a finite radiative lifetime, as seen in Fig. 8(a). When $d \ll \lambda$ ($\varphi \ll 1$),

the radiative decay rate of the darkest subradiant modes is given by

$$-\text{Im}\,\omega^\nu = \gamma_{1D} \frac{\pi^2 \varphi^2 \nu^2}{8N^3}, \qquad \nu = 1, 2, \dots \ll N. \quad (19)$$

See Vladimirova, Ivchenko, and Kavokin (1998) and Zhang and Mølmer (2019). Hence, the radiative decay rate is suppressed by a factor of the order of $\varphi^2 \sim [d/\lambda(\omega_0)]^2$. Moreover, when the array size increases, the radiative decay rate further decreases as $1/N^3$ (Albrecht *et al.*, 2019; Zhang and Mølmer, 2020), as discussed previously in this section. For any given value of d/λ, most of the ten points in Fig. 8(a) are condensed near the abscissa axis and merge with each other, corresponding to strongly subradiant modes. The eigenvectors of subradiant modes can be found in Eq. (18) as

$$P_n \approx (-1)^n \sqrt{\frac{2}{N}} \sin\left[(\pi - k)\left(n - \frac{1}{2}\right)\right], \qquad n = 1, 2, \dots, N, \quad (20)$$

where $k = \pi - \pi/N, \pi - 2\pi/N, \dots$. They are standing waves with the wave vectors close to the edge of the Brillouin zone. The lifetimes of the eigenmodes depend periodically on the array period, as shown in Fig. 8. The situation with one superradiant mode and $N - 1$ dark modes is also realized for the Bragg-spaced arrays with $2d/\lambda_0 = 1, 2, \dots$. In this case, the polariton band gap is enhanced but should be calculated beyond the Markovian approximation. The physics of Bragg-spaced arrays is discussed in more detail later in this section.

It is instructive to note that the inverse to the shifted matrix (15) is a tridiagonal one (Poddubny, 2020),

$$\tilde{H} \equiv (H - \omega_0)^{-1}$$

$$= \frac{1}{\gamma_{1D}} \begin{pmatrix} -\frac{1}{2}\cot\varphi + \frac{i}{2} & \frac{1}{2\sin\varphi} & 0 & \cdots \\ \frac{1}{2\sin\varphi} & -\cot\varphi & \frac{1}{2\sin\varphi} & \cdots \\ 0 & \frac{1}{2\sin\varphi} & -\cot\varphi & \frac{1}{2\sin\varphi}\cdots \\ & & \ddots & \\ \cdots & \frac{1}{2\sin\varphi} & -\cot\varphi & \frac{1}{2\sin\varphi} \\ \cdots & 0 & \frac{1}{2\sin\varphi} & -\frac{1}{2}\cot\varphi + \frac{i}{2} \end{pmatrix}.$$

$$(21)$$

Equation (21) allows one to reduce the infinite-range Hamiltonian (15) to the usual tight-binding Hamiltonian $\tilde{H}$ with the nearest-neighbor couplings and the eigenvalues $1/(\omega - \omega_0)$. While Eq. (21) is not obvious, it can be easily verified that it is compatible to the polariton dispersion law $\omega(K)$ equation (12) in the infinite structure (for $\delta\omega = \gamma = 0$). Namely, according to Eq. (12), $1/[\omega(K) - \omega_0]$ is proportional to $\cos K - \cos\varphi$. The $\cos K$ dispersion law corresponds to a tight-binding model with nearest-neighbor couplings (Bernevig and Hughes, 2013), which is exactly Eq. (21). Therefore, the infinite-range Hamiltonian (15) could be viewed as the tight-binding Hamiltonian (21) in disguise.

The distinction between long-range and tight-binding situations becomes more clear in the Bragg structure, with $\sin \varphi = 0$, where Eq. (21) is not applicable. Thus, the Bragg-spaced array seems to present the clearest manifestation of the long-range interaction.

The only nonzero imaginary elements of the matrix (21) are at the corners, for $n = m = 1$ and $n = m = N$. This is why the radiative decay rate vanishes for an infinite array: radiative losses are only through the array edges. It can be seen in Eq. (20) that the edge values of the wave function are on the order of $P_1 = P_N \propto N^{-3/2}$. The radiative decay rate is obtained in the first order of perturbation theory in the imaginary matrix elements $\mathrm{Im}\tilde{H}_{n,m}$ of Eq. (21). Namely, it is proportional to $\mathrm{Im}\tilde{H}_{1,1}P_1^2 \propto N^{-3}$. This is an alternative way to obtain the $\sim N^{-3}$ scaling of the radiative decay rate.

The approach based on the non-Hermitian Hamiltonian (15) can also be generalized to the non-Markovian case. To this end the phases $\varphi|m - n| \equiv \omega_0|z_m - z_n|/c$ should be replaced by $\omega|z_m - z_n|/c$. Physically, the Markovian approximation assumes that the light flight time is much smaller than all the other relevant timescales in the system. Therefore, it is typically valid for photon scattering on a single atom or on an array of closely spaced atoms. However, non-Markovian effects are still possible in this case. For example, they arise due to the finite bandwidth of the infinite photon wave packet, as studied by Fang, Ciccarello, and Baranger (2018).

c. Bragg-spaced arrays

The situation in which the atomic resonance frequency and array period d satisfy the resonant Bragg condition

$$d = \frac{m}{2}\lambda(\omega_0), \qquad m = 1, 2, \ldots, \qquad (22)$$

deserves special attention. In this case, the incident wave exhibits not only resonant reflection from each individual atom but also the Bragg diffraction: waves reflected from different atoms interfere constructively. The calculation in Fig. 8(b) indicates that the width of the polariton band gap increases when the array period approaches the resonant Bragg condition (22).

Bragg diffraction in arrays of resonant scatterers has been studied in substantially different setups. Historically, the first platform was probably presented by natural crystals, such as iron, where sharp resonances with the widths on the order of a meV exist for γ rays ($\hbar\omega \approx 14$ keV) exhibiting Mössbauer scattering on the nuclei. These crystals have been experimentally studied since the 1960s; see Hannon and Trammell (1999) and Kagan (1999). Artificial Bragg lattices for γ rays made from alternating layers of different isotopes have also been considered (Chumakov *et al.*, 1993). Significant progress has recently been made in this field (Röhlsberger *et al.*, 2010, 2012; Haber *et al.*, 2017, 2019) with the advent of high-brilliance synchrotron radiation sources; see also Röhlsberger and Evers (2021). While initially the researchers studied mainly the angular dependence of the reflectivity instead of its spectral properties (Chumakov *et al.*, 1993), modern technologies have enabled high-resolution spectroscopic demonstration of Bragg reflection from nuclear

multilayers (Haber *et al.*, 2016). In the 1990s, it has been independently proposed to use Bragg-spaced lattices of semiconductor quantum wells (Ivchenko, Nesvizhskii, and Jorda, 1994a, 1994b) and optical lattices of cold atoms (Deutsch *et al.*, 1995) for light. Some other examples of Bragg-spaced lattices with resonant scatterers include ring resonators (Yanik *et al.*, 2004), metallic gratings with plasmonic resonances (Taubert *et al.*, 2012), and dielectric cylinders with Mie resonances (Rybin *et al.*, 2015). A detailed comparison among cold atom systems, semiconductor lattices, and Mössbauer isotopes was given by Poddubny and Ivchenko (2013). It has also been theoretically suggested to consider Bragg lattices of atoms (Haakh, Faez, and Sandoghdar, 2016) and superconducting qubits coupled to the waveguide (Greenberg, Shtygashev, and Moiseev, 2021). The modification of Bragg conditions for the scattering of light from an array of atoms into the guided modes of a waveguide was analyzed by Olmos *et al.* (2021). Large Bragg reflection from atomic arrays trapped near a one-dimensional waveguide had already been demonstrated experimentally by Corzo *et al.* (2016) and Sørensen *et al.* (2016). These experiments are reviewed in more detail in Sec. IV.E.

We examine the polariton dispersion law in the close-to-Bragg regime in Fig. 9. Figure 9(c) presents the polariton dispersion law $\omega(K)$ calculated for the periods close to the Bragg value for $m = 1$. Figure 9(a) corresponds to the situation in which the period is smaller than the Bragg value. The dispersion features two band gaps: the polariton band gap in Eq. (14) below the atomic resonance and the usual photonic band gap at the frequency satisfying the Bragg condition $\omega d/c = \pi$. Figure 9(c) presents the opposite scenario where the Bragg band gap is located below the polariton one. In the
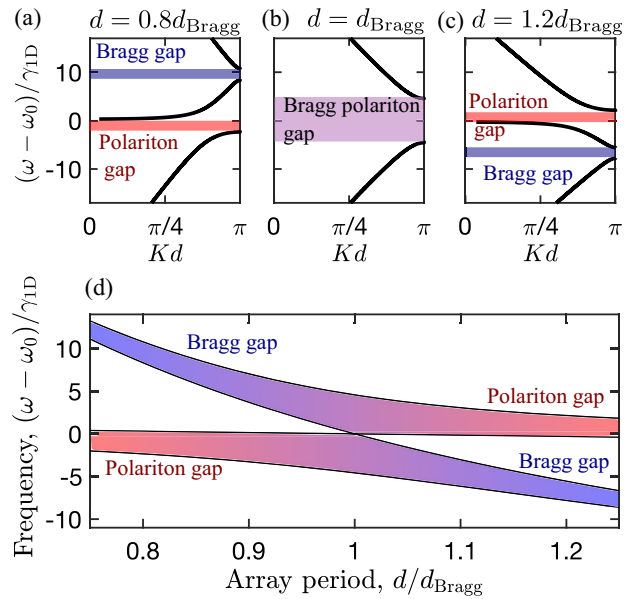

FIG. 9. Polariton dispersion in the atomic arrays with different periods. (a)–(c) Three different values of d/d_{Bragg}, with the values as indicated. Bragg and polariton band gaps are provided. (d) Dependence of the band gap positions on the period of the array. The calculation was performed for $\gamma_{\mathrm{1D}}/\omega_0 = 0.03$ and $\gamma = 0$.
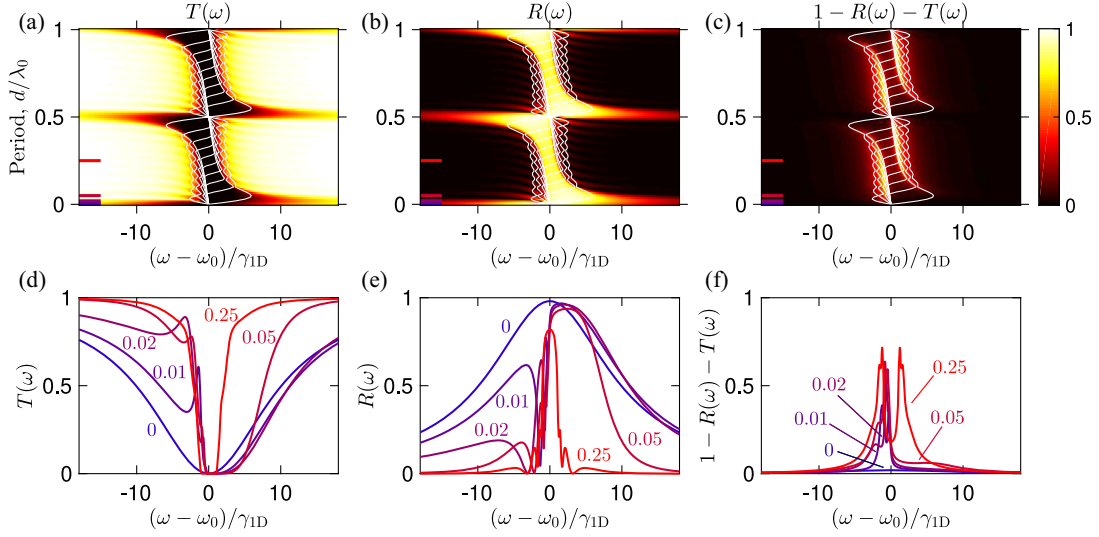
FIG. 10.   (a),(d) Transmission, (b),(e) reflection, and (c),(f) absorption spectra of the array of $N = 10$ atoms coupled to a waveguide, depending on the period of the array d. The bottom panels are calculated for four specific periods, indicated by corresponding dashes in the upper panels. The thin white lines in (a)–(c) show the real parts of the polaritonic eigenfrequencies ω^ν. The calculation was performed for $\gamma = 0.1\gamma_{1D}$ and $\gamma_{1D}/\omega_0 = 10^{-3}$. The value of the parameter d/λ_0 used for the calculations in (d)–(f) is indicated for each curve.

Bragg case illustrated in Fig. 9(b), the two band gaps fuse with each other and form a wide Bragg polariton band gap around the atomic resonance. The polariton dispersion law in Eq. (12) near the resonance can be described using the following equation:

$$\frac{Kd}{\pi} - 1 = \pm\sqrt{\left(\frac{\omega - \omega_0}{\omega_0}\right)^2 - \left(\frac{\Delta_{\text{Bragg}}}{\omega_0}\right)^2}, \qquad (23)$$

where the half-width of the polariton band gap is

$$\Delta_{\text{Bragg}} = \sqrt{\frac{2\gamma_{1D}\omega_0}{\pi}}. \qquad (24)$$

The gap half-width Δ_{Bragg} exceeds the radiative linewidth of the atomic resonance of γ_{1D} by a large factor of $\sim\sqrt{\omega_0/\gamma_{1D}}$. Hence, the light incident upon the Bragg-spaced array will exhibit a strong reflection in the wide spectral range $\omega_0 - \Delta_{\text{Bragg}} < \omega < \omega_0 + \Delta_{\text{Bragg}}$. However, this Bragg band gap will be manifested in reflection only if the number of atoms of the array is large enough, namely, exceeding

$$N^* \sim \frac{1}{m}\sqrt{\omega_0/\gamma_{1D}}. \qquad (25)$$

Indeed, the phase gained by light between two atoms in the Bragg-spaced array is an integer multiple of π. Thus, at first glance the distance does not matter and the Bragg-spaced array is equivalent to the array with $d = 0$. However, this analysis assumes the validity of the Markovian approximation when the time of flight of the photons through the array Nd/c is smaller than the inverse lifetime of the superradiant mode $1/(N\gamma_{1D})$. When the total length of the structure exceeds the wavelength $\sim\sqrt{\omega_0/\gamma_{1D}}/m$ times, as specified by Eq. (25), the

time of flight of the photons can no longer be ignored (Poshakinskiy, Poddubny, and Tarasenko, 2012) and the waveguide-mediated interaction between the atoms stops being instantaneous. Namely, for $N \gg 1/m\sqrt{\omega_0/\gamma_{1D}}$ the reflection coefficient is close to unity inside the Bragg band gap and quickly decays outside the gap.

In general, the previously considered collective eigenmodes can be observed as resonances in the reflection and transmission spectra. The amplitude reflection coefficient can be determined from the Hamiltonian (15) as

$$r = -i\gamma_{1D}\sum_{m,n=1}^{N} G_{mn}(\omega)e^{i\omega(z_n + z_m)/c}, \qquad (26)$$

and the transmission coefficient t is obtained by replacing z_m in Eq. (26) with $-z_m$ and adding unity. In Eq. (26) $G \equiv [\omega - H]^{-1}$ is the matrix Green's function of the atomic excitations. This follows from Eqs. (A13) and (A14) in Appendix A in the low excitation regime, where the nonlinear terms in Eq. (A9) can be ignored. An explicit solution for the Green's function of the finite periodic array was given by Voronov *et al.* (2007). The Green's function can be presented as the following expansion over the eigenmodes,

$$G_{mn} = \sum_{\nu=1}^{N} \frac{\psi_m^\nu \psi_n^\nu}{\omega - \omega^\nu}, \qquad (27)$$

and has resonances at the eigenfrequencies ω_ν. An equivalent way to calculate the reflection and transmission coefficients using the transfer matrix method is presented in Appendix B.

We present in Fig. 10 the dependence of the reflection, transmission, and absorption spectra on the period of the ten-atom array. The spectral features reflect the eigenfrequencies of the array (previously shown in Fig. 8): the positions of the

features correspond to the real parts of the eigenfrequencies, which are shown as thin white lines in Fig. 10. The spectral widths of the features correspond to the imaginary part.

When the distance between atoms is much smaller than the light wavelength or equal to a Bragg value (22), the reflection and transmission coefficients assume an especially simple form,

$$r_N = \frac{iN\gamma_{1D}}{\omega_0 - \omega - i(\gamma + N\gamma_{1D})},$$

$$t_N = 1 + r_N = \frac{\omega_0 - \omega - i\gamma}{\omega_0 - \omega - i(\gamma + N\gamma_{1D})}. \qquad (28)$$

The transmission and reflection spectra have a symmetric Lorentzian shape. The half width at half maximum of the transmission dip (reflection peak) is equal to $\gamma + N\gamma_{1D}$, and it scales linearly with the number of atoms N. This is the manifestation of the radiative decay rate of the collective Dicke superradiant state where the atoms are excited symmetrically. We stress here that the resonant transmission coefficient through the Bragg-spaced array $|t_N(\omega_0)|^2$ is given by $\gamma^2/(\gamma + N\gamma_{1D})^2$. This nonexponential dependence occurs because of the formation of the collective superradiant state. It cannot be captured by a concept of OD that assumes an independent light interaction with all atoms. However, Eqs. (28) for the Bragg-spaced array are valid in the Markovian approximation for $N \ll N^*$ while in long arrays and when the Lorentzian spectrum is saturated.

Detuning of the spacing from zero or a Bragg value leads to suppression of the reflection, and the optical spectra acquire narrow resonant features corresponding to the excitation of the subradiant modes. The reflection is at a minimum at the anti-Bragg condition $d = \lambda(\omega_0)/4$, when the interference between waves reflected from different atoms is destructive. Suppression of the reflection can be used for the selective radiance (Asenjo-Garcia, Moreno-Cardoner *et al.*, 2017).

Another important effect to mention here is disorder. Indeed, introducing small disorder in the Bragg array leads to the disturbance of the Bragg condition (22) suppresses the reflection and modifies the transmission. For strong disorder, collective effects are quenched. The coupling efficiency β and the OD become the main constituents of the transmission.

3. Two-photon scattering

a. Model and historical overview

We start with a general discussion of a quantum problem with two or more photons scattering on an ensemble of atoms coupled to a waveguide. Since a single two-level atom cannot be excited by two identical photons at the same time, the photon-photon interactions become crucial. This problem has become a perfect testing ground for different theoretical techniques, and we now review the development.

The study of photon-photon interactions and nonlinearity of the Maxwell's equations in vacuum due to the excitation of virtual electron-positron pairs is a cornerstone problem of quantum electrodynamics; see Liang and Czarnecki (2012). However, in relativistic quantum electrodynamics the solution is obtained perturbatively since the electron-photon interaction constant $\alpha = e^2/\hbar c \approx 1/137$ is a small parameter. On the

other hand, in the nonrelativistic quantum optical problem there is an exact analytical solution in all orders in the light-atom coupling parameter g, provided that the rotating wave approximation remains valid, that the array has zero spacing ($d = 0$), and that the free-space dipole-dipole coupling is neglected. One of the reasons why this is possible is that when atoms are located in the same point light excites only symmetric Dicke states of types

$$\frac{1}{N}\sum_m \sigma_j^\dagger |0\rangle, \quad \frac{1}{N^2}\sum_{m,n}\sigma_j^\dagger \sigma_m^\dagger |0\rangle, \quad \text{etc.} \qquad (29)$$

Historically, the quantum Dicke model in the rotating wave approximation was first diagonalized exactly by Rupasov and Yudson in 1984 using the Bethe *Ansatz* technique, which was initially developed in the context of condensed matter physics (Rupasov and Yudson, 1984; Yudson, 1985; Yudson and Reineker, 2008). Rupasov and Yudson noticed the similarity between the Dicke problem and the Kondo problem of electrons, with linear dispersion interacting with a single impurity. This was independently solved in the same year by Andrei (1980) and Vigman (1980) using the Bethe *Ansatz*. The Kondo model in turn has certain similarities to a model of one-dimensional boson gas with contact interactions that was solved by Lieb and Liniger in 1963 using an analogous Bethe *Ansatz* approach (Lieb and Liniger, 1963); see also the reviews of the Bethe *Ansatz* given by Batchelor (2007) and Faddeev (2013). The Kondo model with linear dispersion is also related to the spin-boson model (Leggett *et al.*, 1987), which is in turn equivalent to the problem involving a two-level system interacting with photons without the rotating wave approximation; see also Sec. III.A.4 for a discussion of the ultrastrong coupling regime. The details on the Bethe *Ansatz* used by Rupasov and Yudson (1984) are given in Appendix F. Much later the same answer as given by Rupasov and Yudson (1984) and Yudson (1985) was obtained by Shen and Fan (2007a, 2007b) for the particular case of two-photon scattering. Shen and Fan solved the Schrödinger equation directly in the Hilbert subspace with only two excitations. We present an analogous derivation in Appendix C. Next Liao and Law (2010) considered a related system with a two-level atom replaced by a nonlinear cavity. This approach was later extended to several photons using the path integral formalism (Shi and Sun, 2009; Shi, Fan, and Sun, 2011; Shi, Chang, and Cirac, 2015), which is discussed in Appendix E. The scattering has also been analyzed using the conventional input-output theory of quantum optics (Lalumière *et al.*, 2013; Caneva *et al.*, 2015). In both approaches (Shi and Sun, 2009; Shi, Fan, and Sun, 2011; Caneva *et al.*, 2015), the photon degrees of freedom are effectively traced out and the problem is solved in the atomic subspace of the full Hilbert space. The disadvantage of such a technique is that it is valid only in the Markovian approximation. This approximation seems reasonable for closely spaced atoms but can fail in a large array. Namely, the Markovian approximation sets all the phases gained by light when traveling the distance d between any two atoms $\omega_k d/c$ to $\omega_0 d/c$, and the introduced phase error $|\omega_k - \omega_0|d/c$ can become important for a large spacing (Zheng and Baranger, 2013; Fang, Zheng, and Baranger, 2014).

However, the path integral formalism also allows one to take the non-Markovian effects into account (Shi, Chang, and Cirac, 2015).

The photon scattering problem on an atomic array has also been solved using the diagrammatic Green's function techniques (Pletyukhov and Gritsev, 2012; Zheng and Baranger, 2013; Fang, Zheng, and Baranger, 2014; Laakso and Pletyukhov, 2014; Kocabaş, 2016; Schneider *et al.*, 2016). These can be separated into two types. The first type is based on the electron representation, which was inspired by the original Feynman approach to quantum electrodynamics. In this technique, photon absorption is viewed as the transition of an electron from the lower atomic state $|1\rangle$ to the upper one $|2\rangle$, as described using a Hamiltonian of the following type: $a_k c_2^\dagger c_1 +$ H.c., where c_1 and c_2 are the corresponding electron creation operators. The perturbation series for N closely spaced atoms can be summed exactly, and the original answer by Rupasov and Yudson can be recovered; see Appendix F. However, this approach fails for spatially separated atoms due to the appearance of extra diagrams (Kocabaş, 2016) and a closed-form solution cannot be obtained. In our opinion, the Green's function approach in the exciton representation developed by Zheng and Baranger (2013) and Fang, Zheng, and Baranger (2014) is currently the most practical technique. In this representation, the absorption of a photon by an atom leads to the creation of an exciton. It can work for both closely spaced and spatially separated atoms and is not restricted by the Markovian approximation. Another advantage is that it naturally handles multilevel atoms, and the two-level atom case is recovered as a particularly limiting case. Recently the Green's function technique was generalized to multiphoton scattering (Piasotski and Pletyukhov, 2021). The model with a multilevel atom strongly coupled to the waveguide photons is similar to the so-called irreversible quantum graph model, where a propagating wave is coupled to an oscillator (Smilansky, 2004; Gnutzmann and Smilansky, 2006).

b. Photon-photon correlations for $d = 0$

When the atomic array has zero spacing ($d = 0$), the two-photon scattering problem can be solved exactly; see Appendixes C–G for different equivalent derivations. We consider a coherent state of light $\exp(-\alpha^2/2 + \alpha a_{\varepsilon/c}^\dagger)|0\rangle$ incident from the left upon the atomic ensemble. Here ε is the frequency and we assume that the excitation amplitude is weak ($\alpha \ll 1$). The scattered two-photon state can then be given as (Poshakinskiy and Poddubny, 2016)

$$
\psi_{\text{scat}} = e^{-\alpha^2/2} \Big\{ |0\rangle + \alpha t(\varepsilon) a_{\varepsilon/c}^\dagger |0\rangle + \alpha r(\varepsilon) a_{-\varepsilon/c}^\dagger |0\rangle
$$
$$
+ \frac{\alpha^2}{2} [t^2(\varepsilon) a_{\varepsilon/c}^{\dagger,2} + r^2(\varepsilon) a_{-\varepsilon/c}^{\dagger,2} + 2r(\varepsilon) t(\varepsilon) a_{\varepsilon/c}^\dagger a_{-\varepsilon/c}^\dagger]|0\rangle
$$
$$
+ \frac{i\alpha^2}{4} \int_{-\infty}^\infty \frac{d\omega}{2\pi} M(\varepsilon - \omega, \varepsilon + \omega \leftarrow \varepsilon, \varepsilon)
$$
$$
\times (a_{(\varepsilon+\omega)/c}^\dagger + a_{-(\varepsilon+\omega)/c}^\dagger)(a_{(\varepsilon-\omega)/c}^\dagger + a_{-(\varepsilon-\omega)/c}^\dagger)|0\rangle \Big\}.
$$
$$(30)$$

In Eq. (30) we use the notation $M(\omega_1', \omega_2' \leftarrow \omega_1, \omega_2)$ for the matrix element describing the incoherent scattering process where the two incident photons have the frequencies ω_1 and ω_2, and the two scattered photons have the frequencies ω_1' and ω_2'. The first line of Eq. (30) describes the superposition of the vacuum state and the states where a single photon is either reflected or transmitted. The second line describes independent coherent scattering of the two photons. The last two lines in Eq. (30) describe their correlated incoherent scattering. One of the two scattered photons has the frequency $\varepsilon - \omega$, and the other one has $\varepsilon + \omega$. The total energy 2ε is conserved and equal to that of the incident photon pair. This process is characterized by the following scattering matrix, which is derived in Appendix D:

$$
M(\omega_1', \omega_2' \leftarrow \omega_1, \omega_2)
$$
$$
= 4N\gamma_{1D}^2 s(\omega_1) s(\omega_2) s(\omega_1') s(\omega_2')
$$
$$
\times \frac{(\varepsilon - \omega_0 + i\gamma)[\varepsilon - \omega_0 + i(N\gamma_{1D} + \gamma)]}{\varepsilon - \omega_0 + i(N-1)\gamma_{1D} + i\gamma}, \quad (31)
$$

where $s(\omega) = 1/[\omega_0 - \omega - i(\gamma + N\gamma_{1D})]$. The four s factors on the first line of Eq. (31) describe the resonances of incident and scattered photons with the single-excited superradiant Dicke state at $\omega = \omega_0 - i(\gamma + N\gamma_{1D})$. The factor on the second line describes the two-photon resonance when the average energy of two incident (or two scattered) photons is equal to the double-excited Dicke state in Eq. (29), $\varepsilon = \omega_0 - i\gamma - i(N-1)\gamma_{1D}$. Since double-excited states are present only for $N > 1$ atoms, this two-photon resonance in Eq. (31) cancels out with the corresponding term in the numerator for $N = 1$. Equation (31) also shows that incoherent scattering is partially suppressed when the array is excited exactly at the atomic resonance, so the absolute value of the factor $\varepsilon - \omega_0 + i(\gamma + N\gamma_{1D})$ in the numerator is at a minimum. This suppression can be qualitatively understood by analyzing the destructive interference of two different quantum pathways for a related process, the absorption of two photons by two different atoms (Muthukrishnan, Agarwal, and Scully, 2004), which is illustrated in Fig. 11. The process goes through an intermediate virtual state where only one of the two atoms is excited, either the first one or the second one. The sum of the matrix elements of these two processes is proportional to

$$
\frac{1}{\omega_1 - \omega_0} + \frac{1}{\omega_2 - \omega_0}
$$

and vanishes for $(\omega_1 + \omega_2)/2 \equiv \varepsilon = \omega_0$.

The wave function in Eq. (30) allows one to calculate coherent photon reflection and transmission coefficients up to the linear order in the incident light power $\sim c\alpha^2/L$. The transmission coefficient is given by

$$
T_{\text{coh}} = |t|^2 - \frac{c\alpha^2}{L} \text{Im}[M(\varepsilon, \varepsilon \leftarrow \varepsilon, \varepsilon) t^*(t^* + r^*)], \quad (32)
$$

where t and r are coherent single-photon amplitudes of the transmission and reflection coefficients, respectively. The coherent reflection coefficient R_{coh} is obtained by replacing
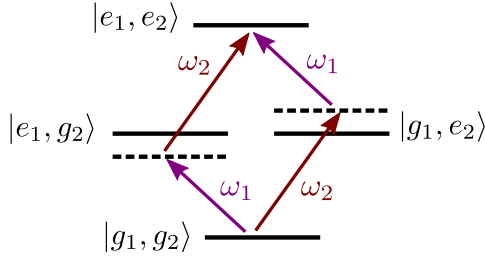
FIG. 11. Two destructively interfering pathways for the absorption of two photons by two different atoms.

FIG. 12. Schematics of single- and two-photon scattering on a two-level atom under resonant excitation.

t with *r* in Eq. (32). One can verify that, in the case of vanishing nonradiative decay, the energy flux conservation holds ($R_{\rm coh} + T_{\rm coh} + I_{\rm incoh} = 1$), where

$$I_{\rm incoh} = \frac{c\alpha^2}{L} \int_{-\infty}^{\infty} \frac{d\omega}{2\pi} |M(\varepsilon - \omega, \varepsilon + \omega \leftarrow \varepsilon, \varepsilon)|^2 \quad (33)$$

is the total incoherent scattering rate.

Insight into the two-photon scattering process can be obtained from the time-dependent, second-order photon-photon correlation functions

$$g_\nu^{(2)}(\tau) = \frac{\langle a_\nu^\dagger(0) a_\nu^\dagger(\tau) a_\nu(\tau) a_\nu(0)\rangle}{|\langle a_\nu^\dagger(0) a_\nu(0)\rangle|^2}, \quad (34)$$

where $\nu = \rightarrow, \leftarrow$. Zero-time correlation functions $g_\nu^{(2)}(0)$ are equal to the ratio of the probability of two photons being emitted together to the probability of their independent emission and thus determine the emission statistics. Calculating the expectation values with the help of Eq. (30), we find that

$$g_\rightarrow^{(2)}(\tau) = \left| 1 + \frac{i}{2t^2(\varepsilon)} \int_{-\infty}^{\infty} \frac{d\omega}{2\pi} e^{-i\omega\tau} M(\varepsilon - \omega, \varepsilon + \omega \leftarrow \varepsilon, \varepsilon) \right|^2 \quad (35)$$

in transmission geometry. The correlation function $g_\leftarrow^{(2)}(\tau)$ for reflected photons is obtained by replacing $t(\varepsilon)$ with $r(\varepsilon)$ in Eq. (35). The integrals can be straightforwardly evaluated analytically using the Cauchy theorem.

The calculation results are most easily interpreted when only an $N = 1$ atom is excited at the resonance ($\varepsilon = \omega_0$). It is then straightforward to show from Eq. (35) that $g_\rightarrow^{(2)}(0)$ is diverging (photon bunching) and $g_\leftarrow^{(2)}(0) = 0$ (antibunching). The bunching occurs because the atom becomes transparent after having absorbed a photon. Thus, a single photon cannot pass through the atom, while a pair of photons can. The antibunching in reflection geometry stems from the fact that a single two-level atom cannot accommodate two photons at the same time and hence cannot emit two photons simultaneously. The scattering of a single photon and two photons on an atom is illustrated in Fig. 12, where we show an incident state, an intermediate virtual state after one of the photons has been absorbed, and output states. The two-photon output state given by Eq. (30) is an entangled state of two photons
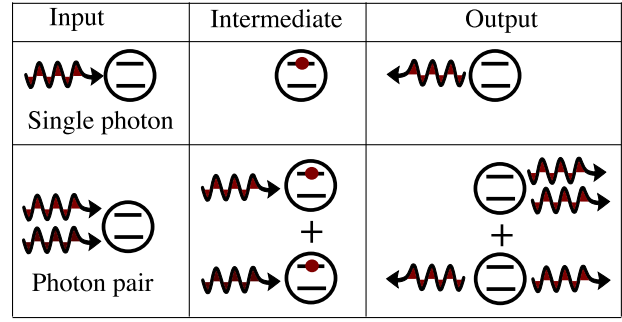
propagating to the right and two photons propagating in opposite directions.

It is instructive to analyze the equal-time photon-photon correlation function $g^{(2)}(0)$, depending on the number of atoms in the array. For resonant excitation ($\varepsilon = \omega_0$) this is given by

$$g_\leftarrow^{(2)}(0) = \left(\frac{1 - 1/N}{1 - \gamma_{\rm 1D}/(\gamma + N\gamma_{\rm 1D})} \right)^2,$$
$$g_\rightarrow^{(2)}(0) = \left(\frac{1 - \gamma_{\rm 1D}/\gamma}{1 - \gamma_{\rm 1D}/(\gamma + N\gamma_{\rm 1D})} \right)^2. \quad (36)$$

The dependence of the photon-photon correlation functions (36) on the atom number N and the ratio of the decay rates is plotted in Fig. 13. One atom in reflection geometry demonstrates full antibunching $g_\leftarrow^{(2)}(0) = 0$ for any value of $\Gamma > 0$ [see Fig. 13(a)] since it cannot host two photons. However, this antibunching is already fully suppressed for $N = 2$ atoms [$g_\leftarrow^{(2)}(0) \approx 1$]. The naive physical explanation is simple: the array of $N > 1$ atoms can host two photons, so the photon blockade is not manifested. In transmission geometry the dependence on N is weak. The transmitted photons are bunched (antibunched) for small (large) values of $\gamma \ll \gamma_{\rm 1D}$; see Fig. 13(b).
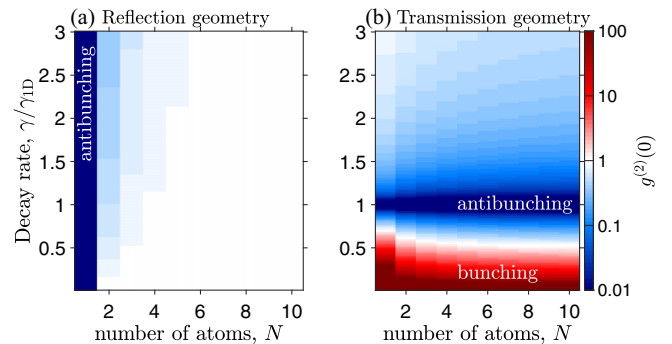

FIG. 13. Dependence of the photon-photon correlation function $g^{(2)}(0)$ on the number of atoms N and on the ratio of nonradiative and radiative damping rates $\gamma/\gamma_{\rm 1D}$ calculated with Eq. (36). (a), (b) Reflection and transmission geometries, respectively, calculated for the light incident at the resonant frequency $\varepsilon = \omega_0$ of the two-level atoms ($U \rightarrow \infty$).

c. Array with nonzero spacing, d > 0

In the case of nonzero spacing, it is not possible to write an explicit analytical solution of the type of Eq. (31), but the scattering can be considered using the generalization of the Green's function method (Zheng and Baranger, 2013) that is described in detail in Appendix G. The two-photon wave function is obtained by replacing the last term in Eq. (30) with

$$\sum_{\mu,\nu=\pm} \int_{-\infty}^{\infty} \frac{d\omega}{2\pi} M_{\mu\nu}(\omega, 2\varepsilon - \omega \leftarrow \varepsilon, \varepsilon) a^{\dagger}_{\mu\omega/c} a^{\dagger}_{\mu(2\varepsilon-\omega)/c} |0\rangle, \quad (37)$$

where the scattering kernel is given by

$$M_{\mu\nu}(\omega'_1, \omega'_2) = -2i\gamma^2_{1D} \sum_{m,n=1}^{N} s^{\mu}_n(\omega'_1) s^{\nu}_n(\omega'_2) Q_{nm} s^{+}_m(\varepsilon) s^{+}_m(\varepsilon), \quad (38)$$

with $s^{\pm}_m(\omega) = \sum_m G_{mn}(\omega) e^{\pm i(\omega/c)z_n}$ and

$$Q = \Sigma^{-1}, \qquad \Sigma_{nm} = \int_{-\infty}^{\infty} \frac{d\omega}{2\pi} G_{nm}(\omega) G_{nm}(2\varepsilon - \omega). \quad (39)$$

Equation (38) is valid beyond the Markovian approximation. However, in the Markovian approximation it can be further simplified. Specifically, the poles ε of the matrix Q in Eq. (39) correspond to the complex energies of the double-excited states

$$|\psi\rangle = \sum_{m,n=1}^{N} \psi_{mn} \sigma^{\dagger}_m \sigma^{\dagger}_n |0\rangle \quad (40)$$

$(\psi_{mn} = \psi_{nm})$ of the effective non-Hermitian atomic Hamiltonian (8). The corresponding two-photon Schrödinger equation for the amplitude ψ_{nm} can be obtained by substituting the *Ansatz* (40) into the general Schrödinger equation $H_{\rm eff}|\psi\rangle = 2\varepsilon|\psi\rangle$. More details are presented in Appendix G.

We now discuss the spatial structure of the double-excited states, which is surprisingly diverse. On the applied side, these are the states responsible for spatial and time dependence of the two-photon correlations and spatial entanglement. For example, recently observed tunable bunching and antibunching (Prasad *et al.*, 2020) are enabled by the correlated double-excited states; see also Sec. III.B.4. On the more fundamental side, we now show that the double-excited states uncover drastically different regimes of particle-particle interaction. Namely, eigenstates of the same array of atoms in a waveguide manifest at the same time fermionization, interaction-induced localization, quantum Hall phases with topological edge states, Hofstadter's butterfly, and quantum chaos. The main reason why this seemingly simple two-body problem is so rich is the strongly nonlinear and nonparabolic polariton dispersion shown in Fig. 6, with the slow polariton group velocity decreasing near the resonance frequency. The inter-actions between the particles with the polaritonic dispersion differ significantly from the more commonly studied parabolic dispersion case (Girardeau, 1960; Lieb and Liniger, 1963).
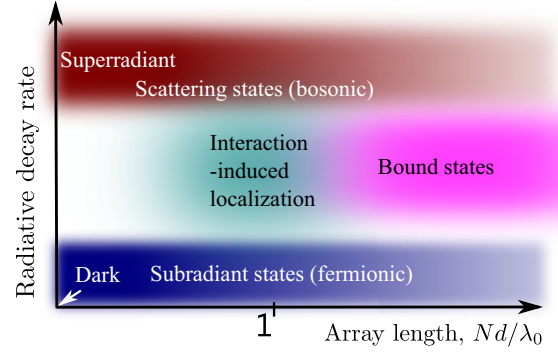

FIG. 14. Schematic phase diagram showing different possible types of two-polariton states in an array of atoms coupled to a waveguide, depending on their radiative decay rate and the ratio of the array length Nd to the wavelength at the atom frequency. Wave functions for these states are shown in Fig. 15.

We present in Fig. 14 a general simplified phase diagram distinguishing among domains of different double-excited states depending on their radiative lifetime and on the array length. Figure 15 shows the characteristic wave functions of these states. The real-space joint two-polariton probabilities $|\psi_{nm}|^2$ are shown in the top row. The second row presents the Fourier transforms $|\psi(k)^2| \equiv \sum_{m=1}^{N} |\psi_m(k)|^2/N$, where $\psi_m(k) = \sum_{n=1}^{N} \psi_{mn} e^{ikn}$, and the bottom row illustrates these Fourier transforms schematically. We now discuss these states in detail.

As with the single-photon states, if the distance between atoms is vanishing, the only double-excited state probed by light is the symmetric superradiant state (top left corner of Fig. 14). The wave function ψ_{nm} for this state is constant if $n \neq m$ and $\psi_{nn} = 0$ due to the photon blockade, as can be seen in Fig. 15(a). The double-excited superradiant state has the complex eigenfrequency $\varepsilon = \omega_0 - i(N-1)\gamma_{1D} - i\gamma$, which can also be found from the resonance of Eq. (31).

When the distance between atoms becomes nonzero, other states with more interesting spatial profiles become accessible by light. The simplest one is the scattering state of two polaritons shown in Fig. 15(b). Typically, scattering states are realized when the wave vectors of both polaritons k are much smaller than the edge of the Brillouin zone π; see the bottom panel of Fig. 15(b). In this case, both polaritons have relatively high group velocity, so the role of their interaction is weak. These two polaritons can be thought of as quasi-independent. The wave function of a single-polariton state in a finite array is a standing wave $P^{(\xi)}_n \propto \cos[k_{\xi}(n-1/2)]$. Hence, the wave function of the two-polariton scattering state is approximately described by a symmetrized product of two standing waves, slightly modified by the interaction that sets $\psi_{nn} = 0$, namely,

$$\psi_{mn} \approx \frac{1}{\sqrt{2}} (P^{(\xi)}_m P^{(\xi)}_n + P^{(\xi')}_m P^{(\xi)}_n)(1 - \delta_{mn}). \quad (41)$$

For example, the state in Fig. 15(b) corresponds to $k_{\xi} = k_{\xi'} = \pi/N$.
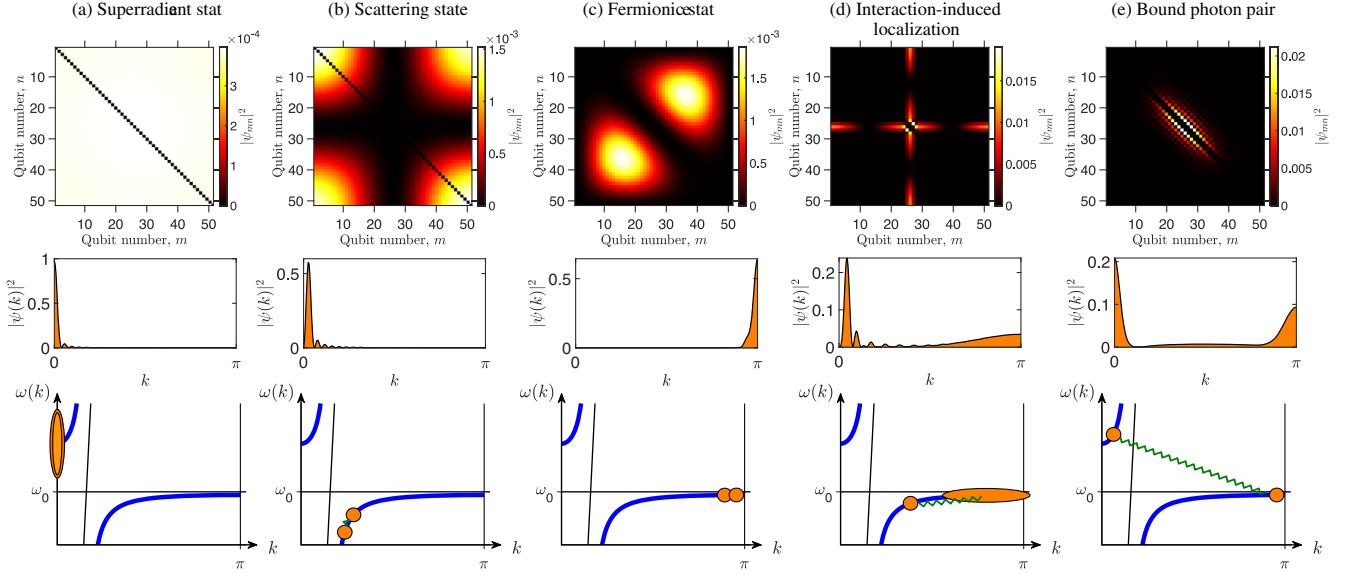
FIG. 15.   Examples of different double-excited states in the finite array of $N = 51$ two-level atoms coupled to a nonchiral waveguide. Top row: real-space two-polariton wave functions $|\psi_{nm}|^2$. Second row: Fourier transforms $|\psi(k)|^2$. (b)–(e) Bottom panels: wave vectors of two polaritons corresponding to the two-polariton wave functions in the upper panels (not in scale). The calculation was performed for the array periods (a),(b),(d) $\omega_0 d/c = 0.01$ and (c),(e) $\omega_0 d/c = 0.4$. The complex energies of the displayed states are $(\varepsilon - \omega_0)/\gamma_{1D} = 8.4 - 48.9i$, $-5.0 - 1.0i$, $-0.2 - 4 \times 10^{-6}i$, and $1.9 - 2 \times 10^{-6}i$ for (a)–(e), respectively.

In the case of zero spacing between atoms $d = 0$, all states except the superradiant one are fully dark and degenerate ($\varepsilon = \omega_0 - i\gamma$) (bottom left corner of Fig. 14), and they become subradiant for $d > 0$. Contrary to well-known single-excited subradiant states, the spatial structure of double-excited subradiant states has only recently been revealed (Albrecht *et al.*, 2019; Zhang and Mølmer, 2019). Remember that single-excited subradiant states are just standing waves with the wave vectors k close to the edge of the Brillouin zone; see Eq. (20). The polaritonic dispersion law given by Eq. (12) near the Brillouin zone edge is parabolic, $\omega(k) - \omega(\pi) \approx -\varphi \gamma_{1D}(k - \pi)^2/8$, with $\varphi = \omega_0 d/c$; see also Fig. 6. The two polaritonic excitations described by the Schrödinger equation (G15) exhibit contact repulsion due to the photon blockade. The problem of interacting bosons with parabolic dispersion and contact repulsion is well known in the condensed matter physics and was solved by Lieb and Liniger (1963) by means of the Bethe *Ansatz*. It has been shown that strong repulsion between bosons emulates the Pauli exclusion principle. Specifically, the two-particle wave function is proportional to the antisymmetric combination of two single-particle wave functions, i.e.,

$$\psi_{mn} \propto \frac{1}{\sqrt{2}} \times \begin{cases} P_m^{(\xi)} P_n^{(\xi')} - P_m^{(\xi')} P_n^{(\xi)} & (m \geq n), \\ -(P_m^{(\xi)} P_n^{(\xi')} - P_m^{(\xi')} P_n^{(\xi)}) & (n \leq m) \end{cases} \quad (42)$$

[compare with the scattering state (41)]. While the wave function (42) still has bosonic symmetry ($\psi_{nm} = \psi_{mn}$), the corresponding probability distribution $|\psi_{nm}|^2$ in the real space is the same as it is for noninteracting spinless fermions. This is called fermionization. The top panel of Fig. 15(c) shows the probability distribution for the most subradiant state calculated numerically in the array of $N = 51$ qubits. Its spatial

structure is well captured by the *Ansatz* (42) with $k_\xi = \pi - \pi/N$ and $k_{\xi'} = \pi - 2\pi/N$. The bottom panel of Fig. 15(c) illustrates the origin of this fermionic state as a result of interaction of two polaritons with the wave vectors close to the edge of the Brillouin zone.

There is also an interesting mesoscopic regime when the length of the array is of the order of its wavelength $N\omega_0 d/c \sim 1$. It has been predicted that the interaction between the two polaritons can make one of them localized, even though all single-polariton states are delocalized and the structure has no disorder (Zhong *et al.*, 2020). Specifically, the first polariton forms a standing wave that drives localization of the second polariton in the node (or in the antinode) of this wave. Since the two polaritons are indistinguishable, at the same time the second polariton drives localization of the first one, and the two-polariton wave function can be approximately described by the *Ansatz*

$$\psi_{mn} \propto \psi_{\text{loc}}(n)\psi_{\text{free}}(m) + \psi_{\text{loc}}(m)\psi_{\text{free}}(n). \quad (43)$$

In Eq. (43) the state $\psi_{\text{loc}}(n)$ is localized at several atoms and the state $\psi_{\text{free}}(n)$ is a standing wave. The localization is so strong because of the low group velocity at large wave vectors. In another words, polaritons with $k \gg \omega_0/c$ have a large effective mass and are easily localized through interactions; see Zhong *et al.* (2020) for more details. The situation becomes even more interesting when the standing wave has multiple nodes. In this case the first polariton experiences both the lattice potential and the periodic standing wave potential, induced by the interaction with the second polariton and determined by $|\psi_{\text{free}}(n)^2|$. The one-dimensional problem of the particle in this potential with two periods is similar to the Aubry-André-Harper model that can in turn be mapped to

the two-dimensional quantum Hall problem on a lattice (Kraus *et al.*, 2012; Poshakinskiy *et al.*, 2014). Thus, it turns out that the WQED setup hosts an analog of the topological quantum Hall phase, which arises solely due to the interactions without any applied magnetic field. This phase manifests an analog to Hofstadter's butterfly and also topological two-polariton edge states, when one of the polaritons is localized at the edge of the structure and another one forms a standing wave (Poshakinskiy *et al.*, 2021).

Yet another type of two-polariton states realized in relatively long structures with the thickness of many wavelengths is a state where two polaritons form a bound pair that can propagate as a whole and is characterized by a certain center-of-mass momentum K. In the finite array, this pair forms a standing wave

$$\psi_{mn} \approx \cos\left(K\frac{m+n}{2}\right)\psi_{\text{bound}}(|m-n|), \qquad (44)$$

where the relative motion wave function $\psi_{\text{bound}}(|m-n|)$ decays exponentially with distance. An example of this state is shown in Fig. 15(e). There are two types of bound two-photon states (Zhang, Yu, and Mølmer, 2020). The first type corresponds to one of the two polaritons in the upper polaritonic branch and one in the lower polaritonic branch, as shown in the lower panel of Fig. 15(e). Its center-of-mass dispersion is sensitive to the ratio of the array period to the light wavelength at the atomic resonance $d/\lambda(\omega_0)$. Namely, there is a "magic value" $d = \lambda(\omega_0)/12$ where the center-of-mass dispersion depends on the wave vector near the edge of the Brillouin zone as $(K-\pi)^4$ and the quadratic term vanishes (Poddubny, 2020). This means that the bound pair acquires infinite mass and that it is hard for photons to escape the array, so their radiative lifetime increases dramatically (Zhang, Yu, and Mølmer, 2020). Another type of bound pair states is formed by both polaritons in the upper branch. A generalization of two-photon states shown in Fig. 15 for the three-photon case was recently given by Zhong and Poddubny (2021).

We also note that the considered two-body problem is generally not integrable, which means, in particular, that none of the simple *Ansätze* (41)–(44) are exact. The intermediate regime, where none of these *Ansätze* hold, corresponds to an interaction-induced quantum chaos (Poshakinskiy, Zhong, and Poddubny, 2021). By this we mean that the two-polariton wave function becomes highly irregular in the real space and also occupies a large region of the reciprocal space.

4. Ultrastrong coupling regime

While in the majority of cases the rotating wave approximation is justified (i.e., the characteristic energy of the qubit-photon interaction g is much less than the qubit transition frequency ω_0), the breakdown of this approximation was recently demonstrated in the circuit QED systems based on superconducting qubits (Niemczyk *et al.*, 2010; Forn-Díaz *et al.*, 2017), where $g/\omega_0 > 0.1$ was demonstrated. From the theory side, departure from the rotating wave approximation (A4) leads to the Hamiltonian

$$H = \sum_m \omega_0 \sigma_z^{(m)} + \frac{1}{\sqrt{L}}\sum_k \omega_k a_k^\dagger a_k + \sum_{m,k} g_k \sigma_x^{(m)}(a_k + a_k^\dagger),$$

$$(45)$$

where $\sigma_x^{(m)} = \sigma_m + \sigma_m^\dagger$. The account for the antiresonant terms $\sigma^{(m)} a_k, \sigma^{\dagger(m)} a_k^\dagger$ lifts the conservation of the total number of excitations. Thus, the Hilbert space of the solutions can no longer be factorized to the blocks with the fixed number of excitations. The analytical solution has been obtained only for the simplest case with a single qubit and a single photonic mode, which is known as the Rabi model (Braak, 2011). The ground state of the Rabi model is a squeezed vacuum state comprising multiple photonic Fock states. The modification of the ground state is the distinct feature of the ultrastrong coupling regime that persists in the multimode and multispin case and may lead to the cavity-mediated phase transitions (Ashida *et al.*, 2020). Note that the Hamiltonian (45) is not gauge invariant. To restore the gauge invariance, an additional term corresponding to the photon occupation number and coupling strength should be added (Kockum *et al.*, 2019). While this term can be neglected at moderate coupling strengths, its omission in the ultrastrong coupling regime can lead to unphysical phase transitions.

In the multimode case, the system resembles the spin-boson model (Leggett *et al.*, 1987) and its multiple spin counterparts. The central quantity in the spin-boson model is the spectral distribution of the coupling strength J:

$$J(\omega) = \frac{2\pi}{\sqrt{L}}\sum_k |g_k|^2 \delta(\omega - \omega_k). \qquad (46)$$

The specific shape of the spectral distribution function $J(\omega)$ depends on a specific geometry of the waveguide. One particularly explored case corresponds to the so-called Ohmic bath $J(\omega) = \alpha\omega f(\omega/\omega_c)$, where $f(x)$ is the cutoff function that decays quickly as $x > 1$, ω_c is the cutoff frequency usually defined by the waveguide bandwidth, and α is the dimensionless coupling constant. It has been discussed that the spin-boson model supports various quantum phase transitions as a function of the coupling strength (Le Hur, 2010). Moreover, for certain waveguide dispersions and coupling coefficients g_k, the model can be directly mapped to the Kondo problem (Blume, Emery, and Luther, 1970) having an exact analytical solution. We note that the applicability of the two-level model for superconducting qubits remains a subject of discussion. For example, Kaur *et al.* (2021) predicted that the intrinsic multilevel structure of the qubits drastically restricts the validity of the spin-boson paradigm.

The properties of the spin-boson model become especially interesting in the presence of disorder. In the absence of disorder at the threshold, when atom-photon coupling strength exceeds a certain threshold, all spins become aligned, forming a ferromagnetic phase while being an analog of the paramagnetic phase below threshold. The disordered multimode Dicke model also features a quantum spin-glass phase where a random linear combination of the cavity modes becomes superradiant (Gopalakrishnan, Lev, and Goldbart, 2011; Strack and Sachdev, 2011; Rotondo, Cosentino Lagomarsino, and Viola, 2015).

There are two general approaches to the theoretical treatment of the WQED regime. Within the first approach, the waveguide Hamiltonian is written in the real-space representation, with a subsequent application of the matrix product states to find the eigenspectrum of the system (Peropadre *et al.*, 2013; Sánchez-Burillo *et al.*, 2014; Wall, Safavi-Naini, and Rey, 2016; Mahmoodian, 2019). Alternatively, one may introduce the unitary transformation, which asymptotically transforms the Hamiltonian to that with a conserved number of excitations (Shi, Chang, and García-Ripoll, 2018; Sánchez-Burillo *et al.*, 2019; Ashida, İmamoğlu, and Demler, 2022). This resembles the polaron transformation widely used in the theoretical treatment of electron-phonon interactions in condensed matter (Silbey and Harris, 1984). For a single-qubit case of the Hamiltonian (45), the transformation operation U_p reads

$$U_p = \exp\left[-\sigma_x \sum_k (f_k a_k^\dagger - f_k^* a_k)\right]. \qquad (47)$$

Under the transformation, the ground state transforms to $|GS\rangle = U_p|0\rangle$, where $|0\rangle$ is the vacuum state. The parameters f_k are obtained using the minimization of the ground state energy yielding the equations

$$f_k = \frac{1}{\sqrt{L}} \frac{g_k}{\Delta_r + \omega_k}, \qquad \Delta_r = \omega_0 e^{-2\sum |f_k|^2}. \qquad (48)$$

The transformed Hamiltonian reads

$$\begin{aligned} H' = \Delta_r \sigma_z + \sum_k a_k^\dagger a_k - 2\Delta_r(\sigma\hat{A}^\dagger + \sigma^\dagger \hat{A}) \\ - 2\Delta_r \sigma_z \hat{A}^\dagger \hat{A} + E_0 + \mathcal{O}(f^3), \end{aligned} \qquad (49)$$

where $\hat{A} = \sum f_k a_k$. Up to the terms that are quadratic in the coupling constant, the transformed Hamiltonian conserves the number of excitations. Therefore, this Hamiltonian can be treated using projection to the subspace with a fixed number of excitations, similar to the case of WQED in the rotating wave approximation. The polaron picture described by the Hamiltonian (49) is particularly useful to gain physical insight on the origin of the peculiar effects occurring in the ultrastrong regime. Since the ground state $|GS\rangle$ comprises the Fock states with nonzero photon occupation, the system hosts virtual photonic excitations even in the ground state. These can be realized by the nonadiabatic change of the coupling constant, resulting in photon emission from the vacuum state in the ultrastrong coupling regime (Sánchez-Burillo *et al.*, 2019). Moreover, the ultrastrong coupling leads to the inelastic Raman scattering of the single photons from the WQED system (Sánchez-Burillo *et al.*, 2014), and even conversion of the single incoming photon to multiple photons of lower energy (Belyansky *et al.*, 2021). Elastic scattering also gets substantially modified in the ultrastrong coupling regime. Shi, Chang, and García-Ripoll (2018) obtained the following expressions for the coherent elastic reflection and transmission coefficients r_k and t_k:

$$t_k = 1 + r_k, \qquad r_k = \frac{i(\omega_k + \Delta_r)\mathrm{Im}\Sigma(\omega_k)}{(\omega_k - \Delta_r)\Delta_r - (\omega_k + \Delta_r)\Sigma(\omega_k)}. \qquad (50)$$

The self-energy $\Sigma(\omega) = \delta_L(\omega) - i\gamma_{1D}(\omega)$ includes the Lamb shift $\delta_L(\omega)$ and the renormalized decay rate $\gamma_{1D}(\omega)$ given by

$$\delta_L(\omega) = 2\Delta_r^2 \mathcal{P} \int \frac{dk}{2\pi} \frac{f_k^2}{\omega - \omega_k}, \qquad (51)$$

$$\gamma_{1D}(\omega) = \Delta_r^2 f_{k'}^2 |\partial \omega_k / \partial k|_{k=k'}^{-1}. \qquad (52)$$

In the weak coupling limit, $\delta_L \approx 0$ and $\gamma_{1D}(\omega) \approx \gamma_{1D}(\omega_0) \equiv \gamma_{1D}$. Thus, Eqs. (50) reduce to the conventional expressions for the qubit reflection and transmission [Eqs. (28) for $N = 1$].

5. Multilevel atoms

Thus far we have considered an idealized situation of a two-level atom coupled to a single propagating waveguide mode. The two-level approximation is reasonable for superconducting qubits, but many modern WQED experiments are realized with ^{133}Cs or ^{87}Rb atoms, which have a complex degenerate multilevel structure.

In this section, we consider a cesium atom initially prepared at its hyperfine structure level $F_g = 4$ of the ground state; see Fig. 16(a). We assume a single photon propagating through the nanofiber with a frequency ω close to the atomic resonance frequency ω_0 of the transition $|F_g = 4\rangle \rightarrow |F_e = 5\rangle$ in the D_2 line. Here F_g and F_e are the total angular moments of the $6S_{1/2}$ ground state and the $6P_{3/2}$ excited state, respectively. Consideration of the chosen transition allows one to avoid any additional influence of the hyperfine structure of the excited state due to the selection rules. Therefore, the magnetic sublevels $e_{M'}$ and g_M of the hyperfine excited $F_e = 5$ and the ground $F_g = 4$ states form a closed set. However, experimentally, the multilevel system shown in Fig. 16(a) can still be reduced to a two-level system. This can first be done by applying a magnetic field that leads to the splitting of Zeeman sublevels along the magnetic field direction; see Sayrin *et al.* (2015). In this case, all transitions have different frequencies; see Fig. 16(b). As a result, a propagating photon is resonant to only one transition. Another way to reduce the number of considered levels in the atomic system is based on the optical trapping technique; see Scheucher *et al.* (2016). In this case, one can transfer atoms from all Zeeman sublevels to one (an edge one where $g_M = -4$ and $g_M = 4$ or a middle one $g_M = 0$); see Fig. 16(c). For each possible photon polarization, the atom can then be considered as a two-level one.

The case in which no magnetic field is applied and the optical trapping technique is not used is more involved. For the first time, spontaneous emission of a multilevel atom near an optical waveguide was calculated by Le Kien *et al.* (2005). It was shown that the multilevel structure of a real atom modifies its decay rate. Here we summarize the results of that paper.

The total decay rate of one Zeeman sublevel of the excited state is given by the sum $\Gamma_{ee'}^{\mathrm{tot}} = \Gamma_{ee'}^{1D} + \Gamma_{ee'}^{\mathrm{rad}}$, where $\Gamma_{ee'}^{1D}$ and
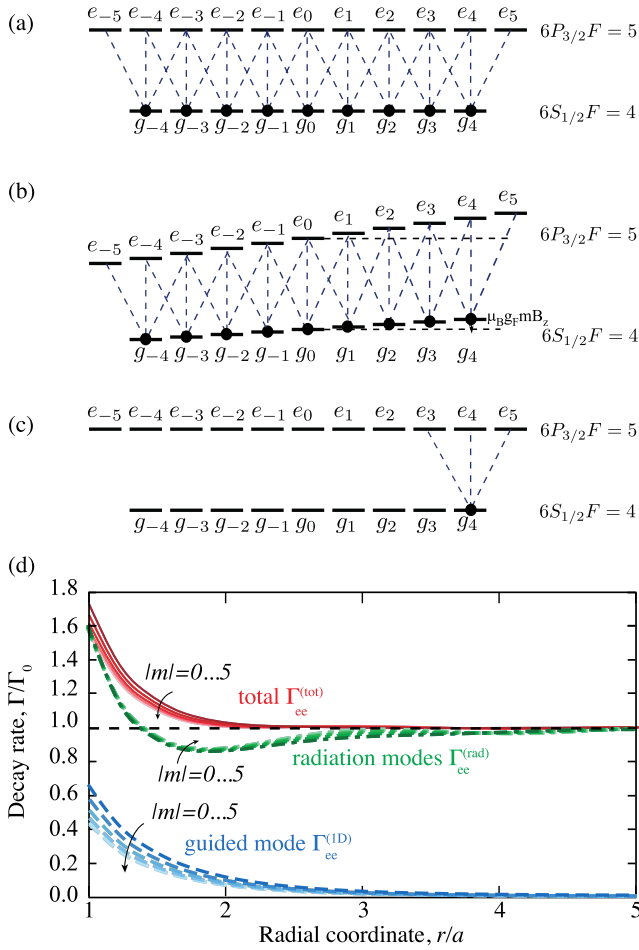
FIG. 16. (a)–(c) Schematics of the $|6S_{1/2}F = 4\rangle \rightarrow |6P_{3/2}F = 5\rangle$ transition in the D_2 line of a ^{133}Cs atom. (b) Level structure of the $|F_g = 4\rangle \rightarrow |F_e = 5\rangle$ transition of ^{133}Cs in a magnetic field. (c) Atoms trapped in the edge state $|F_g = 4, g_M = 4\rangle$. (d) Spontaneous emission rates for various magnetic sublevels of the excited state $|6P_{3/2}F' = 5\rangle$ of a ^{133}Cs atom. Blue dashed, green dash-dotted, and red solid lines show the rates of emission into guided modes, radiation modes, and total decay rates as functions of the atom distance from the fiber center. Different lines of each plot correspond to different Zeeman sublevels of the excited state. The fiber radius was chosen as $a = 200$ nm. The wavelength of the D_2 line of ^{133}Cs is $\lambda_0 = 852$ nm. The refractive indexes of the fiber and the vacuum clad are $n_1 = 1.45$ and $n_2 = 1$, respectively. The decay rates are normalized to the free-space decay rate Γ_0.

$\Gamma^{\mathrm{rad}}_{ee'}$ describe spontaneous emission into the guided and radiation modes, respectively. In Fig. 16(d), one can see the spatial dependence of the spontaneous emission rates for various magnetic sublevels $|e\rangle = |6P_{3/2}F' = 5\rangle$ in the guided modes, radiation modes, and both types of modes. The calculation demonstrates that the efficiency of the emission into the waveguide mode quickly decays with the distance from the atoms to the waveguide surface. For the atoms located exactly at the surface, the total spontaneous decay rate increases by the Purcell factor ~ 1.5 with respect to the free-space value Γ_0, and the fraction of emission into the waveguide mode is about $\beta \sim 0.3$. When the distance from the atoms to the surface becomes larger than the fiber radius, the

total decay rate is not much different from that in free space, and the β factor drops below 10%.

The presence of off-diagonal elements such as $\Gamma^{\mathrm{tot}}_{ee'}$, with $e \neq e'$, is a characteristic difference from the case of two-level atoms. They describe the decay rate of the cross-level coherence and arise only in the framework of a multilevel atom model. Knowledge of both diagonal and off-diagonal types of decay characteristics is important for the study of absorption and emission properties of the multilevel atom.

Despite the simplicity and versatility of a two-level approximation, some quantum information applications, such as quantum memory, slow light, and quantum computing, can be realized only in multilevel atomic schemes. To describe these processes, one needs to go beyond a two-level approximation. We consider as an example an array of Λ-type three-level atoms trapped along an optical nanofiber; see Fig. 17. We assume that only one ground state $|g\rangle$ is populated. Thus, adding only one additional level to the ground state $|s\rangle$ changes the collective decay rate into the waveguide. Indeed, for two-level atoms trapped near a waveguide with a spacing between atoms $d = \lambda_0/2$, the collective decay rate can be determined as $\Gamma + N\Gamma_{1D}$; see Eq. (28). However, for Λ-type three-level atoms, the collective decay rate reads $\Gamma + N\Gamma_{1D}/2$. Here the factor $1/2$
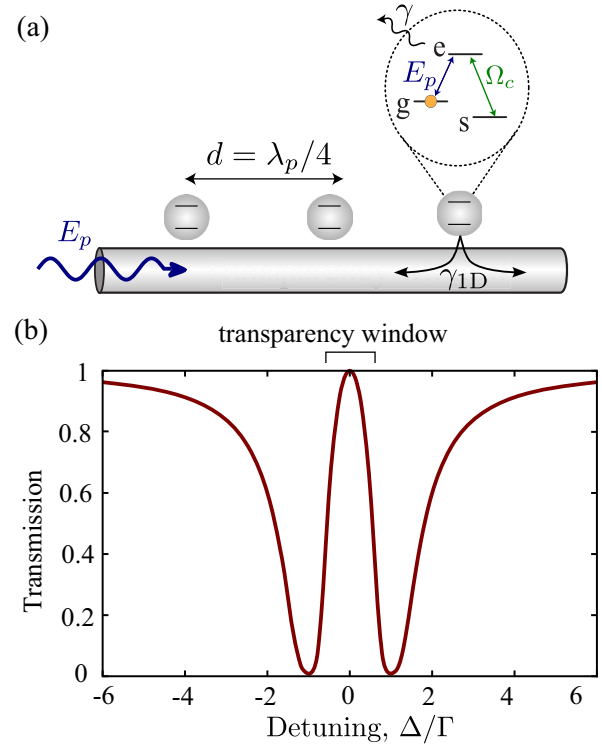

FIG. 17. (a) Schematics of the electromagnetically induced transparency effect. The transition $|g\rangle \rightarrow |e\rangle$ is coupled to the guided photon mode, and the transition $|s\rangle \rightarrow |e\rangle$ is driven by a classical strong control field with a Rabi frequency Ω_c that is external to the nanofiber. (b) Calculated transmission spectrum $|t_N|^2$ with the characteristic transparency window. The number of atoms is $N = 5$, the lattice period is $d = \lambda_p/4$ (where λ_p is the wavelength of the probe photon and the control field $\Omega_c = 2\Gamma$), and the guided decay rate $\gamma_{1D} = 0.5\gamma$. From Asenjo-Garcia, Hood *et al.*, 2017

comes from the presence of two channels of decay in the fiber mode for Λ-configured atoms; see Pivovarov *et al.* (2021).

In the rest of this section, we discuss the propagation of guided light under the condition of electromagnetically induced transparency (EIT), described by Asenjo-Garcia, Hood *et al.* (2017). We assume that the transition $|e\rangle \to |g\rangle$ is coupled to the guided mode and that the orthogonal transition $|e\rangle \to |s\rangle$ is excited externally to the nanofiber, classical, and uniform control field with the Rabi frequency $\Omega_c = 2d_{es}E_c/\hbar$. Here d_{es} is the dipole moment of the transition $|e\rangle \to |s\rangle$ and E_c is the control field amplitude. The applied control field transfers the guided photon from the ground state $|g\rangle$ to a superposition of states $|g\rangle$ and $|s\rangle$ and forms a so-called dark state. The guided photon transfer to the dark state leads to two main consequences that are important in quantum communications. First, it prevents the photon losses due to the long lifetime of the state $|s\rangle$. Second, it results in reduction of the group velocity and the possibility of slowing down the light.

When the control field is present, the interaction part of the atom-photon coupling Hamiltonian (A4) should be modified as follows:

$$H_{\text{atom-phot}} = \sum_{i=1}^{N}\left(\frac{1}{\sqrt{L}}\sum_{k}g_k e^{-ikz_i}a_k^\dagger\sigma_{ge}^{(i)} + \frac{\Omega_c}{2}\sigma_{se}^{(i)} + \text{H.c.}\right).$$
(53)

The energy shift and the dissipation stemming from a coherent interaction between the atoms i and j of the array can be found using the Hamiltonian (15) and correspond to $-\gamma_{1D}\sin(k_{1D}|z_i - z_j|)$ and $\gamma_{1D}\cos(k_{1D}|z_i - z_j|)$, respectively. The transmission coefficient of the atomic array affected by the external control field can be found as

$$t_N = \prod_{\xi}^{N}\frac{\Delta(\Delta + i\gamma) - \Omega_c^2/4}{\Delta(\Delta + i\gamma + \lambda_\xi) - \Omega_c^2/4},$$
(54)

where $\Delta = \omega - \omega_0$ is the detuning of the guided photon frequency ω from the atomic resonance ω_0 and $\lambda_\xi = \Delta_\xi + i\gamma_{1D}^{(\xi)}$, with Δ_ξ and $\gamma_{1D}^{(\xi)}$ corresponding to the energy shift and decay into the waveguide of the eigenstate ξ. Figure 17 shows the transmittance spectrum of the array of $N = 5$ atoms separated by a distance $d = \lambda_p/4$, where λ_p is the wavelength of the guided probe photon. One can see an appearance of the characteristic transparency window around the atomic transition frequency.

Using Eq. (54), one can find an effective wave vector of the polaritonic excitation. Indeed, after the propagation of the light through the array of N atoms, the transmission coefficient acquires the phase factor $t_N \propto e^{ik_{\text{eff}}Nd}$, where k_{eff} is a complex number that characterizes both transmission and absorption. An expansion of Eq. (54) in series over Δ gives

$$k_{\text{eff}} = -\frac{i}{Nd}\sum_{\xi}^{N}\frac{4\lambda_\xi}{\Omega_c^2}\left[\Delta + \frac{4\Delta^2}{\Omega_c^2}(\lambda_\xi + 2i\gamma) + \cdots\right].$$
(55)

Equation (55) is valid for any linear and isotropic quasi-1D structure. Almost all configurations have N eigenstates λ_ξ that

make the calculation of k_{eff} nontrivial. Therefore, for a chain of atoms near a waveguide the effective polaritonic wave vector scales differently with the number of atoms and depends on the interatomic distance. However, as Asenjo-Garcia, Hood *et al.* (2017) showed, the group velocity at the atomic resonance $v_g(\Delta = 0) = (dk_{\text{eff}}/d\Delta)^{-1}|_{\Delta=0} = \Omega_c^2 d/4\gamma_{1D}$ is not affected by a specific atomic configuration. More details on light propagation through an array of atoms with a complex-multilevel structure under the EIT condition and in the presence of undirectional coupling were given by Le Kien and Rauschenbeutel (2015).

Three-level atoms driven by two light beams also enable amplification (Astafiev, Abdumalikov *et al.*, 2010) and cross-Kerr nonlinearity (Hoi *et al.*, 2013); see Vinu and Roy (2020) for the theoretical details.

B. Chiral atomic arrays

Thus far we have considered a situation where an atom is symmetrically coupled to forward- and backward-propagating photons in the waveguide. However, the complex structure of light polarization near a waveguide interface results, under an applied transverse magnetic field, in the chiral (directional) coupling. Namely, the strength of an atom interaction with forward- and backward-propagating photons changes, which provides the grounds for novel nonreciprocal (Scheucher *et al.*, 2016) and cascaded quantum systems (Carmichael, 1993; Stannigel, Rabl, and Zoller, 2012). The systems with broken forward-backward propagation symmetry are now actively studied in the domain of *chiral quantum optics* (Lodahl *et al.*, 2017). We start by discussing the microscopic origins of the spin-momentum locking in the nanophotonic waveguide in Sec. III.B.1. Next we consider directional coupling of a single atom to the waveguide mode in Sec. III.B.2. Section III.B.3 is devoted to the polariton excitations in the array of chirally coupled emitters. To conclude this section, we discuss recent experiments on tunable photon bunching and antibunching in the chiral setup in Sec. III.B.4.

1. Spin-momentum locking

Nanophotonic waveguides provide a unique platform for reaching the directional emission of photons due to the spin-momentum locking effect, thus realizing the one-way inter-actions between the quantum emitters. Spin-momentum locking can be understood by analyzing the coupling of a circularly polarized optical transition to the guided mode of the planar waveguide, as shown in Fig. 18. The main observation is that the polarization of the guided mode is generally elliptical. Indeed, the electric field $\boldsymbol{E}$ outside the waveguide is a transverse plane wave, i.e., $\boldsymbol{k} \cdot \boldsymbol{E} = 0$, where $\boldsymbol{k} = k_x\boldsymbol{e}_x + k_z\boldsymbol{e}_z$ is the wave vector. Since the guided wave is by definition evanescent outside the waveguide, the wave vector component $k_x = \sqrt{(\omega/c)^2 - k_z^2}$ transverse to the waveguide surface is purely imaginary ($k_x = i\kappa$). Thus, the guided wave assumes the form $\boldsymbol{E}(x, z) \sim \exp(-\kappa x)\exp(ik_z z)$. The polarization state of the field is fully defined by the dispersion of the mode $k_z(\omega)$ and varies from linear polarization close to a light line $k_z = \omega/c$ to circular polarization for strongly
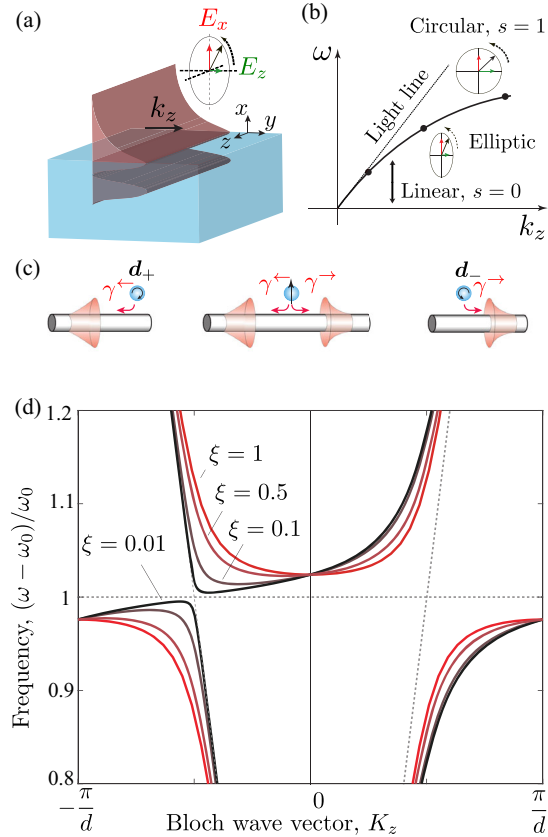
FIG. 18. (a) Evanescent field at a waveguide interface. (b) Schematics of the waveguide mode dispersion with different electric field polarization states. (c) Directional coupling of the emission for right and left circularly polarized atomic dipole transitions. (d) Polariton dispersion in a chiral waveguide depending on the coupling asymmetry ξ. The calculation was performed following Eq. (59) for a regular array of circularly polarized d_- atoms and separated with the phase $\varphi = \omega_0 d / c = \pi/2$.

evanescent waves when $k_z \to \infty$; see Fig. 18(b). We can introduce the polarization parameter $s \in [0, 1]$ such that $E(x, z) = (E_0/\sqrt{s^2 + 1})(e_x - ise_z)e^{ik_z z}$, with $s = 0$ and $s = 1$ corresponding to the linear and circularly polarized fields, respectively. The sign of circular polarization is determined by the sign of the wave vector k_z; it is the opposite for forward- and backward-going waves, $s \propto \text{sgn}k_z$. This spin-momentum locking is a universal feature of guided and surface waves (Sinev *et al.*, 2017). It exists for planar waveguides, nanofibers, and surface plasmon polaritons (Rodriguez-Fortuno *et al.*, 2013; Spitzer *et al.*, 2018); see also the reviews on chiral quantum optics (Lodahl *et al.*, 2017) and spin-momentum locking (Aiello *et al.*, 2015). Intuitively, spin-momentum locking can be understood as a "photonic wheel" effect (Aiello *et al.*, 2015). The wheel rotation (light circular polarization) leads to the translational motion along the surface under the wheel (wave vector k_z), and oppositely rotating wheels travel in opposite directions. More general considerations show that the intrinsic origin of the directional excitation of the guided mode is related to the transverse angular momentum of the photon emitted by the atom (Mitsch *et al.*, 2014; Lamprianidis *et al.*, 2022) rather than its helicity.

2. Directional atom-waveguide coupling

The spin-momentum locking drives asymmetric coupling of transverse circularly polarized emitters with the dipole matrix elements $d_{\mp} = (d_0/\sqrt{2})(e_x \mp ie_z)$ to the waveguide mode. Microscopically, circularly polarized emitters can be realized by applying a magnetic field, which leads to Zeeman splitting of the optical transitions and changes the selection rules. The emitters can be natural atoms (see also Sec. III.A.5) or solid-state emitters, quantum dots (Söllner *et al.*, 2015), or quantum wells (Spitzer *et al.*, 2018). An alternative approach is based on charged quantum dots. There the spin of an extra electron can control the circular polarization of the charged exciton transition (Yılmaz, Fallahi, and Imamoğlu, 2010; Javadi *et al.*, 2018).

In the fully chiral setup ($|s| = 1$), the circularly polarized emitter is coupled only to either forward- or backward-propagating waves. In the case of general elliptic polarization, the couplings can be characterized by emission rates of forward-propagating ($\Gamma^{\rightarrow} \equiv 2\gamma^{\rightarrow}$) and backward-propagating ($\Gamma^{\leftarrow} \equiv 2\gamma^{\leftarrow}$) photons that are proportional to $|E^*(k_z) \cdot d|^2$ and $|E^*(-k_z) \cdot d|^2$, respectively. Explicitly, the emission rates are given by (Gruner and Welsch, 1996; Asenjo-Garcia, Hood *et al.*, 2017)

$$\gamma^{\rightarrow} = \gamma_{1D} \frac{(1 \pm |s|)^2}{s^2 + 1}, \qquad \gamma^{\leftarrow} = \gamma_{1D} \frac{(1 \mp |s|)^2}{s^2 + 1}, \quad (56)$$

where the total decay rate $\gamma_{1D} = \gamma^{\rightarrow} + \gamma^{\leftarrow}$ is found using the Green's function; see Eq. (9). If one takes into account only one circularly polarized mode with $s = 1$ and uses Eq. (7) for the guided part of the Green's function, one can find that the rate $\gamma^{\rightarrow}$ ($\gamma^{\leftarrow}$) is equal to zero for d_- (d_+), which indicates fully chiral one-way coupling. We also introduce the interaction asymmetry parameter $\xi = \gamma^{\leftarrow}/\gamma^{\rightarrow} = (1 \mp |s|)^2/(1 \pm |s|)^2$, which varies from 0 to infinity for the ideal right or left coupling, respectively. From now on, we assume that the Zeeman splitting is large enough that left and right circularly polarized transitions can be spectrally separated. We restrict the consideration to left circularly polarized transitions, and the asymmetry parameter will thus vary from $\xi = 1$ for symmetric coupling to $\xi = 0$ for fully asymmetric (chiral) coupling.

The realistic experimental values of the asymmetry parameter vary depending on the quantum platform. Ramos *et al.* (2014) provided estimations of the asymmetry parameter for Rb atoms near the fiber, obtaining the limits of $10^{-3} < \xi < 1$. Mitsch *et al.* (2014) and Corzo *et al.* (2016) determined the estimated levels of asymmetry extracted from the experimental spectra to be $\xi = 0.083$ and 0.087, respectively. Alternatively, the asymmetry of Rydberg atom spin states coupling with a phonon mode was estimated as $\xi \sim 1/400$ by Vermersch *et al.* (2016). The recently proposed experimental concept of directional coupling in superconducting circuits (Guimond *et al.*, 2020) provided a directional β factor of more than 99%, which corresponds to a ξ parameter of at least $\sim 1/100$.

Consider the scattering of guided photons on the asymmetrically coupled atom. The scattering is characterized by the amplitude reflection coefficient r and forward and backward

amplitude transmission coefficients $t_{\rightarrow,\leftarrow}$ given by (Lodahl *et al.*, 2017)

$$r = \frac{2i\sqrt{\gamma^{\rightarrow}\gamma^{\leftarrow}}}{\omega_0 - \omega - i(\gamma + \gamma_{1D})},$$

$$t_{\rightarrow/\leftarrow} = 1 + \frac{2i\gamma^{\rightarrow/\leftarrow}}{\omega_0 - \omega - i(\gamma + \gamma_{1D})}, \qquad (57)$$

where the constant γ describes all other decay channels. The absolute values of the transmission coefficients $t_{\rightarrow}$ and $t_{\leftarrow}$ are the same, and for vanishing losses $\gamma = 0$ we obtain the energy conservation law $|r|^2 + |t_{\rightarrow/\leftarrow}|^2 = 1$. In the symmetric case, when $\gamma^{\rightarrow} = \gamma^{\leftarrow} = \gamma_{1D}/2$ the reflection and transmission coefficients in Eq. (57) reduce to Eqs. (28) with $N = 1$. In the fully chiral setup $\gamma^{\leftarrow} = 0$ and for vanishing losses $\gamma = 0$, the reflection coefficient vanishes and the transmission coefficient is equal to 1 by the absolute value. At the resonance, we obtain $t_{\rightarrow} = -1$, so light obtains a π phase shift when resonantly passing an atom.

There are other possibilities to realize directional atom-waveguide interactions that do not rely on spin-momentum locking. Instead, one could use nonlinearity that breaks time-reversal symmetry and leads to nonreciprocal photon transmission (Roy, 2010, Roy, 2013a, 2017; Shi, Yu, and Fan, 2015). To this end, the nonlinear structure also needs to lack the $z \rightarrow -z$ mirror symmetry. The quantum nonreciprocity for two superconducting qubits coupled to a waveguide was recently demonstrated by Rosario Hamann *et al.* (2018). While at lower power the structure has behaved reciprocally, an increase in power has led to nonreciprocal transmission driven by quantum nonlinearity. At even larger power, the reciprocity has been restored due to the saturation of the qubit transitions. Moreover, there are structures that, while reciprocal in the single-photon regime and not directly belonging to the traditional domain of chiral quantum optics, also rely on unidirectional atom-photon interactions. Specifically, one can have $|t_{\leftarrow}|^2 = |t_{\rightarrow}|^2 = 1$ and $r = 0$ such that the atom scatters only in the forward direction. This system was considered by Gheeraert, Kono, and Nakamura (2020) and Guimond *et al.* (2020), where each effective atom was formed by two identical waveguide-coupled qubits spaced by a quarter of the wavelength. Because of this $\lambda/4$ spacing, the photons reflected from the first and second qubits interfere destructively and the backscattering is suppressed. The array of these qubit dimers illustrated in Fig. 19(a) was proposed by Guimond *et al.* (2020) for the generation of complex quantum states such as the Greenberger-Horne-Zeilinger (GHZ) state and the 1D cluster state. The structures under consideration consist of the qubit dimers (dark yellow rectangles) coupled to two waveguides (shown in blue). Each dimer also interacts with an additional stationary qubit (shown in green). When the stationary qubit is in its ground state, the dimer transmits a photon with a π-phase shift, and when the stationary qubit is excited the phase shift is equal to zero. Judiciously linking the waveguides with beam splitters and using photons in the waveguides as "flying qubits," one can then realize complex quantum states in the stationary qubit array.

For example, the proposed protocol to generate the GHZ state shown in Fig. 19(a) starts by initialization of the stationary qubits in the product state $|+\rangle_1 \otimes |+\rangle_2 \dots$, where $|+\rangle_n$ is the Hadamard state, $|\pm\rangle \equiv (|1\rangle \pm |0\rangle)/\sqrt{2}$, and sending one photon in the lower waveguide. As described in more detail in Appendix H, upon the conditional detection of the transmitted photon in one of the waveguides, the stationary qubit array ends in one of the GHZ states: $|+\rangle_1 \otimes |+\rangle_2 \dots \pm |-\rangle_1 \otimes |-\rangle_2 \dots$. The slightly more complicated protocol with three beam splitters shown in Fig. 19(b) enables an arbitrary quantum state $|\psi_q\rangle$ of qubit 1 to be transferred to qubit 2. In this case, photon scattering realizes an effective controlled-Z gate between the distant qubits, thereby enabling universal quantum computation. A larger array with more dimers, separated by the beam splitters, allows one to generate a one-dimensional photon cluster state.

A concept based on unidirectional scattering can be implemented even in free space without any waveguide. Namely, it was proposed by Grankin *et al.* (2018) to couple an atom to an auxiliary two-dimensional bilayer atomic array that acts as a "quantum antenna" providing unidirectional photon emission. A related experimental demonstration was made by Stiesdal *et al.* (2021) for three clouds of Rydberg ^{87}Rb atoms. Each cloud has preferentially scattered photons in the forward direction, thereby realizing cascaded coupling.

3. Arrays of chirally coupled emitters

Waveguide-mediated chiral coupling between emitters can be considered using an effective non-Hermitian Hamiltonian (6) with a traced out electromagnetic field. Combining Eqs. (7) and (56), we obtain

$$V_{mn} = -i\gamma_{1D}\delta_{mn} + \begin{cases} -i\gamma^{\rightarrow}e^{i\omega(z_m - z_n)/c} & \text{for } z_m > z_n, \\ -i\gamma^{\leftarrow}e^{i\omega(z_n - z_m)/c} & \text{for } z_m < z_n, \end{cases} \qquad (58)$$

where z_m and z_n are emitter coordinates along the waveguide. Using this Hamiltonian, one can obtain the dispersion of polaritonic Bloch waves $\psi_m \propto e^{iK_z m}$ in a periodic array of atoms with a spacing d (Calajó and Chang, 2022; Fedorovich *et al.*, 2022):

$$\omega - \omega_0 = \frac{\gamma_{1D}}{1 + \xi}\left[\cot\left(\frac{K_z d - \varphi}{2}\right) + \xi \cot\left(\frac{K_z d + \varphi}{2}\right)\right], \qquad (59)$$

where $\varphi = \omega/c$. The two terms in the square brackets of Eq. (59) describe the avoided crossing of forward- and backward-propagating photon dispersion with the atomic resonance. For a purely symmetric coupling $\xi = 1$, the dispersion relation transforms into Eq. (12). The dependence of dispersion on the asymmetry parameter ξ is plotted in Fig. 18, and it demonstrates a strongly unidirectional character of polariton propagation for $\xi \rightarrow 0$, that is, $\omega(K_z) \neq \omega(-K_z)$.

The effects of chiral coupling can also be observed in the spectrum of eigenmodes of the finite atomic array. Figure 20 compares polariton energy spectra calculated by numerically diagonalizing the Hamiltonian (58) for the fully chirally coupled arrays of $N = 400$ atoms given by Fedorovich *et al.* (2022). As discussed in Sec. III.A.2, the eigenstates are simply standing waves with frequencies satisfying the dispersion law for the infinite structure in Eq. (59). Hence, the calculated
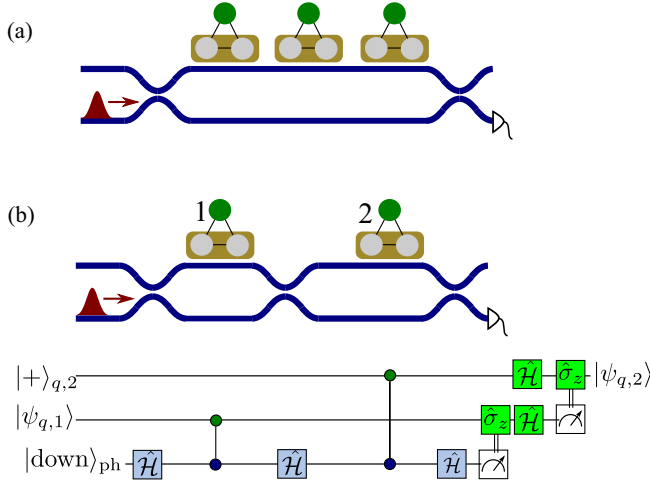
(a)

(b)

FIG. 19. Illustration of the protocol proposed by Guimond *et al.* (2020) for generation of (a) a GHZ state and (b) a quantum state transfer with an array of superconducting qubits coupled to two waveguides. The bottom panel in (b), which shows the quantum circuit, is described in Appendix H.
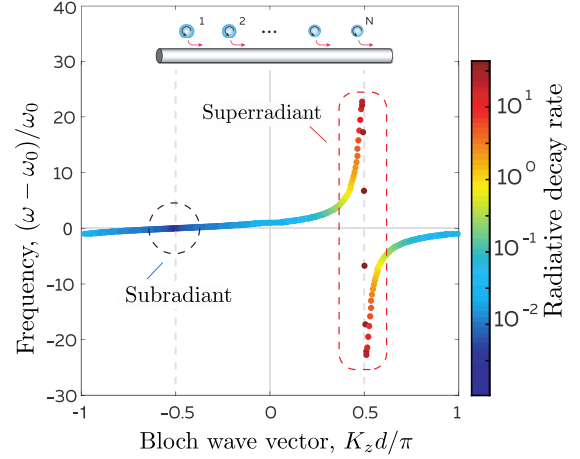

FIG. 20. The frequencies and radiative rates of polariton eigenstates of a finite chain of regularly spaced atoms chirally coupled through a waveguide mode with $\xi = 2 \times 10^{-5}$, depending on the corresponding Bloch wave vector. The radiative decay rate, indicated by the color of the dots, is normalized to the decay rate of the individual atom γ_{1D}. The calculation was performed for $N = 400$ atoms and the anti-Bragg spacing $\varphi = \omega_0 d/c = \pi/2$. From Fedorovich *et al.*, 2022.

eigenfrequencies for the finite structure lie on the dispersion curve for the infinite structure, which is strongly asymmetric in the chiral case. As in the symmetric case of Fig. 6, the radiative decay rate is at maximum for the eigenstates with the wave vector K_z closest to the wave vector of light $\pm\omega_0/c$, and when the polariton wave vector is strongly detuned from the light wave vector, the polariton states become subradiant. See Jones *et al.* (2020) for a detailed theoretical analysis of superradiant chiral emission from atomic arrays into the nanofiber. Jones *et al.* predicted that near-perfect chirality can already be achieved for arrays containing 10–15 atoms by phase matching a superradiant collective guided emission mode via an external laser field.

4. Photon bunching and antibunching in a chiral waveguide

Here we examine the correlations between photons in a waveguide chirally coupled to an array of closely spaced atoms. We consider a fully chiral setup $\xi = \gamma^\leftarrow = 0$. In this case, the photons are transmitted by atoms one by one. The reflection is absent and the transmission coefficient through N atoms is simply a product of the transmission coefficients of individual atoms:

$$t_N = t_1^N, \qquad t_1 = 1 + \frac{2i\gamma^\rightarrow}{\omega_0 - \varepsilon - i(\gamma + \gamma^\rightarrow)}. \qquad (60)$$

In Eq. (60) the radiative decay rate $\gamma^\rightarrow$ is linked to the matrix element of the atom coupling to the right-going photon mode g as $\gamma^\rightarrow = g^2/2c$.

The photon-photon correlation function for a single resonantly excited two-level atom chirally coupled to the waveguide is given by

$$g_1^{(2)}(0) = \frac{(\gamma + \gamma^\rightarrow)^2 (\gamma - 3\gamma^\rightarrow)^2}{(\gamma - \gamma^\rightarrow)^4}. \qquad (61)$$

Equation (61) can be obtained by standard input-output techniques of quantum optics (Kojima *et al.*, 2003; Koshino and Ishihara, 2004). The problem is similar to photon reflection from a one-sided cavity (Rice and Carmichael, 1988).

Equation (61) demonstrates that the photon-photon correlations are sensitive to the ratio of the decay rates γ and $\gamma^\rightarrow$ and that it is possible to realize both bunching and antibunching. Specifically, for $\gamma = 0$ one has $g_1^{(2)}(0) = 9$. Increasing the value of γ leads to an even stronger bunching. The value of $\gamma = \gamma^\rightarrow$ when the single-photon transmission is suppressed ($t_1 = 0$) corresponds to a perfect bunching, $g_1^{(2)}(0) = \infty$. A further increase of γ leads to perfect antibunching at $\gamma = 3\gamma^\rightarrow$. However, in practice the coupling of a single natural atom to a waveguide is weak: $\gamma^\rightarrow/\gamma \sim 1\%$. This means that photons transmitted through one atom are almost uncorrelated. The correlations can be enhanced either by putting an atom in cavity (Dayan *et al.*, 2008; Aoki *et al.*, 2009; Scheucher *et al.*, 2016) or by increasing the number of atoms N (Prasad *et al.*, 2020). For artificial atoms such as superconducting qubits or quantum dots, the coupling can be much stronger; see Fig. 2.

Before proceeding to the results of the experiment (Prasad *et al.*, 2020), we first discuss the theoretical problem of photon pair scattering in the chiral setup. The most interesting effects occur when the number of atoms reaches $N \sim \gamma/\gamma^\rightarrow \sim 100$, but the calculations are significantly more involved than those used for the nonchiral Dicke problem (Rupasov and Yudson, 1984), which is discussed in Sec. III.A.3, even when the interatomic spacing is zero. The reason for this is that the atoms in the nonchiral problem are equivalent to each other, while in the chiral case they are ordered from left to right and hence are not equivalent. However, the problem can be still solved exactly by means of the Bethe *Ansatz* (Ringel, Pletyukhov, and Gritsev, 2014; Mahmoodian *et al.*, 2018).

An important milestone in theoretical research was achieved by Mahmoodian *et al.* (2020), who considered the Dicke problem for a chiral waveguide with multiple photons and multiple atoms. It was demonstrated that the pulse transmission through the atomic array can be satisfactorily described by taking into account only relatively simple bound eigenstates states of the Bethe *Ansatz* (Rupasov and Yudson, 1984; Yudson, 1985), and the connection to solitons in the classical optics regime with large photon numbers has been made. More recently Calajó and Chang (2022) numerically analyzed the transition from the quantum to the classical nonlinear optics regime for both nonchiral and chiral structures. In Appendix I, we present an alternative equivalent derivation using the Green's function technique employed by Zheng and Baranger (2013), Fang, Zheng, and Baranger (2014), and Poshakinskiy and Poddubny (2016). In the case in which $\gamma \gg \gamma^{\rightarrow}$, the photon-photon correlation function is well described by the approximate equation

$$g_N^{(2)}(0) \approx \left[1 - \frac{\sqrt{2}\gamma^{\rightarrow}}{2\gamma} \exp\left(\frac{4N\gamma^{\rightarrow}}{\gamma}\right) \right]^2, \qquad (62)$$

and its dependence on the number of atoms N and on the decay rate γ is shown in Fig. 21. This result is more notable than that of the nonchiral situation; compare Figs. 21 and 13. Specifically, the dependence of the correlation function on the number of atoms is nonmonotonic: increase of N leads first to the antibunching and then to the bunching. The bunching threshold corresponds to $N^* \sim \gamma/\gamma^{\rightarrow}$ or, more precisely, one has $g_{N*}^{(2)}(0) = 1$ at

$$N^*(\gamma) \approx \frac{\gamma}{8\gamma^{\rightarrow}} \left(3\ln 2 + 2\ln \frac{\gamma}{\gamma^{\rightarrow}} \right) \qquad (63)$$

(black curve in Fig. 21). Qualitatively, the nonmonotonic behavior of the correlation function is caused by the interference of two contributions to the photon pair transmission coefficient [the first and second terms in Eq. (62)]. The two terms corresponding to an independent transmission of two photons and the transmission of the correlated photon pair are of opposite signs. The correlated contribution becomes dominant at larger N, when the single-photon transmission is suppressed, leading to photon bunching. The transition from independent photon propagation to antibunching to bunching with an increase in the atom number was first observed by Prasad *et al.* (2020). The experimental dependence $g_N^{(2)}(0)$ on N given by Prasad *et al.* (2020) is presented in Fig. 22. The measured value of the correlation function has been tuned from $g^{(2)}(0) \approx 0.37 \pm 0.12$ for $N \approx 160$ atoms to $g^{(2)}(0) \approx 24 \pm 7$ for $N \approx 200$ atoms. In the experiment, the antibunching was not perfect, due to the fluctuations of the optical density resulting from the uncertainty in the preparation of an atomic ensemble and from the photon shot noise. This can be seen by comparing the green and orange curves in Fig. 22. While the dash-dotted green curve had been calculated by Prasad *et al.* (2020) for an idealized situation and corresponds to Eq. (62), the solid orange curve takes the uncertainties into account and describes the experiment quantitatively.

The correlated photon transport has been also studied for arrays of three-level atoms coupled to a symmetric (Roy, 2011; Roy and Bondyopadhaya, 2014; Song *et al.*, 2017) and a chiral waveguide (Iversen and Pohl, 2021). For the chiral waveguide, it has been predicted that in conditions of EIT of the three-level medium, a high degree of antibunching and photon transmission can be maintained in the presence of moderate losses (Iversen and Pohl, 2021). While in this section we focus on a fully chiral setup, the behavior of quantum photon-photon correlations in the case of general asymmetric coupling is a long-standing problem, despite some recent progress in the field (Jen, 2021).
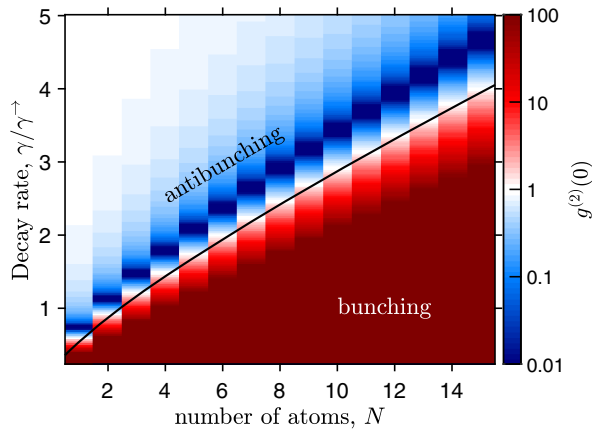

FIG. 21. Dependence of the photon-photon correlation function $g^{(2)}(0)$ in a chiral waveguide on the number of atoms N and on the ratio of nonradiative and radiative damping rates $\gamma/\gamma^{\rightarrow}$. The black curve shows the threshold value $N^*(\gamma)$ given by Eq. (63) when $g_{N*}^{(2)}(0) = 1$. The calculation was performed using Eq. (I7) for light incident at the resonant frequency $\varepsilon = \omega_0$ at the two-level atoms ($U \to \infty$).
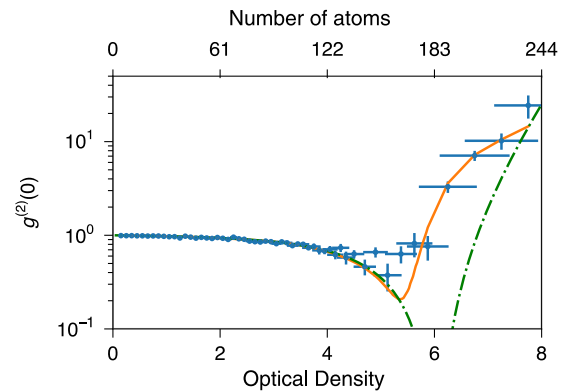

FIG. 22. Experimentally measured (crosses) and calculated (lines) photon-photon correlation functions depending on the number of atoms in the array and optical density. Solid orange and dash-dotted green curves were calculated without and with the experimental uncertainty in the optical density. The parameters of the experiment correspond to $\gamma/\gamma^{\rightarrow} \approx 130$. From Prasad *et al.*, 2020.

C. Two-dimensional atomic arrays

As mentioned in Sec. II, an ordered two-dimensional atomic array with a small lattice period scatters incident light in the far field only in a certain direction, determined by the in-plane light wave vector, because diffraction is not possible. Thus, the problem involving photon interaction with the array is quasi-one-dimensional and similar to a typical WQED problem, with the entire array playing the role of an effective atom (Rui *et al.*, 2020). In this section, we discuss light reflection from such an effective atom in more detail.

Reflection of light from the planar array of scatterers is a well-known problem in classical optics (de Vries, van Coevorden, and Lagendijk, 1998; Khitrova and Gibbs, 2007; Gippius and Tikhodeev, 2009). More recently it has been extensively studied in the field of metasurfaces, artificial two-dimensional arrays of resonant scatterers with a spacing smaller than the light wavelength. These scatterers can be metallic nanoparticles with plasmonic resonances (Decker *et al.*, 2011); dielectric and semiconductor particles, such as those made of silicon, that have Mie optical resonances (Kuznetsov *et al.*, 2016; Kivshar, 2018). The two-dimensional atomic arrays could be viewed as quantum metasurfaces with strong optical nonlinearities at the single-quantum level (Bekenstein *et al.*, 2020; Bettles *et al.*, 2020; Moreno-Cardoner, Goncalves, and Chang, 2021; Solomons and Shahmoon, 2021; Zhang *et al.*, 2022).

Reflection and transmission coefficients for a single photon, normally incident upon the array, can be presented in the form

$$r = \frac{i\gamma_{2D}}{\tilde{\omega}_0 - \omega - i(\gamma + \gamma_{2D})}, \qquad t = \frac{\tilde{\omega}_0 - \omega - i\gamma}{\tilde{\omega}_0 - \omega - i(\gamma + \gamma_{2D})}, \tag{64}$$

which is reminiscent of the reflection and transmission coefficients in Eq. (28) of one atom coupled to a waveguide. In Eq. (64) γ_{2D} is the collective radiative decay rate of the atomic array and $\tilde{\omega}_0$ is the resonance frequency modified by the collective coupling with light (which can be viewed as the cooperative Lamb shift) given by

$$\tilde{\omega}_0 = \omega_0 - \frac{3\gamma_0 \lambda_0^3}{16\pi^3} \mathrm{Re}C, \qquad \gamma_{2D} = \gamma_0 + \frac{3\gamma_0 \lambda_0^3}{16\pi^3} \mathrm{Im}C, \tag{65}$$

where $\gamma_0 = 2\Gamma_0$ is the spontaneous decay rate of a single atom in free space and C is the so-called interaction constant (Simovski, Belov, and Kondratjev, 1999; Belov and Simovski, 2005). The explicit expression for C and the derivation details are presented in Appendix J; see, in particular, Eq. (J5). In the limit in which the spacing between the atoms is much smaller than the light wavelength, one can show that

$$C \approx \frac{2\pi i\omega}{ca^2} + \frac{S + (\omega/c)^2 S'}{2}, \tag{66}$$

where $S \approx 9.03/a^3$ and $S' \approx -3.90/a$. Substituting Eq. (66) into Eq. (65), we find that (Ivchenko and Kavokin, 1992; Ivchenko *et al.*, 1992)

$$\gamma_{2D} = \gamma_0 \frac{3\lambda^2}{4\pi a^2}. \tag{67}$$

Hence, as in the classical Dicke formula for the dense three-dimensional cloud, where the collective decay rate scales as $\gamma_{3D} \sim \gamma_0 (\lambda/a)^3$, the decay rate of the two-dimensional array exhibits cooperative enhancement with the factor of the order of the number of atoms per wavelength square. Figure 23(a) shows the dependence of the collective radiative decay rate γ_{2D} on the ratio of the array period to the light wavelength a/λ_0. For a short period, the array exhibits a superradiant behavior $(\gamma_{2D} > \gamma_0)$, but the radiative linewidth quickly decays with the growth of lattice spacing, and for $a/\lambda_0 > \sqrt{3/4\pi} \approx 0.5$ the structure becomes a subradiant one $(\gamma_{2D} < \gamma_0)$. This enhancement has been observed experimentally for quantum wire arrays (Ivchenko *et al.*, 1992) and quantum dot arrays (Khitrova and Gibbs, 2007), but detailed studies of collective light-matter coupling have been prevented by the strong inhomogeneous broadening. Much more experimental progress has been made for metamaterials, and recently for optical lattices (Rui *et al.*, 2020).

Figure 23(b) presents the reflection spectrum depending on the array period [we have recalculated it following Shahmoon *et al.* (2017)]. While the linewidth of the reflection resonance decreases monotonically for larger spacing following Fig. 23(a), the behavior of the resonance frequency $\tilde{\omega}_0$ is more subtle and nonmonotonic, as shown by the thick black line in Fig. 23(b). For small spacings, the cooperative Lamb shift diverges for $a \to 0$ as $\tilde{\omega}_0 - \omega_0 \propto -\gamma_{1D}(\lambda_0/a)^3$, as follows from Eq. (66), the thin red line in Fig. 23(b). Qualitatively, the Lamb shift is determined by the near-field
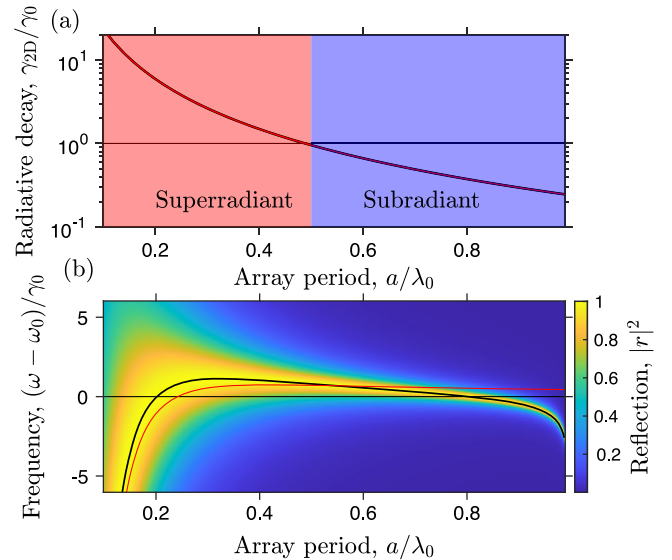

FIG. 23. (a) Collective radiative decay rate of an atomic array depending on the ratio of the array period a to the light wavelength at the atomic resonance λ_0. (b) Light reflection spectra depending on the ratio a/λ_0. The thick black line shows the collective resonance frequency $\tilde{\omega}_0$ [Eq. (65)] and the thin red line shows the analytical solution found using Eq. (66), calculated while neglecting the nonradiative decay rate Γ for the state with the zero in-plane wave vector.

dipole-dipole interactions between atoms. However, the value of the Lamb shift crosses zero for $a \approx 0.2\lambda_0$ due to the destructive interference of the two terms S and $S'(\omega/c)^2$ in Eq. (66). This point corresponds to the perfect reflection when $|r(\omega_0)| = 1$. Another special point at which the Lamb shift vanishes and $|r(\omega_0)| = 1$ is $a \approx 0.8\lambda_0$ (Bettles, Gardiner, and Adams, 2016; Shahmoon *et al.*, 2017).

We now discuss in more detail a recent theoretical proposal of atom-made metasurfaces for the generation of highly entangled photon states (Bekenstein *et al.*, 2020); see Srakaew *et al.* (2023) for experimental verification. The generation and manipulation of Schrödinger cat states were recently demonstrated experimentally in Rydberg atom arrays (Omran *et al.*, 2019) and superconducting qubit arrays (C. Song *et al.*, 2019). Atom-made metasurfaces present a natural further step in this direction. The proposal of Bekenstein *et al.* (2020) was based on the placement of a single ancillary atom near the metasurface. Next, by changing the quantum state of the ancillary atom, one can control via the Rydberg interactions whether the photons will be fully reflected or fully transmitted by the metasurface. This is because even a single atomic layer with subwavelength spacing can realize perfect reflection, thus enhancing the coupling of the ancillary atom with the photons. Specifically, it is proposed to coherently drive a 2D array of three-level atoms in the EIT regime (Fleischhauer, Imamoglu, and Marangos, 2005). The EIT condition is also modified by the Rydberg interactions. If the ancillary atom is in the ground state $|g'\rangle$, the metasurface is in the $|U\rangle$ state, uncoupled from the incident light. When the atom is in its Rydberg state $|r'\rangle$, the metasurface is detuned from the EIT condition to the state $|C\rangle$ and fully reflects light. One starts by preparing the ancillary atom in the state $\psi = (1/\sqrt{2})(|g'\rangle + |r'\rangle)$ so that the full system of atom and metasurface is in the state $(1/\sqrt{2})(|g'\rangle|U\rangle + |r'\rangle|C\rangle)$. Next one sends N initially unentangled photons to different points in the array plane and performs the projective measurement of the ancillary atom in the basis $(1/\sqrt{2})(|g'\rangle \pm |r'\rangle)$. As a result, the scattered light is in the GHZ photonic state $(1/\sqrt{2})(|0\rangle^{\otimes N} + |1\rangle^{\otimes N})$, where the states $|0\rangle$ and $|1\rangle$ correspond to transmitted and reflected photons. Such quantum scattering corresponds to a controlled-NOT gate for photons that processes photons in parallel due to the planar array geometry. The process efficiency is limited by the finite range of the Rydberg interactions controlling the EIT condition. The GHZ state fidelity also depends on the number of atoms. According to the calculation, a fidelity of over 90% requires arrays with more than 20×20 atoms. This protocol can be further developed to realize more complex quantum states (Bekenstein *et al.*, 2020). For example, changing the ancillary atom state between the photon scattering processes should lead to the generation of photon cluster states. Highly entangled free-space photon states could be realized by coupling several ancillary atoms to the metasurface.

IV. EXPERIMENTAL DEMONSTRATIONS

We now discuss experimental demonstrations, highlighting potential applications of the waveguide quantum electrodynamics platform. Since this field is rapidly evolving, covering all relevant works does not seem feasible. Instead, we consider in detail several experiments representing major research directions. We start in Sec. IV.A by discussing superradiance in the waveguide-coupled atomic arrays measured by Solano *et al.* (2017) and proceed to the generation of collective atomic excitations and quantum light in this setup (Sec. IV.B), focusing on the experiment by Corzo *et al.* (2019). Next we consider the slow-light effect under the conditions of electromagnetically induced transparency reported by Gouraud *et al.* (2015) and Sayrin *et al.* (2015) and the potential applications for quantum memory discussed in Sec. IV.C. Section IV.D is devoted to the demonstration of the subradiant modes in the transmon qubit array reported by Brehm *et al.* (2021). Section IV.E presents experimental results (Corzo *et al.*, 2016) for the Bragg-spaced atomic arrays with both unidirectional and chiral interactions.

An important comment should be made regarding disorder in the atomic Bragg arrays, which is inevitably present at the current level of experimental technologies. The achievable filling factor is $\sim 0.5 - 0.8$ with random occupation of the lattice sites by the atoms (Goban *et al.*, 2012; Corzo *et al.*, 2016; Prasad *et al.*, 2020). At the same time, the disorder in the atomic system may harm quantum states such as subradiant states, leading to nonhomogeneous broadening, as shown in Fig. 4 for 2D atomic array systems. In 1D systems, the effects of disorder have been extensively studied theoretically in the case of achiral (Haakh, Faez, and Sandoghdar, 2016; Kornovan *et al.*, 2019) and chiral (Mirza, Hoskins, and Schotland, 2017; Mirza and Schotland, 2018; Jen, 2020; Fedorovich *et al.*, 2022) interactions. Alternatively, the influence of disorder on spectral properties of semiconductor polaritonic lattices has been also been previously studied (Malpuech and Kavokin, 1999; Kosobukin, 2003; Kosobukin and Poddubny, 2007).

A. Superradiance and subradiance in waveguide-coupled atomic arrays

While collective superradiant coupling can be observed for atoms in free space (DeVoe and Brewer, 1996; Guerin, Araújo, and Kaiser, 2016), waveguides offer new opportunities to control the interactions between atoms. It is potentially possible to place atoms far enough apart so that the dipole-dipole interaction becomes irrelevant and to realize collective superradiant or subradiant states mediated by long-range waveguide-mediated coupling (Gonzalez-Tudela *et al.*, 2011; Shahmoon and Kurizki, 2013). An important milestone was reported by Goban *et al.* (2014, 2015) for cesium atoms near an alligator photonic crystal waveguide; see Sec. II for more details on this structure. The total spontaneous emission rate was found to scale linearly with the number of trapped atoms. However, the number of atoms was relatively small ($N \sim 1 - 3$, and their distance along the waveguide was on the order of $10\ \mu m$ and not controllable. Thus, observing the controllable superradiant coupling between distant clouds of atoms, separated by about 0.3 mm along the waveguide, was an important step (Solano *et al.*, 2017). The main experimental results of this work are reproduced in Fig. 24. Instead of the alligator photonic crystal utilized by Goban *et al.* (2014, 2015), Solano *et al.* used an optical nanofiber overlap

magneto-optical trap that contained ^{87}Rb atoms. Figure 24(a) shows an example of measured spontaneous emission kinetics for an atomic cloud after the initial excitation probe has been turned off. The average number of atoms for this realization was $N = 6$, with the optical density ≈ 0.7. The initial faster component of the signal has been fitted as an exponential decay (red dashed line). The dependence of this decay constant on the array geometry, which is presented in Fig. 24(b), depends on the number of atoms in the system. All the measured decay rates scale linearly with the number of atoms, which is a manifestation of the superradiant collective behavior. The blue circles in Fig. 24(b) correspond to a single
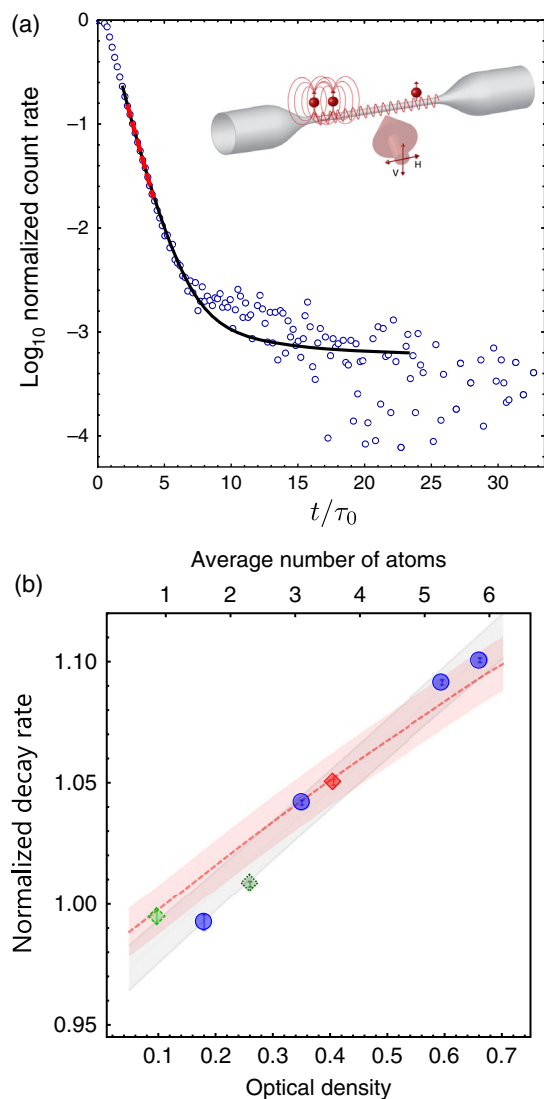

FIG. 24. (a) Experimental spontaneous emission kinetics of photons in a nanofiber. Time is normalized to the natural atom lifetime ($\tau_0 = 1/\Gamma_0 = 26.24$ ns). Inset: illustrated setup and waveguide-mediated coupling between distant atoms. (b) Dependence of the spontaneous decay rate on the average number of atoms and the corresponding OD for two distant atomic clouds. The blue circles, dotted dark green diamonds, and solid red square correspond to the right atomic cloud, left atomic cloud, and a combination of the two clouds, respectively. The red dashed line is the theoretical prediction. From Solano *et al.* (2017).

atomic cloud, and the solid red square corresponds to atoms split into two clouds separated by about 400 wavelengths. This measurement satisfies the same linear scaling law and provides an unambiguous proof of long-range waveguide-mediated interactions for distant clouds. We note, however, that the overall modification of the radiative decay rate compared to that of a single atom in vacuum is not large, on the order of 10%. This modification has been limited by the coupling efficiency of atomic emission into the waveguide mode, which has been estimated as $\beta \approx 13\%$. Figure 24(a) also reveals a more slowly decaying tail attributed to subradiant modes of the cloud.

We have focused here only on single-photon superradiance that is resolved in the weak excitation regime. There is also the opposite regime, considered in the original Dicke proposal, in which all atoms of the array are initially in the excited state and then rapidly emit light. We refer the interested reader to the recent theoretical work of Masson *et al.* (2020) studying many-body signatures of collective decay in atomic arrays, and references therein for more details on this regime. The phenomenon of superradiance can also be studied theoretically in more complicated setups. For example, Wang *et al.* (2020) theoretically considered quantum emitters coupled to a waveguide formed by an array of coupled cavities. Wang *et al.* (2015) formulated an interesting proposal of superradiant lattices in reciprocal momentum space that was realized for an array of three-level atoms coupled to an external wave. This concept might be useful as a simulator of solid-state physics in a quantum optical setup.

B. Generation of collective excitations of an atomic array

The generation of collective quantum states of atoms coupled to light presents one of the main potential applications of the WQED platform. In Sec. III.B.4 we described how arrays of atoms weakly chirally coupled to the waveguide have been used to experimentally demonstrate either photon bunching or antibunching, depending on the photon number (Prasad *et al.*, 2020). There have also been preliminary reports on the two-photon entanglement and squeezing from the same setup (Hinney *et al.*, 2021). Schrödinger cat states were recently realized in an array of atoms coupled to an optical waveguide (Leong *et al.*, 2020).

We now discuss in more detail another important experimental demonstration (Corzo *et al.*, 2019). A collective atomic excitation in an atomic array has been prepared and then read out with an external laser pulse leading to single-photon emission into the guided mode using the Duan-Lukin-Cirac-Zoller (DLCZ) protocol (Duan *et al.*, 2001). To implement this protocol, 2000 atoms of ^{133}Cs were initially prepared in the ground state $|g\rangle = |6S_{1/2}, F = 4\rangle$ and trapped along the optical nanofiber; see the top panel of Fig. 25. Specifically, a weak pulse in y polarization and detuned by $\Delta = -10$ MHz from the $|g\rangle \rightarrow |e\rangle$ atomic transition creates a single collective excitation in an array. This excitation was heralded by detecting a single-photon guided mode of the nanofiber, quasilinearly polarized along the x axis (the field-1 mode). After a programmable delay, an external read pulse resonant with the $|s\rangle \rightarrow |e\rangle$ atomic transition was sent to the ensemble. The read pulse maps the collective excitation into a field-2

photon that escapes the atomic ensemble and propagates in the opposite direction of field-1 photon. The field-2 mode is also a guided one, but it has a quasilinear polarization along the y axis. The readout process benefits from the enhanced atom interaction with the guided mode. Namely, the single-atom coupling has been around $\beta = \Gamma_{1D}/\Gamma \approx 10^{-2}$, where Γ_{1D} and Γ are the radiative decay rates into the guided mode and into free space. As described in Sec. II.A, this has allowed OD equal to 300 for 2000 atoms to be achieved, which means that the atom-waveguide interaction is enhanced by about 2 orders of magnitude compared to the effective free-space interaction. The one-dimensional geometry of the problem presents another advantage over the 3D free-space setup. Namely, since the initial pulse is incident from the side of the array and is external to the nanofiber, it is possible to collectively excite the atoms with the same amplitude.

After the implementation of the DLCZ protocol, the non-classical correlations between field 1 and field 2 should be characterized. This can be done with the normalized cross-correlation function $g_{12} = p_{12}/p_1 p_2$, where p_{12} is the joint probability of detecting a pair of photons and p_1 and p_2 are the probabilities of detecting a photon in fields 1 and 2. The dependence of g_{12} on the probability p_1 is shown in Fig. 25(a). One can see that the value of g_{12} increases when the excitation probability is reduced. For efficient retrieval of the stored collective excitation, the conditional retrieval efficiency is a crucial parameter. It can be found via a measurement of the conditional probability of detecting a guided photon in field 2 after retrieval ($p_c = p_{12}/p_1$). Memory efficiency can be found as a ratio $q_c = p_c/\eta_2$, with η_2 the overall detection efficiency. Figure 25(b) displays the retrieval efficiency as a function of p_1. One can observe three different regimes. In the first region, characterized by the large value of p_1, q_c increases with p_1 and corresponds to a multiexcitation process in the write field. The second region with a plateau in the q_c corresponds to a single-excitation regime. And the third region corresponds to low excitation probability, where the noise background causes false heralding events to become predominant.

Finally, a single-photon character of the heralded excitation can be confirmed by measuring the degree of suppression w of the two-photon component of the retrieved field 2 compared to a coherent state. This value can be found from the ratio $W = p_1 p_{1,2a,2b}/p_{1,2a}p_{1,2b}$, where $p_{1,2a,2b}$ indicates the probability for triple coincidences and $p_{1,2a}$ and $p_{1,2b}$ are probabilities for coincidences between detectors. In Fig. 25(c), one can see the antibunching value w as a function of the cross-correlated parameter g_{12}. The temporal mode of the guided single photon is given in the inset of Fig. 25(c). These experimental achievements demonstrate that the collective quantum state can be characterized by the subsequent on-demand emission of a guided single photon, and that this nonclassical state can be preferentially coupled to a waveguide.

C. Slow guided light and quantum memory

Interfacing guided light with an atomic array has been foreseen as a promising alternative, enabling longer interaction length and large optical depth, which are crucial for
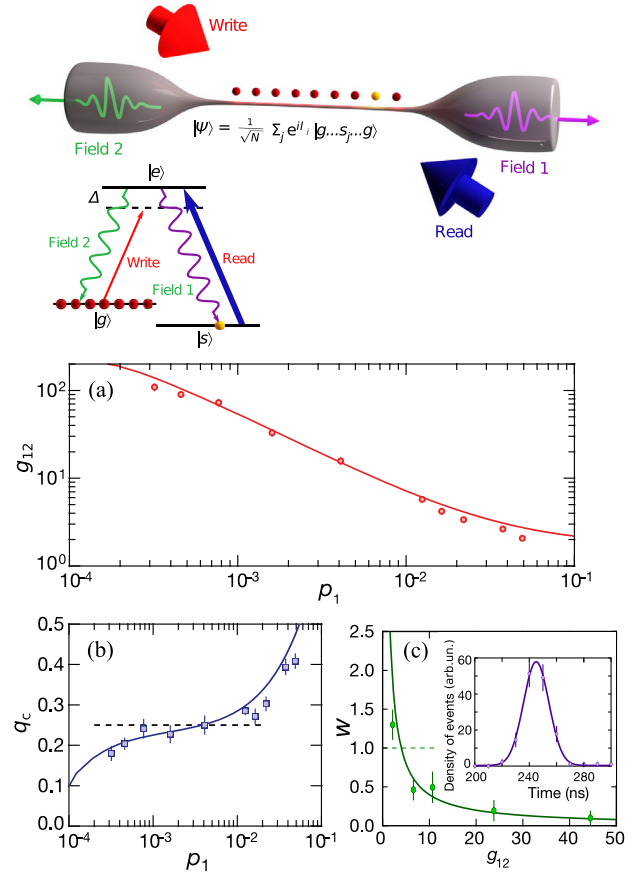

FIG. 25. Waveguide-coupled collective excitation of an atomic array. Top panel: DLCZ scheme (Duan *et al.*, 2001). One single-flip excitation is created in a chain of N atoms trapped near an optical nanofiber by an external optical pulse that is detuned from the atomic $|g\rangle \rightarrow |e\rangle$ transition. This process is heralded by the detection of a photon in the guided field-1 mode. Later, a read pulse resonant to the $|s\rangle \rightarrow |e\rangle$ atomic transition converts the excitation into a single photon in the guided field-2 mode. Lower panel: characterization of the collective excitation. (a) Normalized cross-correlation function g_{12} between field 1 and field 2. (b) Conditional retrieval efficiency q_c as a function of the probability p_1 for detecting a heralding photon in field 1. (c) Suppression of the two-photon component of field 2. From Corzo *et al.*, 2019.

quantum memory applications (Gorshkov *et al.*, 2007). In an optical nanofiber, a propagating single-mode field experiences a dispersion due to the dispersive material contents of the core and clad. The group velocity of the envelope of such a propagating fiber mode is $v_g = d\omega/dk_{1D}$, with k_{1D} the propagation constant of the fiber mode. The group velocity of the fiber mode can be significantly reduced under conditions of EIT. The light delay propagating in an optical nanofiber was theoretically studied by Patnaik, Liang, and Hakuta (2002) and Song *et al.* (2017), and the first experimental demonstrations were done by Gouraud *et al.* (2015) and Sayrin *et al.* (2015). The main difference between these two experiments consists in prepared atomic systems. Thus, in the work of Gouraud *et al.* (2015) a cloud of laser-cooled atoms overlapped with a nanofiber, while in the work of Sayrin *et al.* (2015) laser-cooled cesium atoms were confined

to a one-dimensional optical lattice realized in an evanescent field surrounding an optical nanofiber.

Guided light propagating through an optical nanofiber has a complex polarization pattern, including a significant nontransverse component. The transmission coefficient of weak intensity light propagating through a dilute atomic cloud with an OD has an exponential dependence $\sim \exp\{-\mathrm{OD}/[1 + (2\Delta/\Gamma_{\mathrm{tot}})^2]\}$, where Δ and Γ_{tot} are detuning from the atomic resonance and the total decay rate of the atomic excited state. The transmission coefficient of the guided light in a nanofiber-mediated atomic cloud is displayed in blue in Fig. 26(d).

The fitting of the experimental data with the exponential profile yielded OD = 3 and $\Gamma_{\mathrm{tot}}/2\pi = 6.8$ MHz. Notice that this value is 30% larger than the natural linewidth in free space $\Gamma_0/2\pi = 5.2$ MHz resulting from the finite temperature, surface interactions, and modification of the spontaneous emission rate near the fiber. Sayrin *et al.* (2015) obtained OD = 6 and $\Gamma_{\mathrm{tot}}/2\pi = 6.4$ MHz with a similar fitting.

It is well known that a strong control field changes the transmission characteristics of the probe field. Figure 26(d) shows an example of the transmission profiles of the signal as a function of its spectral detuning δ from the resonance of the atomic transition $|g\rangle \to |e\rangle$ for different values of the control field power from Gouraud *et al.* (2015). When the control field is applied, a transparency window appears, providing a first signature of EIT in this evanescent-field configuration. Transparency close to 80% was achieved in both experiments. After having EIT transparency, the slow-light effect resulting from the guided light propagation under the EIT condition can be measured. As a signal pulse, a weak laser pulse at a single-photon level was used. The results for the light delay are demonstrated in Fig. 26(b) for the work of Gouraud *et al.* (2015) and in Fig. 27(a) for the work of Sayrin *et al.* (2015). Larger delays are obtained when the control field is decreased due to the narrower transparency window. For a 0.5 mW control field power, a light delay of 60 ns was observed by Gouraud *et al.* (2015) and a light delay of 5 μs was achieved with a control field power 0.7 pW by Sayrin *et al.* (2015).

In addition, the storage of the guided light can be demonstrated by switching off the control field. This corresponds to an implementation of the dynamical EIT protocol. While the light is slowed down, the control is ramped down to zero and the signal pulse is converted into a collective atomic excitation. After a controllable delay, the control field can be switched on again and the light can be retrieved in a well-defined spatiotemporal mode due to the collective enhancement provided by the atomic ensemble. Figures 26(c) and 27(b) demonstrate the storage results for a signal with mean photon numbers per pulse equal to 0.6 and 0.8, respectively. Owing to the limited delay, the pulse cannot be contained entirely in the ensemble, and leakage is observed before the control pulse is switched off. The crucial parameter characterizing the memory is its efficiency, which can be defined as a ratio of the photodetection events in the retrieved pulse to the ones in the reference. Efficiencies of $\eta = 10\%$ and 3% were obtained in these experiments. These efficiencies are compatible with the limited OD used in the experiments. These two experiments demonstrated that the interaction of
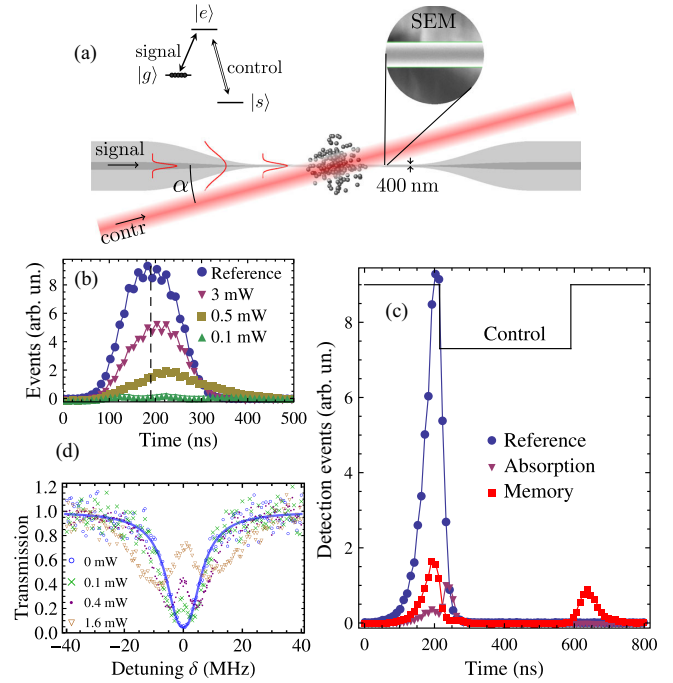

FIG. 26. (a) Nanofiber with a diameter 400 nm overlapped with an ensemble of cold atoms of ^{133}Cs. The signal pulse is a guided mode field, and the control pulse is external to the nanofiber. (b) Transmitted pulses for different control powers. The reference is measured without atoms. (c) Storage and retrieval of the guided light with an exponentially rising profile with a full width at half maximum of 60 ns. In the absence of a control field, the blue circles and purple triangles give the transmitted pulse without and with atoms. The red squares correspond to the memory sequence, showing leakage and retrieval. The solid black line indicates the control timing. (d) EIT for the guided light. The control field is on resonance with the $|s\rangle \to |e\rangle$ transition, while the signal is detuned by Δ from the $|g\rangle \to |e\rangle$ atomic resonance. From Gouraud *et al.*, 2015.

the evanescent field propagating through an optical nanofiber with the surrounding atoms provides an intrinsically fibered memory that has potential applications.

D. Subradiant excitations in the qubit array

Thus far we have considered experiments probing symmetric superradiant modes of the atomic array. However, as previously discussed in the context of Fig. 10, there are also subradiant modes with a strongly suppressed radiative decay compared to a single atom. The lifetime of the darkest subradiant modes tends to increase with the number of atoms N, as either N^3 [Eq. (19) (Zhang and Mølmer, 2020)] or even faster (Kornovan *et al.*, 2019).

However, the large radiative lifetime also means that it is hard to address subradiant states in experiments. We illustrate this by discussing the state-of-the-art experiment by Brehm *et al.* (2021) for an array of artificial atoms, superconducting qubits, coupled to the waveguide. The structure consisted of eight transmon qubits, as illustrated in Fig. 28(a). The spacing of the qubits was approximately 40 times smaller than the electromagnetic wavelength at the qubit resonance, so
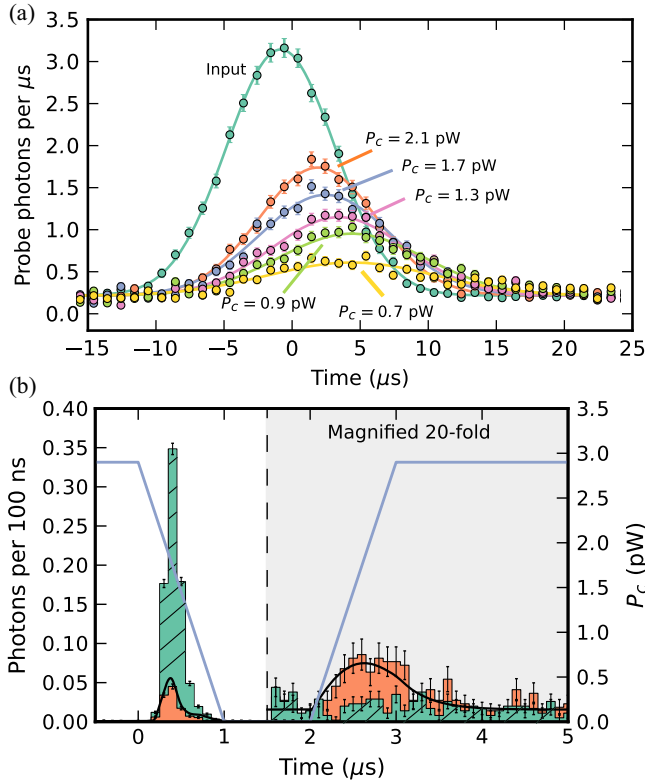
(a)

FIG. 27. (a) Slow guided light. A light delay with respect to a reference pulse (indicated as "input") is visible. The solid lines correspond to Gaussian fits of the experimental data at different powers, which are indicated near the curves. (b) Storage of light in a nanofiber-trapped ensemble of cold atoms. A pulse duration of $\tau = 0.2$ μs contains 0.8 photon on average. The storage time was chosen as 1 μs. The data corresponding to a green area with a slanted pattern represent the reference recorded without atoms. The black solid line is the simulated time trace. The homogeneous magnetic field is $B_{\text{off}} = 15$ G. From Sayrin *et al.*, 2015.
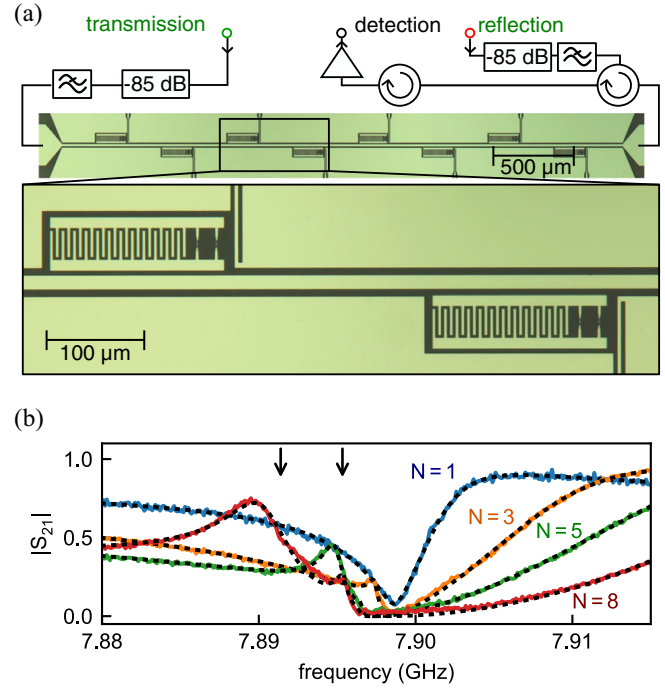
FIG. 28. (a) Optical micrograph of the eight-qubit metamaterial composed of superconducting transmon qubits capacitively coupled to a coplanar waveguide. Local flux-bias lines provide individual qubit frequency control in the range of 3–8 GHz. (b) Transmission spectra $|S_{21}|$ for different numbers N of resonant qubits with the resonant frequency $f = 7.898$ GHz and low drive powers. With an increasing N, the emergence of subradiant states (visible as peaks in transmission) can be observed. The black dotted lines are fits to the expected transmission using a transfer matrix calculation. Black vertical arrows indicate the calculated frequencies of the two brightest subradiant states for $N = 8$. From Brehm *et al.*, 2021.

the array can be viewed as a quantum metamaterial. In the experiment, the amplitude transmission coefficient of the electromagnetic wave through the metamaterial $S_{21} \equiv t(\omega)$ has been measured. The setup allows one to tune the resonant frequencies of the qubits independently by applying an external voltage. Thus, by tuning a given number of the consecutive qubits $N \leq 8$ to the resonance and detuning the remaining qubits, it has been possible to study the dependence of the transmission spectra on N. The experimental results are presented in Fig. 28(b). The experiment has been performed for low excitation powers. For $N = 1$, the transmission spectrum has a dip at the qubit resonance frequency. In contrast to the theoretically predicted Lorentzian, the experimental spectrum is slightly asymmetric. This Fano-like asymmetry originates from the interference between the resonant scattering on the qubit and the multiple reflections from the edges of the waveguide. Figure 28(b) demonstrates that an increase of the number of qubits leads to suppression of the transmission around the qubit resonance. This reflects the formation of the polariton band gap for the coupled photon-qubit excitations. At the same time, additional peaks appear with an increase of N below the qubit resonance.

These peaks correspond to subradiant excitations of the array (discussed in Sec. III.A.2). Namely, they can be obtained by diagonalizing the effective Hamiltonian matrix (15). However, only up to two brightest subradiant modes have been resolved in the experiment. This is due to the quality of the sample: the ratio of nonradiative to radiative decay rates γ/γ_{1D} was on the order of 10%. Thus, the darkest subradiant modes decay mostly nonradiatively and are not resolved in transmission spectra. The experiment of Brehm *et al.* (2021) reveals the potential of the superconducting qubit arrays. A natural extension of this work would be to demonstrate the slow-light effect due to a lower group velocity of polaritons near the resonance. It is also potentially possible to further increase both the quality and the number of qubits, which will enable slowing and storing microwave pulses propagating through the array (Leung and Sanders, 2012).

Another application of the subradiant states with superconducting qubits could be related to the quantum measurements. Quantum nondemolition single-microwave photon detector remains a challenge (Royer *et al.*, 2018; Blais *et al.*, 2021; Grimsmo *et al.*, 2021). The proposal of Royer *et al.* (2018) is based on a signal waveguide photon being absorbed by an array of superconducting qubits. Next the absorption of

photon by the array leads to coherent state displacement in an additional harmonic mode that is detected using homodyne measurement. The essence of the proposal is the engineering of the system in such a way that a signal photon is absorbed into the bright state of the qubit array, transferred to a long-lived subradiant state, and, after some time, returns to the bright state, where it is reemitted. The measurement efficiency is enhanced due to the long lifetime of the collective subradiant state.

E. Bragg-spaced arrays

In this section, we discuss in more detail the experimental results of Corzo *et al.* (2016) for a waveguide-coupled atomic array. The theoretical background for Bragg structures was presented in Sec. III.A.2. In this experiment, the array of $N = 2000$ trapped atoms of ^{133}Cs was prepared in the evanescent field of a 400 nm diameter nanofiber with a lattice constant d close to $\lambda_0/2$, where λ_0 is the wavelength of the atomic transition. For this array of $N = 2000$ atoms, the reflection up to 75% was achieved. For comparison, the 80% reflection was achieved in a free-space experiment with 10^7 atoms (Schilke *et al.*, 2011). While we considered a symmetric nonchiral situation previously in this section, the experiment of Corzo *et al.* (2016) also demonstrated the effect of the waveguide chirality arising from the complex polarization pattern. Namely, each atom exhibits the radiative decay rates $\gamma^\rightarrow$ and $\gamma^\leftarrow$ into the right- and left-propagating modes, respectively, and $\gamma \sim \gamma_0$ into all other modes, with γ_0 the free-space radiative decay rate; see Fig. 29(a). For a guided probe field quasilinearly polarized along the y direction, the two decay rates are equal: $\gamma^\rightarrow = \gamma^\leftarrow = \gamma_{1D}/2$. In contrast, for an orientation along the x direction the couplings to the waveguide become strongly asymmetric (Le Kien and Rauschenbeutel, 2014). In the case of asymmetric coupling, the forward decay rate is increased sixfold, while the backward decay rate is suppressed by about 1 order of magnitude. To examine the effect of asymmetric coupling in experiment, one can compare the light reflection spectra in x and y polarizations.

Figures 29(c) and 29(d) provide theoretical reflection spectra calculated for different small detunings $\Delta\lambda$ of the trap wavelength to atomic resonance and for the two orthogonal polarizations. The calculations are performed using the transfer matrix formalism discussed in Appendix B. For atoms separated by exactly $\lambda_0/2$, the reflection spectrum has a broadened Lorentzian profile in the symmetric coupling case, while the reflectance is strongly suppressed in the chiral case. Indeed, the amount of chirality and the number of atoms result in a finite bandwidth around resonance where reflection is suppressed. One can see that close to the commensurate array the Bragg condition is fulfilled out of resonance. This leads to a maximum reflectance shifted to the blue but also results in an increased reflectance for the chiral case. Large reflectance values can then be obtained for both polarizations, as the single-atom reflection coefficients are similar in the chosen configuration.

The measured reflection spectra for both x- and y-polarization profiles are shown in Fig. 30(a). The achievable filling factor is around 0.5, with random occupation of the lattice sites by the
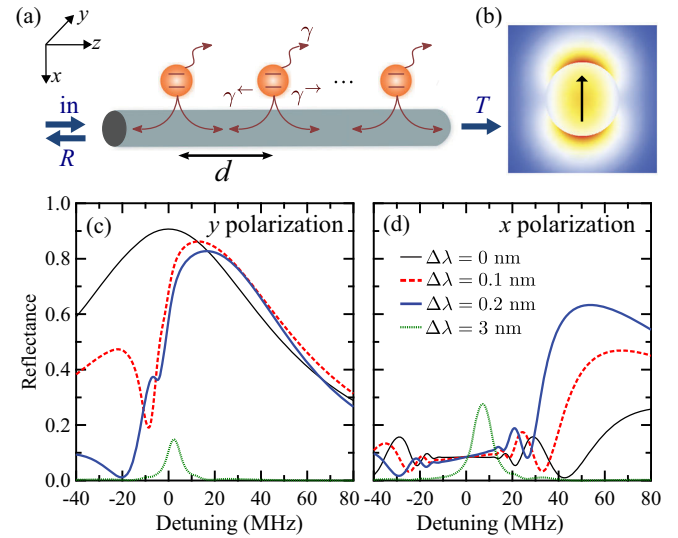

FIG. 29. Bragg reflection from atoms coupled to a one-dimensional waveguide. (a) N atoms trapped near a waveguide and exhibiting radiative decay rates $\gamma^\rightarrow = \gamma^\leftarrow$ into the right- and left-propagating modes, respectively, and $\gamma \sim \gamma_0$ into all other modes. (b) Electric field distribution in the transverse plane of a nanofiber for a guided probe field with a quasilinear polarization (indicated by the arrow). Theoretical reflection spectra for a probe quasi-linearly polarized (c) along the y direction (symmetric decay rates) and (d) along x direction (asymmetric decay rates). The spectra are given for different distances between the atoms, with values close to the commensurate case. $\Delta\lambda$ stands for the trap detuning from the resonance, with $d = \lambda_0/2 + \Delta\lambda/2$. The calculation parameters are $N = 2000$, $\gamma_{1D}/\gamma_0 = 0.007$, $\gamma^\rightarrow = 2.8\gamma_{1D}$, and $\gamma^\rightarrow/\gamma^\leftarrow = 12$. From Corzo *et al.*, 2016.

atoms. In Fig. 30, the estimated filling factor was around 0.3; nevertheless, one can observe the pronounced Bragg peak in the reflection spectrum averaged over multiple realizations. One of the possible mechanisms of this tolerance is related to directional interaction with the waveguide mode and suppressed reflection. The trap detuning was fixed at $\Delta\lambda = 0.2$ nm, which adds slight disorder in the atomic array. However, one can see that the reflection spectrum is significantly shifted and broadened in the asymmetric case of x polarization (red curves). These features are compelling signatures of the chiral character of the waveguide on the reflection, as confirmed by the associated simulations shown in Fig. 30(b). Notice that the maximal observed reflectance of 0.75 ± 0.06 was obtained in the asymmetric case at a probe detuning of 25 MHz. Beyond their fundamental significance, observation of the chiral character of the nanofiber demonstrates key ingredients for the exploration of a variety of emerging and potentially rich protocols based on 1D reservoirs coupled to atoms.

V. SUMMARY AND OUTLOOK

In this review, we provided an introduction in the emerging field of waveguide quantum electrodynamics. We considered various experimental platforms and described in detail several recent groundbreaking experiments devoted to light-matter interactions in the quantum regime, including tunable
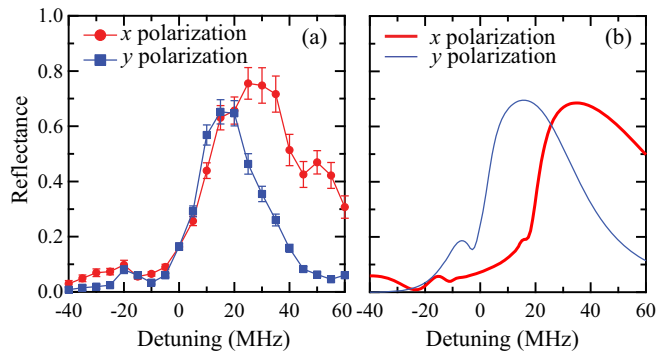
FIG. 30. Effect of the chiral character of the waveguide on the Bragg reflection. (a) Measured reflection spectra for x and y quasilinear polarizations, with $\Delta\lambda = 0.2$ nm. (b) Theoretical simulations done with $N = 2000$, $\gamma_{1D}/\gamma_0 = 0.007$, $\gamma^{\rightarrow}/\gamma^{\leftarrow} = 12$, and $f = 0.3$.

bunching and antibunching of emission due to the formation of bound photon states, resonant light reflection from atommade quantum metasurfaces, and topological quantum optics. We also provided a detailed introduction into various theoretical techniques useful in quantum optics consisting of ordered one-dimensional atomic arrays in the waveguide.

Given the advances in the WQED field in the last five to ten years, it is difficult to predict specific directions of future development, but substantial progress can certainly be expected. Not only will the current WQED platforms continue to develop but new types of structures could also become prominent, such as those based on Rydberg superatoms, topologically nontrivial waveguides, or even Mössbauer nuclei (Röhlsberger and Evers, 2021); see the discussion in Sec. II.C. We can also envisage the arrival of hybrid quantum systems involving interacting excitations of different origins. For example, one could think of tripartite systems with interacting atomic excitations, photons, and atomic vibrations in the quantum regime. There have already been a number of relevant experimental demonstrations (Lecocq *et al.*, 2016; Bothner, Rodrigues, and Steele, 2021) and theoretical predictions (Chang, Cirac, and Kimble, 2013; Iorsh, Poshakinskiy, and Poddubny, 2020; Sedov, Kozin, and Iorsh, 2020), and the field of WQED may soon be complemented by waveguide quantum optomechanics. Another type of quasiparticle that can be interfaced with superconducting circuits is offered by collective spin excitations in ferromagnetic crystals; see Lachance-Quirion *et al.* (2019). The photon excitations can also be substituted for atomic waves in an optical lattice, giving rise to matter-wave polaritons (Kwon *et al.*, 2022). The entire concept of WQED might evolve, fuse with circuit QED, and include structures with two-dimensional arrays of waveguides (Marques, Shelykh, and Iorsh, 2021), or even more complicated topologies.

The focus of research will probably shift from pioneering demonstrations of cooperative light-matter interactions, such as generation of superradiant and subradiant states, to the studies of advanced highly excited and highly entangled quantum states of atoms and photons. Different protocols are currently under development that explore both the possibility of cascaded photon processing in one-dimensional

structures (Guimond *et al.*, 2020) and the possibility of two-dimensional arrays to parallelize photon processing (Bekenstein *et al.*, 2020; Bettles *et al.*, 2020) for the generation of photon cluster states and cat states. In addition to potential applications for quantum information processing, WQED systems can act as quantum simulators useful for fundamental problems from many-body and condensed matter physics. Some examples include topological quantum Hall phases induced by interactions (Poshakinskiy *et al.*, 2021) or an external magnetic field (De Bernardis *et al.*, 2021). An advantage of the optical setup over the more conventional condensed matter ones is the possibility to visualize interesting quantum states, such as the fractional quantum Hall phase (Perczel *et al.*, 2020). Recently self-ordering of photons in the WQED setup with three-level atoms with Laughlin-like photon states was predicted by Iversen and Pohl (2022). The situation becomes interesting when disorder is taken into account. Single-photon properties of disordered arrays have already been studied (Haakh, Faez, and Sandoghdar, 2016; Mahmoodian *et al.*, 2018; Song *et al.*, 2021; Fedorovich *et al.*, 2022), but the many-body problem of photons interacting with atoms in the disordered structure is especially interesting. For example, recent numerical calculations indicate that the WQED system exhibits many-body localization instead of conventional thermalization (Fayard *et al.*, 2021). The localization phase occurs, provided that the excitation filling factor in the array of two-level atoms is less than $1/2$. At larger filling factors, the states are delocalized, which may be related to saturation of the optical transitions. The filling factor of $1/2$ seems to be a special value because subradiant states in the subwavelength array also disappear above this threshold (Poshakinskiy and Poddubny, 2021). The interplay of disorder and dissipation in this system certainly merits future study. Another interesting type of many-body phases in the Dicke model is related to spin glasses (Gopalakrishnan, Lev, and Goldbart, 2011; Strack and Sachdev, 2011; Rotondo, Cosentino Lagomarsino, and Viola, 2015). Specifically, cavity-mediated coupling between the atoms can be mapped to the effective long-range spin-spin interactions. One of the interesting features of the spin-glass model is the similarity to the Hopfield associative memory. Thus, certain elements of "machine learning behavior" emerge in the strongly coupled multimode Dicke model (Fiorelli *et al.*, 2020). Namely, the atomic array behaves as a basic associative memory with stationary states corresponding to the retrieval phase of the Hopfield neural network (Hopfield, 1982), characterized by the ability to recall previously stored information. To our knowledge, the spin-glass behavior has thus far been theoretically studied only for atomic arrays in a cavity, and it is not yet clear what would happen in a strongly dissipative waveguide setup. Progress in artificial intelligence and machine learning will probably also inspire many studies in the realm of WQED. One can not only seek analogies between processes in quantum systems and neural networks but also apply machine learning approaches to better understand the results of numerical calculations (Che *et al.*, 2020) and experiments (Ahmed *et al.*, 2021). Thus far we have discussed stationary many-body phases. It would also be interesting to examine how the so-called time-crystal phases that

break time-translation symmetry (Carollo, Brandner, and Lesanovsky, 2020) are manifested in the WQED setup.

To summarize, the possibility of tuning energies and interactions of atoms and of probing the wave functions at individual atoms is unprecedented for conventional solid-state systems and will inspire many interesting experiments. We refer the interested reader to recent reviews by Noh and Angelakis (2017) and Chang *et al.* (2018) and original theoretical works on quantum simulators based on the atomic arrays by Douglas *et al.* (2015), González-Tudela *et al.* (2015), and Hung *et al.* (2016). We hope that all these intriguing predictions will soon inspire new theoretical concepts, experimental demonstrations, and eventually practical applications for quantum technologies.

ACKNOWLEDGMENTS

APPENDIX A: INPUT-OUTPUT FORMALISM

Here we outline the input-output formalism (Gardiner and Collett, 1985; Walls and Milburn, 2007) for an ensemble of two-level atoms interacting with a single mode of photons with linear dispersion, propagating in a waveguide, and discuss its limitations. The derivation mostly follows Caneva *et al.* (2015).

The system under consideration is described by the following sum of a photon Hamiltonian H_{phot}, an atom Hamiltonian H_{atom}, and an atom-photon interaction Hamiltonian $H_{\text{atom-phot}}$:

$$H = H_{\text{phot}} + H_{\text{atom}} + H_{\text{atom-phot}},$$

$$H_{\text{phot}} = \sum_k \omega_k a_k^\dagger a_k, \qquad H_{\text{atom}} = \omega_0 \sum_{m=1}^N \sigma_m^\dagger \sigma_m, \qquad \text{(A1)}$$

$$H_{\text{atom-phot}} = -\sum_{m=1}^N \hat{\boldsymbol{d}} \cdot \hat{\boldsymbol{E}}(z = z_m). \qquad \text{(A2)}$$

In Eqs. (A1) and (A2) we set $\hbar = 1$, $\omega_k = c|k|$ is the frequency of the photonic mode with the wave vector k, c is the light speed in the waveguide, and $\sum_k \equiv L \int_{-\infty}^\infty dk/2\pi$, where L is the normalization length. The bosonic operators $a_k^\dagger$ and $b^\dagger$ describe the creation of the photon in the waveguide and the excitation of the atom, and $\sigma \equiv |e\rangle\langle g|$, where $|g\rangle$ and

$|e\rangle$ are the ground and excited atom states. The light-atom coupling is treated in the dipole approximation with the dipole momentum operator $\hat{\boldsymbol{d}} = \boldsymbol{d}b + \boldsymbol{d}^* b^\dagger$, where $\boldsymbol{d}$ is the matrix element of the electric dipole momentum between ground and excited states of the pointlike atom. The quantized electromagnetic field operator reads

$$\boldsymbol{E}(z,t) = \sum_k \sqrt{\frac{2\pi\omega_k}{LA}} e^{ikz} \boldsymbol{e}_k a_k(t) + \text{H.c.}, \qquad \text{(A3)}$$

where A is the normalization area (the effective cross section of the waveguide), $\boldsymbol{e}_k$ is the unit photon polarization wave vector, and we use the Gaussian units system. In this appendix, we consider a resonant rotating wave approximation in which the Hamiltonian $H_{\text{atom-phot}}$ can be reduced to

$$H_{\text{atom-phot}} = \frac{1}{\sqrt{L}} \sum_{m=1}^N \sum_k (g_k e^{-ikz_m} a_k^\dagger \sigma_m + g_k^* e^{ikz_m} a_k \sigma_m^\dagger), \qquad \text{(A4)}$$

with $g_k = -\sqrt{2\pi\omega_k/A}\boldsymbol{d} \cdot \boldsymbol{e}_k^*$. This rotating wave approximation holds provided that the array is excited resonantly and that the atom-photon coupling is reasonably weak ($|g_k|/\sqrt{L} \ll \omega_0$). An ultrastrong coupling regime in which $g/\sqrt{L} \sim \omega_0$ and the counterrotating terms cannot be ignored was considered in Sec. III.A.4. In the same Markovian approximation, the dependence of g on the light wave vector k can be simplified to $g_k = g_{\omega_0/c} \equiv g_+$ for $k > 0$ and $g_k = g_{-\omega_0/c} \equiv g_-$ for $k > 0$. We also introduce annihilation operators corresponding to forward- and backward-propagating photons,

$$a_\rightarrow(z,t) = \sum_{k>0} a_k(t) e^{ikz}, \qquad a_\leftarrow(z,t) = \sum_{k<0} a_k(t) e^{ikz}. \qquad \text{(A5)}$$

The Heisenberg equations for these operators read (Caneva *et al.*, 2015)

$$a_\rightarrow(z,t) = a_{\text{in},\rightarrow}(t - z/c)$$
$$- \frac{ig_+\sqrt{L}}{c} \sum_{m=1}^N \theta(z - z_j)\sigma_m(t - |z - z_m|/c), \qquad \text{(A6)}$$

where the operator $a_{\text{in},\rightarrow}(t - z/c)$ describes the field that is incident from the left. For backward-propagating operators, $\theta(z - z_m)$ in Eq. (A6) is to be replaced by $\theta(z_m - z)$, $a_{\text{in},\rightarrow}(t - z/c)$ is replaced by the backward-propagating input field $a_{\text{in},\leftarrow}(t + z/c)$, and g_+ is replaced by g_-. The equation of motion for the atomic operators is (Caneva *et al.*, 2015)

$$\frac{d\sigma_m}{dt} = -i\omega_0\sigma_m - \frac{i(1 - 2\sigma_m^\dagger\sigma_m)}{\sqrt{L}}[g_+^* a_{\text{in},\rightarrow}(t) + g_-^* a_{\text{in},\leftarrow}(t)]$$
$$- \gamma_{1D} \sum_{n=1}^N \sigma_n(t - |z_m - z_n|/c), \qquad \text{(A7)}$$

where we have introduced the rate of spontaneous emission into the waveguide: $\gamma_{1D} = |g_+^2|/c = |g_-^2|/c$. From now on, we

consider a situation in which $|g_+| = |g_-|$; a more general case with chiral coupling was discussed in Sec. III.B.

We now use the Markovian approximation

$$\sigma_n(t - |z_m - z_n|/c) \approx \sigma_n(t)e^{i\omega_0|z_m - z_n|/c} \quad \text{(A8)}$$

provided that the structure is not too long. A more general, non-Markovian input-output approach was given by Fang, Ciccarello, and Baranger (2018). Equation (A7) then reduces to

$$\frac{d\sigma_m}{dt} = i[H_{\text{eff}}, \sigma_m] - \frac{i(1 - 2\sigma_m^\dagger \sigma_m)}{\sqrt{L}}[g_+^* a_{\text{in},\rightarrow}(t) + g_-^* a_{\text{in},\leftarrow}(t)],$$
$$\text{(A9)}$$

and

$$H_{\text{eff}} = \sum_{m=1}^{N} \omega_0 \sigma_m^\dagger \sigma_n - i\gamma_{1D} \sum_{m,n=1}^{N} \sigma_m^\dagger \sigma_n e^{i\omega_0|z_m - z_n|/c} \quad \text{(A10)}$$

is the effective atomic Hamiltonian with traced out photonic degrees of freedom. This is equivalent to Eq. (8) if the replacement $k_z \rightarrow \omega_0/c$ is made.

The treatment becomes simpler when the input field is in the coherent state. In this case, it is convenient to determine the system density matrix ρ from the master equation $\partial_t \rho = i[\rho, \mathcal{H}] + L\rho$ and then to find the scattered light. Specifically, we consider the case in which the structure is driven from the left by a coherent field at frequency ω. The Hamiltonian H entering the master equation then reads

$$H = \frac{\Omega}{2} \sum_{m=1}^{N} (e^{i\omega(z_m/c - t)} \sigma_m^\dagger + \text{H.c.}) + \frac{H_{\text{eff}} + H_{\text{eff}}^\dagger}{2}, \quad \text{(A11)}$$

where Ω is the Rabi frequency. The Hamiltonian (A11) includes the Hermitian part of the effective Hamiltonian (8). The non-Hermitian part describing the decay processes is incorporated into the Lindblad operator

$$\mathcal{L}\rho = \sum_{m,n=1}^{N} \left[\gamma_{1D} \cos\frac{\omega_0(z_m - z_n)}{c} + \delta_{m,n}\gamma \right]$$
$$\times (2\sigma_m \rho \sigma_n^\dagger - \sigma_m^\dagger \sigma_n \rho - \rho \sigma_m^\dagger \sigma_n). \quad \text{(A12)}$$

We have also added nonradiative damping term γ to the Lindblad operator. Once the density matrix has been found, the coherent reflection coefficient is given by

$$r = \frac{2i\gamma_{1D}}{\Omega} \sum_{m=1}^{N} e^{i\omega_0 z_m/c} \langle\sigma_m(t)\rangle e^{i\omega t}, \quad \text{(A13)}$$

and the coherent transmission coefficient reads

$$t = 1 + \frac{2i\gamma_{1D}}{\Omega} \sum_{m=1}^{N} e^{-i\omega_0 z_m/c} \langle\sigma_m(t)\rangle e^{i\omega t}. \quad \text{(A14)}$$

More details on the input-output formalism in the WQED setup were given by Lalumière *et al.* (2013) and Das *et al.* (2018).

APPENDIX B: THE TRANSFER MATRIX METHOD

The easiest way to calculate single-photon reflection and transmission coefficients for an arbitrarily spaced atomic array coupled to the waveguide is offered by the transfer matrix method (Corzo *et al.*, 2016). The electric field to the left and right of an atom located at the point $z = 0$ is given as

$$E(z) = \begin{cases} E_L^\rightarrow e^{i\omega z/c} + E_L^\leftarrow e^{-i\omega z/c} & (z < 0), \\ E_R^\rightarrow e^{i\omega z/c} + E_R^\leftarrow e^{-i\omega z/c} & (z > 0), \end{cases} \quad \text{(B1)}$$

where we assume an $e^{-i\omega t}$ time dependence. The fields to the left and right of the atom are linked,

$$\begin{pmatrix} E_R^\rightarrow \\ E_R^\leftarrow \end{pmatrix} = M_{\text{atom}} \begin{pmatrix} E_L^\rightarrow \\ E_L^\leftarrow \end{pmatrix}, \quad \text{(B2)}$$

by the transfer matrix

$$M_{\text{atom}} = \frac{1}{t_\leftarrow} \begin{pmatrix} t_\rightarrow t_\leftarrow - r^2 & r \\ -r & 1 \end{pmatrix}, \quad \text{(B3)}$$

which is expressed via the reflection and transmission coefficients r and $t_{\rightarrow/\leftarrow}$ given by Eqs. (57). Equation (B3) is written for the case of general chiral coupling, where forward ($t_\rightarrow$) and backward ($t_\leftarrow$) transmission coefficients can differ; see Eqs. (57). The transfer matrix through the free part of the waveguide with length d can be given as

$$M_d = \begin{pmatrix} e^{i\omega d/c} & 0 \\ 0 & e^{-i\omega d/c} \end{pmatrix}. \quad \text{(B4)}$$

By multiplying these matrices, we obtain the following total transfer matrix through an array of N atoms with period d:

$$M_N = (M_d M_{\text{atom}})^N, \quad \text{(B5)}$$

which allows one to find the reflection and transmission coefficients

$$r_N^\leftarrow = -\frac{[M_N]_{2,1}}{[M_N]_{2,2}}, \qquad t_N^\rightarrow = \frac{\det M_N}{[M_N]_{2,2}}. \quad \text{(B6)}$$

In a case of symmetric coupling in which $t_\rightarrow = t_\leftarrow = t$, it is also possible to obtain analytical expressions for Eqs. (B6) that read (Ivchenko, 2005)

$$r_N^\leftarrow = \frac{\tilde{r}\sin NKd}{\sin NKd - \tilde{t}\sin(N-1)Kd}, \qquad t_N^\rightarrow = \frac{\tilde{t}\sin Kd}{\tilde{r}\sin NKd} r_N^\leftarrow, \quad \text{(B7)}$$

where $\tilde{t} = te^{i\omega d/c}$ and $\tilde{r} = re^{i\omega d/c}$ are the transmission and reflection coefficients through one period of the array.

APPENDIX C: PHOTON PAIR SCATTERING FROM A SINGLE ATOM

Here we solve the problem regarding photon pair scattering on a single atom. A general diagrammatic Green's function approach to solve a more general problem for N atoms is discussed in Appendix G. The goal of this appendix is to present a more straightforward technique that does not require prior knowledge of Green's function theory. Instead of solving the real-space differential equations for the two-photon wave function, as done by Shen and Fan (2007a, 2007b), we solve the Schrödinger equation directly in the double-excited subspace of the Hilbert space. The procedure can be viewed as a "poor man's" version of the Bethe *Ansatz* technique, which is discussed in Appendix D. We start with the Hamiltonian

$$
\begin{aligned}
H &= H_{\text{phot}} + H_{\text{atom}} + H_{\text{atom-phot}} \\
&= \sum_k \omega_k a_k^\dagger a_k + \omega_0 b^\dagger b + \frac{U}{2} b^\dagger b (b^\dagger b - 1) \\
&\quad + \frac{g}{\sqrt{L}} \sum_k (a_k^\dagger b + a_k b^\dagger).
\end{aligned} \tag{C1}
$$

The wave function is sought in the form

$$
|\psi\rangle = \sum_k \sum_{k'} E_{kk'} \frac{a_k^\dagger a_{k'}^\dagger}{2} |0\rangle + \sum_k P_k a_k^\dagger b^\dagger |0\rangle + Q \frac{b^{\dagger,2}}{2} |0\rangle. \tag{C2}
$$

In Eq. (C2) $|0\rangle$ is a state with zero photons and the atom in its ground state. Equation (C2) contains all possible combinations of the double-excited states, namely, the states with two photons, the states with one photon absorbed and the atom in the double-excited state, and the state with a double-excited atom. The Schrödinger equation for the double-excited states reads

$$
E_{kk'} \omega_k + \omega_{k'} + \frac{g}{\sqrt{L}} (P_k + P_{k'}) = 2\varepsilon E_{kk'}, \tag{C3}
$$

where 2ε is the total energy. However, we need to take into account the fact that the structure is excited from the left by the two photons with the energy ε and the wave vector $k = \varepsilon/c$. To describe this, we add an inhomogeneous term to Eq. (C3), corresponding to the excitation so that, in the absence of atoms, one has $E_{kk'} = \delta_{k,\varepsilon/c} \delta_{k',\varepsilon/c}$. The result is

$$
E_{kk'} + \frac{g/\sqrt{L}}{\omega_k + \omega_{k'} - 2\varepsilon - i0} (P_k + P_{k'}) = \delta_{k,\varepsilon/c} \delta_{k',\varepsilon/c}. \tag{C4}
$$

In Eq. (C4) the term $-i0$ in the denominator represents an infinitely small imaginary part that has been added for regularization purposes. The Schrödinger equation for the states, where one photon has been absorbed, reads

$$
(\omega_k + \omega_0 - 2\varepsilon) P_k + \frac{g}{\sqrt{L}} \sum_{k'} (E_{kk'} + E_{k'k}) + \frac{g}{\sqrt{L}} \sqrt{2} Q = 0. \tag{C5}
$$

Expressing the electric field in Eq. (C4) and substituting it into Eq. (C6), we find that

$$
\begin{aligned}
(\omega_k + \omega_0 - 2\varepsilon) P_k &= \frac{g^2}{L} P_k \sum_{k'} \frac{1}{\omega_k + \omega_{k'} - 2\omega - i0} \\
&\quad + \frac{g^2}{L} \sum_{k'} \frac{1}{\omega_k + \omega_{k'} - 2\omega - i0} P_{k'} \\
&\quad - g\sqrt{\frac{2}{L}} Q + \frac{2g}{\sqrt{L}} \delta_{k,\varepsilon/c}.
\end{aligned} \tag{C6}
$$

This summation can be carried out exactly in the rotating wave approximation,

$$
\int_{-\infty}^{\infty} \frac{dk}{2\pi} \frac{1}{\omega_k - \omega} \approx 2 \lim_{\delta \to 0} \int_{-\infty}^{\infty} \frac{dk}{2\pi} \frac{1}{ck - i\delta - \omega} = \frac{i}{c}. \tag{C7}
$$

In Eq. (C7) we split the integration into two parts, $\int_{-\infty}^{\infty} dk = \int_0^{\infty} dk + \int_{-\infty}^0 dk$, and then each of the two resulting integrals are extended back to the full axis, which results in the prefactor of 2. The result reads

$$
\begin{aligned}
(\omega_k + \omega_0 - 2\varepsilon - i\gamma_{\text{1D}}) P_k &= \frac{g^2}{L} \sum_{k'} \frac{1}{\omega_k + \omega_{k'} - i0 - 2\varepsilon} P_{k'} \\
&\quad - g\sqrt{\frac{2}{L}} Q + \frac{2g}{\sqrt{L}} \delta_{k,\varepsilon/c}.
\end{aligned} \tag{C8}
$$

The term $-i\gamma_{\text{1D}} P_k$ on the left-hand side of Eq. (C8) describes the spontaneous decay of the "propagating photon and excited atom" state into the state with two propagating photons. We now divide both parts of Eq. (C8) by $\omega_k + \omega_0 - 2\varepsilon$ and sum over k to find

$$
\sum_k P_k = \frac{2g/\sqrt{L}}{\omega_0 - \varepsilon - i\gamma_{\text{1D}}} - \frac{ig}{c} \sqrt{2L} Q, \tag{C9}
$$

where we have again used Eq. (C7). The sum stemming from the first term on the right-hand side of Eq. (C4) is zero,

$$
\sum_k \frac{1}{(\omega_k + \omega_0 - 2\varepsilon - i0)(\omega_k + \omega_{k'} - 2\omega - i0)} = 0. \tag{C10}
$$

The Schrödinger equation for the double-excited state is

$$
(2\omega_0 + U - 2\varepsilon) Q + g\sqrt{\frac{2}{L}} \sum_k P_k = 0. \tag{C11}
$$

Combining Eqs. (C11) and (C8), we find the amplitude of the double-excited state

$$
Q = -\frac{2\sqrt{2} g^2 / L}{(\omega_0 + U/2 - \varepsilon - i\gamma_{\text{1D}})(\omega_0 - \varepsilon - i\gamma_{\text{1D}})}. \tag{C12}
$$

We now solve Eq. (C8) for P_k. This can be done iteratively by treating the first term on the right-hand side as a perturbation:

$$P_k = P_k^{(0)} + P_k^{(1)} + \tilde{P}_k^{(1)}, \qquad (C13)$$

where

$$P_k^{(0)} = \frac{2g}{\sqrt{L}} \frac{\delta_{k,\varepsilon/c}}{\omega_0 - \varepsilon - i\gamma_{1D}}, \qquad (C14)$$

$$P_k^{(1)} = \frac{g^2}{L} \sum_{k'} \frac{1}{\omega_k + \omega_{k'} - 2\varepsilon} P_{k'}^{(0)} = \frac{2g^3}{L^{3/2}}$$

$$\times \frac{1}{(\omega_k + \omega_0 - 2\varepsilon - i\gamma_{1D})(\omega_k - \varepsilon - i0)(\omega_0 - \varepsilon - i\gamma_{1D})}, \qquad (C15)$$

and

$$\tilde{P}_k^{(1)} = -g\sqrt{\frac{2}{L}} \frac{Q}{\omega_k + \omega_0 - 2\varepsilon - i\gamma_{1D}}$$

$$= P_k^{(1)} \frac{\omega_k - \varepsilon}{\omega_0 + U/2 - \varepsilon - i\gamma_{1D}}. \qquad (C16)$$

The key observation is that the solution in Eq. (C13) is actually exact, and the higher-order terms are zero. Mathematically, the reason for the cancellation is the same as it is in Eq. (C10).

We are now in a position to find the amplitude of the incoherent two-photon scattering process. To this end, we substitute the solution (C13) into Eq. (C4). The terms $\propto P_k^{(0)}$ describe the incoherent scattering. The amplitude of the scattering matrix for the incoherent scattering process is given by

$$S(\omega_k, \omega_{k'} \leftarrow \varepsilon, \varepsilon) = 2\pi i \delta(\omega_k + \omega_{k'} - 2\varepsilon) M(\omega_k, \omega_{k'} \leftarrow \varepsilon, \varepsilon), \qquad (C17)$$

where

$$M(\omega_k, \omega_{k'} \leftarrow \varepsilon, \varepsilon) = \frac{L^2}{c^2} \frac{g}{\sqrt{L}} (P_k^{(1)} + \tilde{P}_k^{(1)} + P_{k'}^{(1)} + \tilde{P}_{k'}^{(1)}), \qquad (C18)$$

with $\omega_{k'} + \omega_k = 2\varepsilon$. Performing the summation of four terms in Eq. (C18), we obtain

$$M(\omega_k, \omega_{k'} \leftarrow \varepsilon, \varepsilon) = -\frac{4U\gamma_{1D}^2 s(\omega_k) s(\varepsilon) s(\omega_k')}{2\omega_0 + U - 2\varepsilon - 2i\gamma_{1D}}, \qquad (C19)$$

where $s(\omega) = 1/(\omega_0 - \omega - i\gamma_{1D})$. In the limit of a two-level atom $U \to \infty$, Eq. (C19) exactly matches the general result in Eq. (31) for an $N = 1$ atom.

The previous derivation becomes especially simple for a two-level atom, where $U \to \infty$, so $Q = 0$ and the terms $\tilde{P}^{(1)}$ can be neglected. It also explains how the incoherent scattering vanishes for a harmonic atom $U = 0$. In this case, the terms $P_k^{(1)} + P_{k'}^{(1)}$ and $\tilde{P}_{k'} + \tilde{P}_{k'}^{(1)}$ resulting from the single-excited and double-excited states cancel each other exactly.

APPENDIX D: PHOTON PAIR SCATTERING: THE BETHE *ANSATZ*

In this appendix, we consider the Dicke problem of photons interacting with an array of N identical two-level atoms. The derivation mostly follows the Bethe *Ansatz* approach by Rupasov and Yudson (1984), Shen and Fan (2007b), Yudson and Reineker (2008), and Roy (2013b).

We start by rewriting the Hamiltonian (C1) in real space as

$$H = -ic \int dx [a_\to^\dagger(x) \partial_x a_\to(x) - a_\leftarrow^\dagger(x) \partial_x a_\leftarrow(x)]$$

$$+ \sum_{\nu=\to,\leftarrow} [g[a_\nu^\dagger(0)\sigma + a_\nu(0)\sigma^\dagger]]. \qquad (D1)$$

In Eq. (D1) we assume that the two-level atoms with the excitations characterized by the destruction operators σ_j, $\sigma = \sum_{j=1}^N \sigma_j$, and $a_\nu^\dagger$ are the creation operators for right-going ($\nu =\to$) and left-going ($\nu =\leftarrow$) photons: $[a_\nu^\dagger(x), a_\nu(x')] = \delta(x - x')$. We also assume the rotating wave approximation measuring the energies from the atomic resonance ω_0 and set the normalization length L to unity in this appendix.

Owing to the mirror reflection symmetry $x \to -x$, the problem described by the Hamiltonian (D1) can be solved separately in even- and odd-scattering channels. Namely, if the new operators $a(x)$ and $a_0(x)$ are introduced as

$$a(x) = \frac{a_\to(x) + a_\leftarrow(-x)}{\sqrt{2}}, \qquad a_0(x) = \frac{a_\to(x) - a_\leftarrow(-x)}{\sqrt{2}}, \qquad (D2)$$

the Hamiltonian (D1) is separated as $H = H_{\text{even}} + H_{\text{odd}}$, where

$$H_{\text{even}} = -ic \int dx a^\dagger(x) \partial_x a(x) + \tilde{g}[a^\dagger(0)\sigma + a(0)\sigma^\dagger], \qquad (D3)$$

with $\tilde{g} = \sqrt{2}g$. In the odd-scattering channel, the photons do not interact with atoms at all, $H_{\text{odd}} = -ic \int dx a_0^\dagger(x) \partial_x a_0(x)$, and the problem is trivial. We now focus on the scattering problem in the even channel.

The single-excited eigenstates of Eq. (D1) can be written as the following superposition of the states with one photon and the states with zero photons and atoms excited to a symmetric Dicke state:

$$|k\rangle = \int dx E(x) a^\dagger(x)|0\rangle + P\sigma^\dagger|0\rangle. \qquad (D4)$$

The Schrödinger equation reads

$$-ic\partial_x E + \tilde{g}\delta(x)P = \varepsilon E,$$
$$N\tilde{g}E(0) = \varepsilon P \qquad (D5)$$

and has eigenstates with the energy $\varepsilon = ck$ and

$$E_k(x) = \theta(-x)e^{ikx} + \theta(x)t_k^{\text{even}}e^{ikx}, \qquad (D6)$$

where $t_k^{\mathrm{even}} = (ck - iN\gamma_{1D})/(ck + iN\gamma_{1D})$ is the transmission coefficient in the even channel and $\gamma_{1D} = \tilde{g}^2/2c \equiv g^2/c$ is the radiative decay rate. We note that the reflection and transmission coefficients for one atom can be given as $r = (1 - t_k^{\mathrm{even}})/2$ and $t = (1 + t_k^{\mathrm{even}})/2$ when $\varepsilon = \omega - \omega_0$ is taken into account. The eigenstate (D4) can be written in a compact way as

$$|k\rangle = \int dx\, r_k^\dagger(x)|0\rangle, \qquad r_k^\dagger(x) \equiv E_k(x)a^\dagger(x) + P\delta(x)\sigma^\dagger. \tag{D7}$$

We now proceed to the double-excited states having the energy 2ε and described by the *Ansatz*

$$\iint dx\,dy\, E(x,y)a^\dagger(x)a^\dagger(y)|0\rangle + \int dx\, P(x)a^\dagger(x)\sigma^\dagger|0\rangle$$
$$+ \frac{Q}{2}\sum_{j\neq j'}\sigma_j^\dagger\sigma_{j'}^\dagger|0\rangle, \tag{D8}$$

which is equivalent to Eq. (C2). The last term in Eq. (D8) accounts for the double-excited atomic array and is present only for $N > 1$. Instead of Eqs. (D5), we obtain

$$-i(\partial_x + \partial_y)E + \frac{\tilde{g}}{2}[\delta(x)P(y) + \delta(y)P(x)] = 2\varepsilon E,$$
$$-i\partial_x P + N\tilde{g}[E(x,0) + E(0,x)] + (N-1)\tilde{g}\delta(x)Q = 2\varepsilon P,$$
$$2\tilde{g}P = 2\varepsilon Q. \tag{D9}$$

In Eq. (D9) we assume the bosonic symmetry $E(x,y) = E(y,x)$ and also define the electric field at the singular lines $x = 0$ or $y = 0$ as

$$\frac{E(x,0^+) + E(x,0^-)}{2} \equiv \lim_{\delta\to 0}\frac{E(x,-\delta) + E(x,+\delta)}{2}.$$

The essence of the Bethe *Ansatz* approach is the representation of the amplitude $E(x,y)$ as a sum of free-space plane wave solutions outside the singular lines where $x = 0$ or $y = 0$,

$$E(x,y) = \begin{cases} Ae^{ikx+ipy} + Be^{iky+ipx}, & \text{region I,} \\ At_k^{\mathrm{even}}e^{ikx+ipy} + Bt_p^{\mathrm{even}}e^{iky+ipx}, & \text{region II,} \\ t_k^{\mathrm{even}}t_p^{\mathrm{even}}(Ae^{ikx+ipy} + Be^{iky+ipx}), & \text{region III,} \end{cases} \tag{D10}$$

where regions I–III are as indicated in Fig. 32. The states (D9) have the energy $2\varepsilon = c(k + p)$. The amplitude $P(x)$ is found using the first of Eqs. (D9) to be

$$P(x) = \frac{2i}{\tilde{g}} \times \begin{cases} E(x,0^+) - E(x,0^-), & x < 0, \\ E(0^+,x) - E(0^-,x), & x > 0. \end{cases} \tag{D11}$$

The second and third of Eqs. (D9) yield the continuity condition
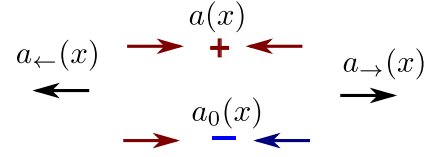

FIG. 31. Schematics of the separation in Eq. (D2) of the problem with left- and right-propagating photons into two problems with even and odd symmetry.

$$P(0^+) - P(0^-) = -\frac{i(N-1)\tilde{g}^2}{2\varepsilon}[P(0^+) + P(0^-)]. \tag{D12}$$

From Eqs. (D12) and (D11), we find the following relationship between the amplitudes A and B:

$$\frac{A}{B} = -\frac{i\tilde{g}^2 + ck - cp}{i\tilde{g}^2 - ck + cp}. \tag{D13}$$

Taking into account that $E(x,y) = E(y,x)$, we rewrite the amplitude in the region where $x,y < 0$ as

$$E(x,y) = \theta(x-y)[Ae^{ikx+ipy} + Be^{iky+ipx}]$$
$$+ \theta(y-x)[Ae^{iky+ipx} + Be^{ikx+ipy}]$$
$$= \frac{A+B}{2}e^{ikx+ipy}\left(1 + \mathrm{sgn}(x-y)\frac{A-B}{A+B}\right) + (k \leftrightarrow p). \tag{D14}$$

Since $(A - B)/(A + B) = i\tilde{g}^2/(ck - cp)$, the eigenstate (D8) can be presented in the following form:

$$|k,p\rangle = C\iint dx\,dy\left(1 + \frac{i(\tilde{g}^2/c)\mathrm{sgn}(x-y)}{k-p}\right)$$
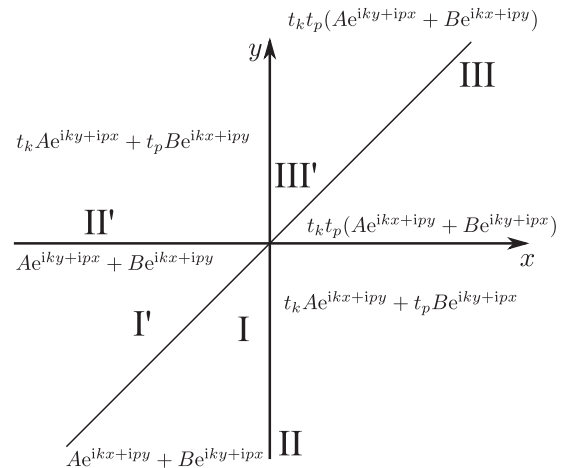$$\times r_k^\dagger(x)r_p^\dagger(y)|0\rangle, \tag{D15}$$

FIG. 32. Illustration of the Bethe *Ansatz* (D10) for the two-photon states depending on the first and second coordinates x and y. Region I corresponds to the incident state. In regions II and II' either the first or second photon is scattered on the atom. In regions III and III' both photons have scattered.
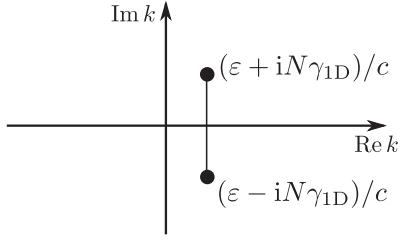
FIG. 33. Illustration of the so-called string between two rapidities, describing the bound two-photon state (D17) in the Bethe *Ansatz.*

FIG. 34. Integration contours for the rapidities k_1 and k_2 used to calculate the two-photon scattering problem in Eq. (D19).

where C is the normalization factor. The factorization of Eq. (D15) in products of single-excited eigenstates $r_k^\dagger(x) r_p^\dagger(x)|0\rangle$ is the central result of this appendix and means that the problem is solvable using the Bethe *Ansatz*. In the Bethe *Ansatz* formalism, the wave vectors k and p are called rapidities (Tsvelick and Wiegmann, 1983). For two-photon states with real-valued energies $2\varepsilon = c(k + p)$, the rapidities either can both real or can correspond to complex conjugated pairs $k = p^*$ that are called strings; see Fig. 33. Of special interest are the strings

$$k = \frac{\varepsilon + iN\gamma_{1D}}{c}, \qquad p = \frac{\varepsilon - iN\gamma_{1D}}{c}, \qquad (D16)$$

which correspond to the bound two-photon states. Specifically, if k and p are given by Eqs. (D16), we determine from Eq. (D13) that $B = 0$ and the two-photon state (D10) is then simplified as

$$E(x, y) = e^{i\varepsilon(x+y)/c} e^{-N|x-y|\gamma_{1D}/c} \times \begin{cases} 1, & x, y < 0, \\ t_k, & x, y < 0, \\ t_k t_p, & x, y > 0. \end{cases} \quad (D17)$$

The wave function amplitude for the bound state decays exponentially with an increase in the distance between the two photons $|x - y|$.

Rupasov and Yudson (1984) proved that the Bethe *Ansatz* holds for an arbitrary number of excitations $M = 1, 2, 3, \ldots$; i.e., the quantum Dicke problem is integrable. The eigenstate characterized by the so-called rapidities $k_1 \cdots k_M$ has the form

$$|\boldsymbol{k}\rangle = C \iint d^M x \prod_{m<n} \left(1 + \frac{i\tilde{g}^2 \mathrm{sgn}(x_m - x_n)}{c(k_m - k_n)}\right) \prod_{n=1}^{M} r_{k_n}^\dagger(x_n)|0\rangle \quad (D18)$$

with the energy $\varepsilon = c\sum_{m=1}^{M} k_m$.

To solve a scattering problem, when M photons are incident at the atoms from the left ($x \to -\infty$), one more step is required. Namely, the incident photon wave function has to be expanded over the Bethe eigenstates. This can be done in two ways. One is the "brute-force" approach, when the input eigenstate is presented as a superposition of the states (D15) with real rapidities k and p and the bound state (D17). Shen and Fan (2007b) proved that this set is complete and
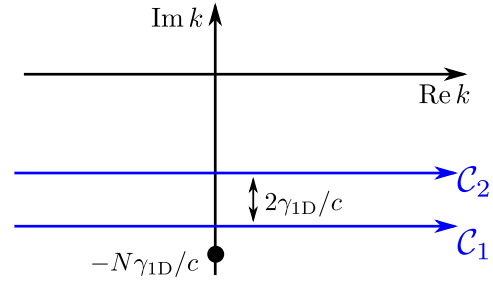
allows one to find the full scattering matrix of the problem. To perform this expansion, the eigenstates (D15) and (D17) have to be properly normalized.

There is an alternative approach that circumvents the expansion of the input state over the Bethe eigenstates and directly provides the scattered eigenstate (Yudson, 1985). Its particular application to the two-photon scattering problem was discussed in detail by Yudson and Reineker (2008). The two-photon amplitude is expressed as

$$E(x_1, x_2, t) = \int_{\mathcal{C}_1} \frac{dk_1}{2\pi} \int_{\mathcal{C}_2} \frac{dk_2}{2\pi} \left(1 - \frac{2i(\tilde{g}^2/c)\theta(x_2 - x_1)}{k_1 - k_2 + i\tilde{g}^2/c}\right)$$
$$\times e^{ik_1(x_1 - x_1^{(0)} - ct)} e^{ik_2(x_2 - x_2^{(0)} - ct)} E_{k_1}(x_1) E_{k_2}(x_2), \quad (D19)$$

where the integration over the rapidities k_1 and k_2 is performed along the contours $\mathcal{C}_1$ and $\mathcal{C}_2$ in the complex plane shown in Fig. 34. In Eq. (D19) $x_2^{(0)} < x_1^{(0)} < 0$ are the coordinates of two incident photons at $t = 0$ when the input state is $a^\dagger(x_1^{(0)})a^\dagger(x_2^{(0)})|0\rangle$. The advantage of the approach in Eq. (D19) is that it can be generalized for an arbitrary number of incident photons. To this end, the integration contours should satisfy the relation (Yudson and Reineker, 2008)

$$\mathrm{Im}\, k_{n+1} - \mathrm{Im}\, k_n > \frac{2\gamma_{1D}}{c}, \qquad \mathrm{Im}\, k_1 > -\frac{N\gamma_{1D}}{c}. \quad (D20)$$

Performing the integration in Eq. (D19), we obtain

$$E(x_1, x_2, t) = \Phi(x_1, x_1^{(0)} + ct)\Phi(x_2, x_2^{(0)} + ct)$$
$$+ \Phi_c(x_1, x_2, x_1^{(0)} + ct, x_2^{(0)} + ct). \quad (D21)$$

In Eq. (D21)

$$\Phi(x, x^{(0)} + ct) = \delta(x - x^{(0)} - ct)$$
$$- 2\gamma_{1D}N\theta(0 < x < x^{(0)} + ct)e^{\gamma_{1D}N(x - x^{(0)} - ct)} \quad (D22)$$

is the solution of the scattering problem for the input state $a^\dagger(x^{(0)})|0\rangle$ with one photon at $t = 0$. Hence, the first term in Eq. (D21) describes the independent scattering of two photons on the array of atoms. The second term describes the interaction between the photons and reads

$$\Phi_c(x_1, x_2, x_1^{(0)} + ct, x_2^{(0)} + ct)$$
$$= -\frac{2N\tilde{g}^4}{c^2}\theta(0 < x_1 < x_2 < x_2^{(0)} + ct < x_1^{(0)} + ct)$$
$$\times e^{N\gamma_{1D}(x_1 + x_2 - x_1^{(0)} - x_2^{(0)} - 2ct)}$$
$$\times [N - (N-1)e^{2\gamma_{1D}(x_2^{(0)} + ct - x_2)}]. \qquad (D23)$$

In Eq. (23) the notation $\theta(0 < x_1 < x_2 < \cdots)$ represents the product of the corresponding Heaviside step functions that is unity if $0 < x_1 < x_2$, and zero otherwise. The second term in square brackets in Eq. (D23) describes the contribution of photon scattering by an atomic system already excited to the Dicke state $b^\dagger|0\rangle$. This term is absent for the single-atom case when $N = 1$.

The scattering of two photons with certain incident energies ck_1 and ck_2 ($ck_1 + ck_2 = 2\varepsilon$) can be considered by performing a Fourier transform of Eq. (D23). We write the input state as

$$|\text{in}\rangle = \iint dx_1^{(0)} dx_2^{(0)} \theta(x_2^{(0)} < x_1^{(0)}) e^{ik_1 x_1^{(0)} + ik_2 x_2^{(0)}}$$
$$\times a_\rightarrow^\dagger(x_1^{(0)}) a_\rightarrow^\dagger(x_2^{(0)})|0\rangle + (k_1 \leftrightarrow k_2).$$

The scattered state is obtained by separating the odd- and even-scattering channels and applying Eq. (D23) in the even channel; see Fig. 31 and Eq. (D2). The scattered state for $x_2, x_1 > 0$ (the transmission channel) can be presented as

$$|\text{out}\rangle = \iint dx_1 dx_2 t(x_1, x_2) a^\dagger(x_1^{(0)}) a^\dagger(x_2^{(0)})|0\rangle, \qquad (D24)$$

where

$$t(x_1, x_2) = t(x_2, x_1)$$
$$= \frac{1}{2}[e^{ik_1 x_1 + k_2 x_2} + (k_1 \leftrightarrow k_2)]t_N(ck_1)t_N(ck_2)$$
$$+ \frac{1}{8}\int_{x_2}^\infty dx_2^{(0)} \int_{x_2^{(0)}}^\infty dx_1^{(0)} \Phi_c(x_1, x_2, x_1^{(0)}, x_2^{(0)})$$
$$\times [e^{ik_1 x_1^{(0)} + ik_2 x_2^{(0)}} + (k_1 \leftrightarrow k_2)], \qquad (D25)$$

and

$$t_N(ck) = \frac{1 + t_k^{\text{even}}}{2} = \frac{-ck}{ck + iN\gamma_{1D}}$$

is the transmission coefficient through N atoms [equivalent to Eqs. (28)]. The first part of Eq. (D25) describes the independent transmission of two photons, and the second part results from their interaction with each other. The prefactor $1/8$ comes from the conversion from the symmetric to the chiral problem and back ($\propto 1/2^2$) and also from the symmetrization of the transmission amplitude with respect to the permutations of x_1 and x_2. Performing the integration, we obtain (Yudson and Reineker, 2008)

$$t(x_1, x_2)$$
$$= \frac{1}{2}[e^{ik_1 x_1 + k_2 x_2} + (k_1 \leftrightarrow k_2)]t_N(ck_1)t_N(ck_2)$$
$$+ e^{i\varepsilon(x_1 + x_2)} \frac{N\varepsilon\gamma_{1D}^2 e^{(i\varepsilon - N\gamma_{1D})|x_1 - x_2|/c}}{[\varepsilon + i(N-1)\gamma_{1D}](ck_1 + iN\gamma_{1D})(ck_2 + iN\gamma_{1D})}. \qquad (D26)$$

Finally, the transmitted state for two incident photons having incident energies $\omega_{1,2} = ck_{1,2}$ is given by

$$|\text{out}\rangle = \frac{1}{2}\int \frac{d\omega_1' d\omega_2'}{(2\pi)^2} S(\omega_1', \omega_2' \leftarrow \omega_1, \omega_2) a_{\omega_1'/c}^\dagger a_{\omega_2'/c}^\dagger|0\rangle,$$

where

$$S(\omega_1', \omega_2' \leftarrow \omega_1, \omega_2)$$
$$= (2\pi)^2[\delta(\omega_1 - \omega_1')\delta(\omega_2 - \omega_2') + (\omega_1 \leftrightarrow \omega_2)]t_N(\omega_1)t_N(\omega_2)$$
$$+ 2\pi i M(\omega_1', \omega_2' \leftarrow \omega_1, \omega_2)\delta(\omega_1 + \omega_2 - \omega_1' - \omega_2'), \qquad (D27)$$

$$M(\omega_1', \omega_2' \leftarrow \omega_1, \omega_2) = 4\gamma_{1D}^2 s(\omega_1)s(\omega_2)s(\omega_1')s(\omega_2')$$
$$\times \frac{N(\varepsilon - \omega_0)(\varepsilon - \omega_0 + iN\gamma_{1D})}{\varepsilon - \omega_0 + i(N-1)\gamma_{1D}}, \qquad (D28)$$

and $s(\omega) = 1/(\omega - \omega_0 + iN\gamma_{1D})$. Here we have restored the atomic resonance frequency ω_0 to underline the resonant character of the scattering and introduced the frequencies of the scattered photons $\omega_{1,2}'$.

APPENDIX E: FUNCTIONAL INTEGRAL APPROACH

Here we show how the photonic degree of freedom can be integrated out to obtain the effective non-Hermitian Hamiltonian for the atomic system (Shi and Sun, 2009; Xu and Fan, 2015). We start with the full Lagrangian of the system $L = L_{\text{atoms}} + L_{\text{phot}} + L_{\text{atom-phot}}$, where

$$L_{\text{phot}} = \sum_k \left(ia_k^\dagger \frac{da_k}{dt} - \omega_k a_k^\dagger a_k\right),$$

$$L_{\text{atom-phot}} = -\frac{g}{\sqrt{L}}\sum_k \sum_{j=1}^N (a_k b_j^\dagger e^{ikz_j} + a_k^\dagger b_j e^{-ikz_j}), \qquad (E1)$$

and $L_{\text{atoms}} = i\sum_j b_j^\dagger(db_j/dt) - H_{\text{atoms}}$ is the Lagrangian of the atoms that depends on b_j and $b_j^\dagger$ only. The Green's functions of the atomic subsystem can be described by the generating functional, which is readily given by the functional integral

$$Z[\zeta_1^*(t), \ldots, \zeta_N^*(t); \zeta_1(t), \ldots, \zeta_N(t)]$$
$$= \int e^{i\int[L + \sum_j(\zeta_j^* b_j + \zeta_j b_j^\dagger)]dt} \prod_j D[b_j]D[b_j^\dagger]\prod_k D[a_k]D[a_k^\dagger]. \qquad (E2)$$

In particular, the single-excitation Green's function is given by the functional derivative

$$G_{jl}(t,t') = -\frac{\delta^2 \ln Z}{\delta \zeta_j^*(t)\delta \zeta_l(t')}\bigg|_{\zeta,\zeta^*=0}. \qquad (E3)$$

We now perform integration over $D[a_k]$ and $D[a_k^\dagger]$ in Eq. (E2). To this end, we separate the part that depends on the photonic operators and switch from temporal representation to the frequency domain, i.e., from $a_k(t)$ and $a_k^\dagger(t)$ to their Fourier transforms $a_k(\omega)$ and $a_k^\dagger(\omega)$:

$$\int (L_{\text{phot}} + L_{\text{atom-phot}})dt$$
$$= \sum_k \int \{(\omega - \omega_k)a_k^\dagger(\omega)a_k(\omega)$$
$$- g\sum_j [a_k(\omega)b_j^\dagger(\omega)e^{ikz_j} + a_k^\dagger(\omega)b_j(\omega)e^{-ikz_j}]\}d\omega.$$

The previous expression is quadratic in $a_k(\omega)$ and $a_k^\dagger(\omega)$. Therefore, the corresponding functional integral is Gaussian and can be easily evaluated,

$$\int e^{i\int (L_{\text{phot}}+L_{\text{atom-phot}})dt}\prod_k D[a_k]D[a_k^\dagger] = Ce^{i\delta S}, \qquad (E4)$$

where C is a constant and

$$\delta S = -\int d\omega \sum_k \frac{g^2}{\omega - \omega_k + i0}\sum_{j,l} b_j^\dagger b_l e^{ik(z_j-z_l)}. \qquad (E5)$$

Calculating the sum over k separately for $k > 0$ and $k < 0$, we obtain

$$\delta S = i\gamma_{1D}\int d\omega \sum_{j,l} b_j^\dagger(\omega)b_l(\omega)e^{i\omega|z_j-z_l|/c}, \qquad (E6)$$

where $\gamma_{1D} = g^2/c \equiv \Gamma_{1D}/2$.

Returning to the generating functional equation (E2), we can now present it in the following form:

$$Z = \int e^{i\int[L_{\text{atoms}}^{\text{eff}}+\sum_j(\zeta_j^* b_j + \zeta_j b_j^\dagger)]dt}\prod_j D[b_j]D[b_j^\dagger], \qquad (E7)$$

where $\int L_{\text{atoms}}^{\text{eff}}dt = \int L_{\text{atoms}}dt + \delta S$ is the effective action of the atomic system that accounts for photon-mediated interatomic interactions. Equivalently, we can introduce the effective Hamiltonian $\int L_{\text{atoms}}^{\text{eff}}dt = i\sum_j b_j^\dagger(db_j/dt) - H_{\text{atoms}}^{\text{eff}}(t)$, where

$$H_{\text{atoms}}^{\text{eff}}(t) = H_{\text{atoms}}(t) - i\gamma_{1D}\sum_{j,l} b_j^\dagger(t)b_l(t - |z_j - z_l|/c) \qquad (E8)$$

and $H_{\text{atoms}}(t) = \omega_0\sum_j b_j^\dagger(t)b_j(t)$. We note the two key features of the effective atomic Hamiltonian: it is non-Hermitian and non-Markovian. In the case of excitation by monochromatic light at frequency ω, we can use $b_l(t - \tau) = b_l e^{-i\omega\tau}$. The effective Hamiltonian then assumes the form

$$H_{\text{atoms}}^{\text{eff}} = \sum_{j,l} H_{jl}(\omega)b_j^\dagger b_l, \qquad (E9)$$

where the matrix

$$H_{jl}(\omega) = \omega_0\delta_{jl} - i\gamma_{1D}e^{i\omega|z_j-z_l|/c} \qquad (E10)$$

agrees with Eq. (15).

APPENDIX F: PHOTON PAIR SCATTERING: THE GREEN'S FUNCTION SOLUTION IN AN ELECTRON REPRESENTATION

Here we show how the two-photon scattering matrix for a single two-level atom (qubit) can be calculated using the Green's function technique. We first introduce the bare (disregarding the light-qubit interaction) Green's function of the qubit in its ground and excited states,

$$G_{0,g(x)}(\varepsilon) = \frac{1}{\varepsilon - \varepsilon_{g(e)} + i0}, \qquad (F1)$$

where $\varepsilon_{g(e)}$ is the energy of the qubit's ground (excited) state, $\varepsilon_e - \varepsilon_g = \omega_0$. The Green's function of the waveguide photon with the wave vector k reads

$$D_k(\omega) = \frac{1}{\omega - \omega_k + i0}, \qquad (F2)$$

where $\omega_k = c|k|$ is the photon dispersion.

The interaction with light does not affect the ground state of the qubit, since it cannot emit a photon, while the excited state gets dressed. The dressing occurs due to the processes when the qubit in the excited state emits a photon and then reabsorbs it, as depicted in Fig. 35(a). There the solid lines denote the Green's functions of the qubit in its ground or excited state, and wavy lines stand for the photon's Green's function. The vertex represents the process of photon absorption or emission by the atom and corresponds to the amplitude $g_k/\sqrt{L}$, where g_k is the interaction constant and L is the normalization length. The excited state self-energy corresponding to Fig. 35(a) reads

$$\Sigma(\varepsilon) = -i\sum_k \int \frac{d\varepsilon'}{2\pi}\left(\frac{ig_k}{\sqrt{L}}\right)^2 G_{0,g}(\varepsilon')D_k(\varepsilon - \varepsilon') \qquad (F3)$$

$$= -i\int \frac{dk}{2\pi}\frac{g_k^2}{\varepsilon - \varepsilon_g - \omega_k + i0}. \qquad (F4)$$

We separate the real and imaginary parts of Σ using the Sochocki formula ($\Sigma = \Sigma' + i\Sigma''$),

$$\Sigma'(\varepsilon) = \mathcal{P}\int \frac{dk}{2\pi}\frac{g_k^2}{\varepsilon - \varepsilon_g - \omega_k}, \qquad (F5)$$

$$\Sigma''(\varepsilon) = -\int \frac{dk}{2\pi}g_k^2\pi\delta(\varepsilon - \varepsilon_g - \omega_k) = -\frac{g_{k_0}^2}{v_{k_0}} = -\gamma_{1D}. \qquad (F6)$$

In Eq. (F6) the real part Σ' describes the radiative correction to the energy of the excited state (the Lamb shift), while the imaginary part Σ'' corresponds to the lifetime of the excited state, as previously calculated. Note that if we ignore the dependence of g_k on k and linearize the photon dispersion near

(a)

$$\Sigma(\varepsilon) = \underset{\varepsilon \quad g_k \qquad g_k \quad \varepsilon}{\overset{D_k(\varepsilon - \varepsilon') \quad G_{0,g}(\varepsilon')}{}}$$

(b)

$$\omega_k \quad \varepsilon_g + \omega_k \quad \omega_k$$
$$\varepsilon_g \quad |g\rangle \quad x \quad |g\rangle$$

(c)

$$\omega_{k_1'} \quad x \quad |g\rangle$$
$$\omega_{k_2'} \quad x \quad |g\rangle \quad \omega_{k_1}$$
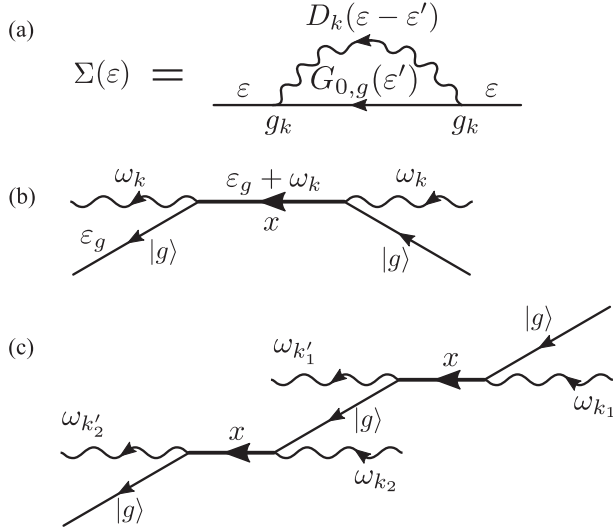$$\omega_{k_2}$$
$$|g\rangle$$

FIG. 35. (a) Diagrammatic representation of the self-energy correction for the excited atomic state. The straight line is the bare Green's function of the atom, while the wavy line is the photon's Green's function. (b) Diagram representing the single-photon reflection from an atom. The bold straight line represents the dressed Green's function of the atom in the excited state. (c) Diagrammatic representation of the two-photon scattering by an atom.

$k_0 = \omega_0/c$ and $\omega_k \approx \omega_{k_0} + v(k - k_0)$, the Σ' part vanishes, while Σ'' is constant.

The dressed Green's function of the excited state is readily expressed via the self-energy Σ as

$$G_e(\varepsilon) = \frac{1}{G_{0,e}^{-1}(\varepsilon) - \Sigma(\varepsilon)} = \frac{1}{\varepsilon - \varepsilon_0 + i\gamma_{1D}}. \qquad (F7)$$

The single-photon reflection coefficient is shown in Fig. 35 (b), where the bold line denotes the dressed Green's function of the excited state, which yields

$$r(\omega_k) = -i\gamma_{1D}G_e(\varepsilon_g + \omega_k) = -\frac{i\gamma_{1D}}{\omega_k - \omega_0 + i\gamma_{1D}}. \qquad (F8)$$

A diagram describing the simultaneous reflection of two photons is shown in Fig. 35(c). The scattering occurs at fourth order in the interaction constant. The higher-order contributions are easily taken into account using the dressed Green's function of the atom in the excited state (the bold solid line). The scattering matrix element corresponding to the diagram reads

$$S_1 = -\frac{ig^4}{L^2} G_e(\varepsilon_g + \omega_{k_1})G_{0,g}(\varepsilon_g + \omega_{k_1} - \omega_{k_1'})iG_e(\varepsilon_g + \omega_{k_2})$$
$$\times 2\pi\delta(\omega_{k_1} + \omega_{k_2} - \omega_{k_1'} - \omega_{k_2'})$$
$$= \frac{-ig^4/L^2}{(\omega_{k_1} - \omega_0 + i\gamma_{1D})(\omega_{k_1} - \omega_{k_1'} + i0)(\omega_{k_2} - \omega_0 + i\gamma_{1D})}$$
$$\times 2\pi\delta(\omega_{k_1} + \omega_{k_2} - \omega_{k_1'} - \omega_{k_2'}), \qquad (F9)$$

where we assume that g_k is k independent, $g_k = g$. Using the Sochocki formula, we decompose the result into two terms,

$$S_1 = S_1^{(coh)} + S_1^{(incoh)}, \qquad (F10)$$

$$S_1^{(coh)} = \frac{-g^4/L^2}{(\omega_{k_1} - \omega_0 + i\gamma_{1D})(\omega_{k_2'} - \omega_0 + i\gamma_{1D})}\pi\delta(\omega_{k_1} - \omega_{k_1'}),$$
$$\times 2\pi\delta(\omega_{k_1} + \omega_{k_2} - \omega_{k_1'} - \omega_{k_2'})$$
$$= \frac{1}{2}r(\omega_{k_1})r(\omega_{k_2})\delta_{|k_1|,|k_1'|}\delta_{|k_2|,|k_2'|}, \qquad (F11)$$

$$S_1^{(incoh)} = \frac{-ig^4/L^2}{(\omega_{k_1} - \omega_0 + i\gamma_{1D})(\omega_{k_2'} - \omega_0 + i\gamma_{1D})(\omega_{k_1} - \omega_{k_1'})}$$
$$\times 2\pi\delta(\omega_{k_1} + \omega_{k_2} - \omega_{k_1'} - \omega_{k_2'}). \qquad (F12)$$

$S_1^{(coh)}$ describes the process where photons are reflected independently, each of them conserving its frequency. The amplitude of this process is given by the product of the single-photon reflection coefficients $r(\omega)$ for the two photons. In contrast, $S_1^{(incoh)}$ describes the process where the photons interact and the energy is redistributed between them.

Apart from the contribution S_1, the scattering matrix features three more,

$$S = S_1 + S_2 + S_3 + S_4, \qquad (F13)$$

that are obtained by permutations: S_2 by $k_1 \leftrightarrow k_2$, S_3 by $k_1' \leftrightarrow k_2'$, and S_4 by both $k_1 \leftrightarrow k_2$ and $k_1' \leftrightarrow k_2'$. The calculation yields for the coherent term

$$S^{(coh)} = r(\omega_{k_1})r(\omega_{k_2})[\delta_{|k_1|,|k_1'|}\delta_{|k_2|,|k_2'|} + \delta_{|k_1|,|k_2'|}\delta_{|k_2|,|k_1'|}]. \qquad (F14)$$

For the incoherent term, after somewhat cumbersome algebra we obtain

$$S^{(incoh)} = \frac{2ig^4}{L^2}\frac{\omega_{k_1} + \omega_{k_2} - 2\omega_0 + 2i\gamma_{1D}}{(\omega_{k_1} - \omega_0 + i\gamma_{1D})(\omega_{k_2} - \omega_0 + i\gamma_{1D})}$$
$$\times \frac{2\pi\delta(w_1 + w_2 - w_1' - w_2')}{(\omega_{k_1'} - \omega_0 + i\gamma_{1D})(\omega_{k_2'} - \omega_0 + i\gamma_{1D})}. \qquad (F15)$$

The previous results for the two-photon scattering matrix for a single atom coincide with those obtained by other methods. However, this approach does not allow a direct generalization to the case of many atoms (Kocabaş, 2016).

APPENDIX G: PHOTON PAIR SCATTERING: THE GREEN'S FUNCTION SOLUTION IN AN EXCITON REPRESENTATION

Here we describe the Green's function technique for calculation of the scattering matrix of an atomic array that is based on excitonic representation of the atomic Hamiltonian in Eq. (A1). We start with the bare Green's functions of the atomic excitations and waveguide photons,

$$G_0(\omega) = \frac{1}{\omega - \omega_0 + i0}, \qquad (G1)$$

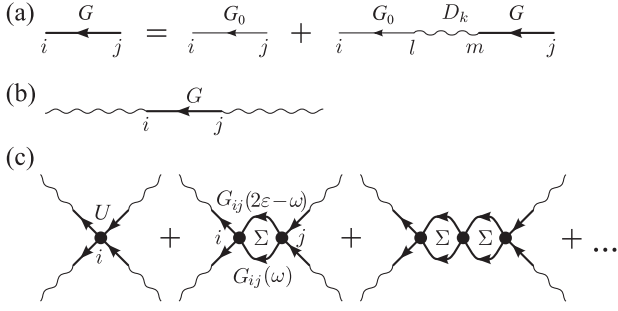$$D_k(\omega) = \frac{1}{\omega - \omega_k + i0}. \qquad (G2)$$

FIG. 36. (a) Dyson-like equation for the dressed exciton Green's function (thick straight line). The thin straight and wavy lines represent bare exciton and bare photon Green's functions. (b) Diagram representing single-photon reflection. (c) Series corresponding to the two-photon scattering. The bold dots indicate the exciton-exciton interaction U.

As in the approach taken in Appendix F, we start by dressing the atomic excitations by photons. The dressed exciton Green's function $G_{ij}(\omega)$ can be calculated from the Dyson-like equation depicted in Fig. 36(a), which yields

$$G_{ij}(\omega) = G_{0,ij}(\omega)$$
$$+ \frac{1}{L}\sum_k g_k^2 \sum_{l,m} G_{0,il}(\omega)e^{ikz_l}D_k(\omega)e^{-ikz_m}G_{mj}(\omega).$$

$$(G3)$$

Summation over k can be easily performed, assuming the linear dispersion $\omega_k = c|k|$ and constant $g_k = g$,

$$\frac{1}{L}\sum_k \frac{g_k^2 e^{ik(z_l - z_m)}}{\omega - \omega_k + i0} = -i\frac{g^2}{c}e^{i\omega|z_l - z_m|/c}. \quad (G4)$$

See also Eq. (C7). Equation (G3) then assumes the form

$$(\omega - \omega_0)G_{ij}(\omega) + i\gamma_{1D}\sum_m e^{i(\omega/c)|z_i - z_m|}G_{mj}(\omega) = \delta_{ij}, \quad (G5)$$

where $\gamma_{1D} = g^2/c$. In other words, the exciton Green's function can be found by inverting the matrix as

$$[G^{-1}(\omega)]_{ij} = (\omega - \omega_0)\delta_{ij} + i\gamma_{1D}e^{i(\omega/c)|z_i - z_j|}. \quad (G6)$$

The amplitude of the photon reflection from the left is shown in Fig. 36(b). It reads

$$r = -i\gamma_{1D}\sum_{ij} G_{ij}e^{i(\omega/c)(z_j + z_i)}, \quad (G7)$$

where we replace the $2\pi\delta(0)$ term with the time $T = L/c$. The result can be simplified by the use of the relations following from Eq. (G5),

$$s_i^+(\omega) \equiv \sum_j G_{ij}e^{i(\omega/c)z_j}$$
$$= \frac{e^{i(\omega/c)z_{\min}}}{i\gamma_{1D}}[\delta_{i,i_{\min}} - (\omega - \omega_0)G_{i,i_{\min}}], \quad (G8)$$

$$s_i^-(\omega) \equiv \sum_j G_{ij}e^{-i(\omega/c)z_j}$$
$$= \frac{e^{-i(\omega/c)z_{\max}}}{i\gamma_{1D}}[\delta_{i,i_{\max}} - (\omega - \omega_0)G_{i,i_{\max}}], \quad (G9)$$

where $i_{\max(\min)}$ are the indices of the atoms with the maximal (minimal) z-coordinate value $z_{\max}$ ($z_{\min}$). We then obtain

$$r = \frac{e^{2i(\omega/c)z_{\min}}}{i\gamma_{1D}}[(\omega - \omega_0 - i\gamma_{1D}) - (\omega - \omega_0)^2 G_{i_{\min},i_{\min}}]. \quad (G10)$$

A similar calculation gives the transmission coefficient

$$t = 1 - i\gamma_{1D}\sum_{ij} G_{ij}e^{i(\omega/c)(z_j - z_i)}$$
$$= \frac{(\omega - \omega_0)}{i\gamma_{1D}}[\delta_{i_{\max},i_{\min}} - (\omega - \omega_0)G_{i_{\max},i_{\min}}]. \quad (G11)$$

Diagrams corresponding to the two-photon scattering are shown in Fig. 36(c). There bold solid lines represent the exciton Green's function and the dots stand for the exciton-exciton interaction with the amplitude U. The scattering matrix element is given by the geometric series (Poshakinskiy and Poddubny, 2016)

$$S^{\text{incoh}}(\omega_1', \omega_2'; \omega_1, \omega_2)$$
$$= \frac{2g^4}{L^2}\sum_{i,j=1}^{N} s_i^-(\omega_1')s_i^-(\omega_2')[-iU\delta_{ij} + U^2\Sigma_{ij} + \cdots]$$
$$\times s_j^+(\omega_1)s_j^+(\omega_2)2\pi\delta(\omega_1 + \omega_2 - \omega_1' - \omega_2')$$
$$= 2\pi i M\left(\frac{c}{L}\right)^2 \delta(\omega_1 + \omega_2 - \omega_1' - \omega_2'),$$

where $s_i^\pm(\omega)$ is defined by Eqs. (G8) and (G9),

$$M = -2i\frac{g^4}{c^2}\sum_{i,j=1}^{N} s_i^-(\omega_1')s_i^-(\omega_2')Q_{ij}s_j^+(\omega_1)s_j^+(\omega_2) \quad (G12)$$

is the two-exciton self-energy, and the matrix Q is given by $Q = -iU(1 - iU\Sigma)^{-1}$, and the matrix Σ has the elements

$$\Sigma_{ij}(\varepsilon) = \int G_{ij}(\omega)G_{ij}(2\varepsilon - \omega)\frac{d\omega}{2\pi}, \quad (G13)$$

with $\varepsilon = (\omega_1 + \omega_2)/2$. In the case of a two-level atom $U \to \infty$, we get $Q = \Sigma^{-1}$.

It is instructive to compare the resonances of the scattering matrix Σ with the eigenstates of the two-photon Schrödinger equation. To this end, we substitute the double-excited states in the form $\sum_{m,n=1}^{N}\psi_{mn}b_m^\dagger b_n^\dagger|0\rangle$ into the effective Hamiltonian

$$H_{\text{atoms}} = \sum_{mn} H_{mn}b_m^\dagger b_n + \frac{U}{2}\sum_{m=1}^{N} b_m^\dagger b_m(b_m^\dagger b_m - 1), \quad (G14)$$

with H_{mn} given by Eq. (15) evaluated at $\omega = \omega_0$, and obtain (Ke *et al.*, 2019)

$$\sum_{m'n'=1}^{N} (\mathcal{H} + \mathcal{U})_{mn,m'n'} \psi_{m'n'} = 2\varepsilon \psi_{mn}, \qquad (G15)$$

with $\mathcal{H}_{mn;m'n'} = \delta_{mm'} H_{nn'} + \delta_{nn'} H_{mm'}$ and $\mathcal{U}_{mn,m'n'} = \delta_{mn}\delta_{mm'}\delta_{nn'} U$. We now note that the integral in Eq. (G13) can be presented as

$$\int \frac{d\omega}{2\pi} G_{ij}(\omega) G_{kl}(2\varepsilon - \omega) = \int \frac{d\omega}{2\pi} \left[\frac{1}{H - \omega}\right]_{ij} \left[\frac{1}{H + \omega - 2\varepsilon}\right]_{kl}$$
$$= \left[\frac{i}{H \otimes 1 + 1 \otimes H - 2\varepsilon}\right]_{ik,jl}. \qquad (G16)$$

Hence,

$$\Sigma_{mn} = \left[\frac{i}{\mathcal{H} - 2\varepsilon}\right]_{mm,nn}, \qquad Q_{mn} = iU\left[\frac{2\varepsilon - \mathcal{H}}{\mathcal{H} + \mathcal{U} - 2\varepsilon}\right]_{mm,nn}. \qquad (G17)$$

Thus, the two-photon scattering matrix indeed has resonances when the sum of the energies of two incident photons 2ε matches the energy of the double-excited state (G15). In the limit of $U \to \infty$ Eq. (G17) can be further simplified to

$$Q_{mn} = 2(i\varepsilon - \gamma_{1D})\delta_{mn} + \sum_{\nu=1}^{N(N-1)/2} \frac{2i d_m^\nu d_n^\nu}{\varepsilon_\nu - \varepsilon}, \qquad (G18)$$

where ε_ν are the two-photon state energies found in Eq. (G15) and $d_m^\nu = \mathcal{H}_{mm;m'n'}\psi_{m'n'}^\nu$, with the normalization condition for two-photon states being $\sum_{m'n'}(\psi_{m'n'}^\nu)^2 = 1$.

APPENDIX H: GENERATION OF THE GHZ STATE AND THE QUANTUM STATE TRANSFER

In this appendix, we provide more details on the protocols of the generation of the GHZ state and the quantum state transfer, which were proposed by Guimond *et al.* (2020) and illustrated in Fig. 19. The proposed quantum protocol works in the regime in which the interaction of a waveguide photon through a given dimer is described by the operator

$$|\text{phot}\rangle \to [|1_q\rangle\langle 1_q| - |0_q\rangle\langle 0_q|]|\text{phot}\rangle \equiv -\sigma_{z,q}|\text{phot}\rangle, \qquad (H1)$$

where $|0_q/1_q\rangle$ are the ground and excited states of the stationary qubit coupled to the dimer. This can be realized by choosing the energy of the incoming photon between the bare dimer qubit resonance and the dimer qubit resonance shifted by the excitation with the stationary qubit (Guimond *et al.*, 2020). We also introduce the Hadamard states of the stationary qubits and photons

$$|\pm\rangle = (|1\rangle \pm |0\rangle)/\sqrt{2}.$$

In the Hadamard basis, the photon transmission is described by the Pauli matrix σ_x, which corresponds to transitions $|+\rangle \to |-\rangle$ and $|-\rangle \to |+\rangle$.

The Hadamard gate acting on the qubit n is defined as $\hat{\mathcal{H}}_n = |+\rangle_n\langle 0|_n + |-\rangle_n\langle 1|_n$. The photons in the upper and lower waveguides shown in Fig. 19 play the role of flying qubits. The waveguides can be linked by beam splitters that act as Hadamard gates for the photons. The only difference is that the basis of the states $|0\rangle$ and $|1\rangle$ is replaced by $|d\rangle$ and $|u\rangle$, which correspond to the photons in the upper and lower waveguides. Specifically, a photon entering the lower arm is transformed into $(|d\rangle + |u\rangle)/\sqrt{2}$, and a photon entering the lower arm is transformed into $(|d\rangle - |u\rangle)/\sqrt{2}$.

We now illustrate the protocol to generate the GHZ state for the simplest case of $N = 2$ qubits. The system is initialized as $\psi_{\text{in}} = |+\rangle_1|+\rangle_2|d\rangle$; i.e., the stationary qubits are in the product state and one photon is incident in the lower waveguide. The cascaded photon processing in the array is detailed as follows:

First beam splitter: $\quad |+\rangle_1|+\rangle_2 \dfrac{|d\rangle + |u\rangle}{\sqrt{2}},$

after qubit 1: $\quad \dfrac{1}{\sqrt{2}}|-\rangle_1|+\rangle_2|u\rangle + \dfrac{1}{\sqrt{2}}|+\rangle_1|+\rangle_2|d\rangle,$

after qubit 2: $\quad \dfrac{1}{\sqrt{2}}|-\rangle_1|-\rangle_2|u\rangle + \dfrac{1}{\sqrt{2}}|+\rangle_1|+\rangle_2|d\rangle,$

Second beam splitter: $\quad \frac{1}{2}|d\rangle(|+\rangle_1|+\rangle_2 - |-\rangle_1|-\rangle_2)$
$$+ \tfrac{1}{2}|u\rangle(|+\rangle_1|+\rangle_2 + |-\rangle_1|-\rangle_2). \quad (H2)$$

Hence, after projecting the output on the state $|d\rangle$ or $|u\rangle$ (performing the measuring), one arrives at the qubit array in the GHZ state.

A similar approach can be used for the quantum state transfer; see Fig. 19(b). We start with the first qubit in an arbitrary quantum state and one photon in the lower waveguide,

$$\psi_{\text{in}} = (c_+|+\rangle_1 + c_-|-\rangle_1)|+\rangle_2|d\rangle, \qquad (H3)$$

with $|c_+|^2 + |c_-|^2 = 1$. Using the previous logic, we find that the output state after the third beam splitter is

$$|\psi_1\rangle = -\frac{\sqrt{2}}{4}\{[(c_+ + c_-)|-\rangle_2 + (c_+ - c_-)|+\rangle_2]|-\rangle_1$$
$$+ [(c_+ + c_-)|-\rangle_2 - (c_+ - c_-)|+\rangle_2]|+\rangle_1\}|d\rangle + (\cdots)|u\rangle.$$

We now start to perform the quantum measurements. We project the state $|\psi_1\rangle$ onto the state $|d\rangle$, apply the $\sigma_{z,1}$ matrix, and project the first qubit in the $|-\rangle_1$ state:

$$\psi_2 = \langle d|\langle -|_1\sigma_{z,1}|\psi_1\rangle = -\frac{\sqrt{2}}{4}[(c_- + c_+)|-\rangle_2 + (c_+ - c_-)|+\rangle_2].$$

We now apply the Hadamard transformation followed by the $\sigma_{z,2}$ operation to the second qubit:

$$2\sigma_z\hat{\mathcal{H}}\psi_2 = c_+|+\rangle_2 + c_-|-\rangle_2.$$

Thus, the quantum state has been transferred to the second qubit.

The setup of Fig. 19 can be easily tailored to construct arbitrary matrix product states (10) of the stationary qubits, with the rank of the A matrix equal to 2. Even more complicated states could be generated by adding waveguides to the system (Guimond *et al.*, 2020).

APPENDIX I: PHOTON PAIR SCATTERING FROM A CHIRAL ATOMIC ARRAY

Here we generalize the technique discussed in Appendix G to the case of photon pair scattering from a chiral array of two-level atoms. The problem is still described by the Hamiltonians (A1)–(A4), but the summation over k is carried out only over the right-going photon states, where $k > 0$. The effective Hamiltonian describing a light-mediated interaction between single-excited atomic states is

$$H_{nm} = \begin{cases} \omega_0 - i(\gamma^{\rightarrow} + \gamma), & n = m, \\ -2i\gamma^{\rightarrow}, & n > m, \\ 0, & n < m, \end{cases} \quad (I1)$$

where $\gamma^{\rightarrow} = g^2/2c$ is the radiative decay rate of a single atom and γ is the nonradiative decay rate. This Hamiltonian is similar to the Hamiltonian (15) for a nonchiral waveguide, but now the atoms with $n < m$ are not coupled to each other by light.

The Green's function for single-excited states is given by $G = (\omega - H)^{-1}$. Since the atoms with $n < m$ are decoupled, the Green's function can be found recursively as

$$G_{11} = \frac{1}{\omega - \tilde{\omega}_0} \quad (I2)$$

($\tilde{\omega}_0 = \omega_0 - i\gamma^{\rightarrow} - i\gamma$) and

$$G_{nm} = G_{11} + 2i\gamma^{\rightarrow} \sum_{m'=0}^{n-1} G_{nm'}, \quad G_{nm} = 0 \quad \text{for } m > n. \quad (I3)$$

Using Eqs. (G13), we now find the two-photon scattering kernel

$$\Sigma_{nm}(\varepsilon) \equiv \int G_{nm}(\omega) G_{nm}(2\varepsilon - \omega) \frac{d\omega}{2\pi} = \frac{i\gamma^{\rightarrow} \delta_{nm}}{\tilde{\omega}_0 - \varepsilon}. \quad (I4)$$

The scattering matrix is given by Eq. (G12) and reads

$$M(\omega, 2\varepsilon - \omega \leftarrow \varepsilon, \varepsilon)$$
$$= \frac{4g^2}{c} \frac{1}{(\varepsilon - \tilde{\omega}_0)(\omega - \tilde{\omega}_0)(2\varepsilon - \omega - \tilde{\omega}_0)} \frac{t_{\varepsilon}^{2N} t_{\omega}^{N} t_{2\varepsilon-\omega} - 1}{t_{\varepsilon}^{2} t_{\omega} t_{2\varepsilon-\omega} - 1}, \quad (I5)$$

where

$$t_{\omega} = \frac{\omega_0 - \omega + i\gamma^{\rightarrow} - i\gamma}{\omega_0 - \omega - i\gamma^{\rightarrow} - i\gamma} \quad (I6)$$

is the single-photon transmission coefficient of one atom. The photon-photon correlation function is found in Eq. (35) and is determined by the residue of Nth order at $\omega = \tilde{\omega}_0$, which can be calculated as

$$g_N^{(2)}(0) = \left(1 + \frac{d^{N-1}}{dx^{N-1}} \mathcal{M}|_{x=0}\right)^2, \quad (I7)$$

with

$$\mathcal{M} = \frac{(1 + \gamma^{\rightarrow}/\gamma)[(1 - x)(x - \gamma/\gamma^{\rightarrow})/(\gamma/\gamma^{\rightarrow} + 1 - x)]^N}{1/2 - (1/2 + \gamma/2\gamma^{\rightarrow} - x)^2 + (\gamma/\gamma^{\rightarrow})^2}. \quad (I8)$$

For relatively small values of $N \lesssim 100$, the residue can be readily calculated by expanding the products in Eq. (I8) in the binomial series (Mahmoodian *et al.*, 2018). For large values of $\gamma/\gamma^{\rightarrow}$, it is possible to use a simple asymptotic expression (62) that is valid for an arbitrarily large N. To derive this expression, we rewrite the residue in Eq. (I7) as a contour integral,

$$\frac{d^{N-1}}{dx^{N-1}} \mathcal{M}|_{x=0} = \frac{1}{2\pi i} \oint_{x=R} \mathcal{M} dx. \quad (I9)$$

For $\gamma \gg \gamma^{\rightarrow}$, the value of the integral is determined mostly by a simple pole at $x = x^*$, where

$$x^* = \frac{\gamma}{\gamma^{\rightarrow}} + \frac{1}{2} - \sqrt{2\left(\frac{\gamma}{\gamma^{\rightarrow}}\right)^2 + \frac{1}{2}} \quad (I10)$$

is a zero of the denominator that results in Eq. (62).

APPENDIX J: PHOTON REFLECTION FROM A PLANAR ATOMIC ARRAY

In this appendix, we outline the calculation of the light reflection from a two-dimensional atomic array that was considered in Sec. III.C. The light-array interaction can be treated in the following discrete dipole approximation (Draine and Flatau, 1994):

$$\boldsymbol{p}_j = \alpha\left[\boldsymbol{E}_0(\boldsymbol{r}_j) + \sum_{j' \neq j} G(\boldsymbol{r}_{j'} - \boldsymbol{r}_j)\boldsymbol{p}_{j'}\right], \quad (J1)$$

where $\boldsymbol{p}_j$ is the electric dipole moment of the atom number j and

$$\alpha = \frac{3ic^3}{2\omega_0^3} \frac{\gamma_0}{\omega_0 - \omega - i(\gamma_0 + \gamma)} \quad (J2)$$

is the single-atom polarizability characterized by the resonance frequency ω_0, a radiative decay rate $\gamma_0 \equiv \Gamma_0/2$, and a nonradiative decay rate $\gamma \equiv \Gamma/2$. In Eq. (J1) $\boldsymbol{E}_0$ is the electric field of the incident wave and

$$G_{\mu\nu}(\boldsymbol{r}, \omega) = \left[\delta_{\mu\nu} + \left(\frac{c}{\omega}\right)^2 \frac{\partial^2}{\partial x_\mu \partial x_\nu}\right] \frac{e^{i\omega r/c}}{4\pi r} \quad (J3)$$

is the electromagnetic tensor of the Green's function at the frequency ω satisfying the equation $\text{rot}\,\text{rot}\,G = (\omega/c)^2 G + \delta(\boldsymbol{r})$. The first term in Eq. (J1) describes the

polarizability of the atom by the incident wave, and the second term accounts for the sum of electric fields emitted by all other atoms. We consider for simplicity the case in which light is incident in the normal direction, such that $E_0(r_j) \equiv E_0$ and $p_j = p$. In this case Eq. (J1) is readily solved, yielding

$$p = \tilde{\alpha}E_0, \qquad \tilde{\alpha} = \frac{\alpha}{1 - C\alpha}, \tag{J4}$$

where

$$C = 4\pi \left(\frac{\omega}{c}\right)^2 \sum_{r \neq 0} G_{xx}(r) \tag{J5}$$

is the so-called interaction constant describing light-induced coupling between a given atom and all other atoms in the array. Hence, the coefficient $\tilde{\alpha}$ in Eq. (J4) is the polarizability renormalized by collective coupling between the atoms. The amplitude light reflection and transmission coefficients from the array r and t can be found by summing the field emitted from all the dipoles in the normal direction. The results read (Ivchenko, Fu, and Willander, 2000; Yugova *et al.*, 2009)

$$r = \frac{2\pi i\omega}{ca^2}\tilde{\alpha}, \qquad t = 1 + r. \tag{J6}$$

We consider an array with $a < \lambda$ when all the diffracted waves are evanescent. In this case, the reflection and transmission coefficients reduce to Eqs. (64).

The sum in Eq. (J5) for arrays with tens of atoms, which occurs in practice (Rui *et al.*, 2020), can be readily and directly evaluated. In the theoretical limit of an infinite array the convergence of the sum is slow due to far-field interactions. The commonly used approach to evaluate the lattice sum is the Ewald summation, which is based on splitting the sum into two parts. The first part corresponding to smaller values of r in the near-field zone is evaluated in real space, and the second part corresponding to the far-field zone $r \gtrsim c/\omega$ is Fourier transformed into reciprocal space using the identity

$$\frac{e^{i\omega r/c}}{r} = \sum_b \frac{2\pi i}{k_b a^2} e^{ik_b|z| + ib \cdot \rho}, \tag{J7}$$

where $r = (r, z)$ and the reciprocal lattice vectors b form a square lattice with the spacing $2\pi/a$ and $k_b \equiv \sqrt{(\omega/c)^2 - b^2}$. More details on the Ewald summation were given by Kambe (1967). Another efficient summation technique, which in our experience is even more efficient, is the Floquet summation technique developed by Belov and Simovski (2005). Specifically, the sum is given as Eq. (A37) by Belov and Simovski (2005), which has to be complex conjugated and also multiplied by 4π to take into account the time dependence convention $e^{j\omega t}$ and the differing definition of the Green's function by Belov and Simovski (2005).

We now discuss how to obtain the approximate expression for the lattice constant given by Eq. (66). The first term $2\pi i\omega/ca^2$ is given by the term with $b = 0$ in Eq. (J7) multiplied by $(\omega/c)^2$. It describes the radiative decay due to the emission of the waves propagating normally to the array,

where $b = 0$, or, in another words, results from far-field radiative coupling between the atoms. The term $S/2$ is given by the near field and can be obtained by setting ω in Eq. (J5) to zero:

$$\frac{S}{2} = \sum_{r \neq 0} \frac{\partial^2}{\partial x^2} \frac{1}{r} \equiv \sum_{r \neq 0} \frac{3x^2 - r^2}{r^5}$$
$$= \frac{1}{2} \sum \sum_{r \neq 0} \frac{1}{r^3} \approx \frac{9.03}{2a^3}. \tag{J8}$$

The sum for the square lattice converges rapidly enough and can be calculated directly. The term $S'(\omega/c)^2/2$ resulting from the field in Eq. (J5) in the intermediate zone between the far field and the near field reads

$$\frac{S'(\omega/c)^2}{2} = \sum_{r \neq 0} \frac{1 - (x/r)^2}{r} \frac{e^{ib \cdot r + i\omega r/c}}{r}. \tag{J9}$$

The term $1 - (x/r)^2$ for the square lattice can be replaced by $1/2$, and we can write it as

$$S' = \lim_{z \to 0} \lim_{\omega \to 0} \left(\text{Re} \sum_r \frac{e^{i\omega\sqrt{r^2 + z^2}/c}}{\sqrt{r^2 + z^2}} - \frac{e^{i\omega|z|/c}}{|z|} \right). \tag{J10}$$

Taking the Fourier transformation of the first term with the help of Eq. (J7), we find that

$$S' = \lim_{z \to 0} \lim_{\omega \to 0} \left(\frac{2\pi i}{a} \sum_b \frac{e^{i\sqrt{(\omega/c)^2 - b^2}|z|}}{\sqrt{(\omega/c)^2 - b^2}} - \frac{e^{i\omega|z|/c}}{|z|} \right)$$
$$= \lim_{z \to 0} \left(\frac{2\pi}{a} \sum_b \frac{e^{-b|z|}}{b} - \frac{1}{|z|} \right). \tag{J11}$$

We first check the cancellation of the singular diverging terms $\propto 1/z$ in Eq. (J11). To do this, we can replace the summation by integration:

$$\frac{2\pi}{a} \sum_b \frac{e^{-bz}}{b} \approx \int_0^\infty b\,db \frac{e^{-b|z|}}{b} = \frac{1}{|z|}. \tag{J12}$$

Thus, the $1/z$ terms cancel each other out and Eq. (J11) has a finite limit of the order of $1/a$. Numerical calculation for a square lattice yields

$$S' = \lim_{z \to 0} \left(\frac{2\pi}{a} \sum_b \frac{e^{-b|z|}}{b} - \frac{1}{|z|} \right) = -\frac{3.90}{a}. \tag{J13}$$

REFERENCES

Ahmed, S., C. Sánchez Muñoz, F. Nori, and A. F. Kockum, 2021, "Classification and reconstruction of optical quantum states with deep neural networks," Phys. Rev. Res. **3**, 033278.

Aiello, A., P. Banzer, M. Neugebauer, and G. Leuchs, 2015, "From transverse angular momentum to photonic wheels," Nat. Photonics **9**, 789–795.

Alaee, R., B. Gurlek, M. Albooyeh, D. Martín-Cano, and V. Sandoghdar, 2020, "Quantum Metamaterials with Magnetic Response at Optical Frequencies," Phys. Rev. Lett. **125**, 063601.

Alaee, R., A. Safari, V. Sandoghdar, and R. W. Boyd, 2020, "Kerker effect, superscattering, and scattering dark states in atomic antennas," Phys. Rev. Res. **2**, 043409.

Albrecht, A., L. Henriet, A. Asenjo-Garcia, P. B. Dieterle, O. Painter, and D. E. Chang, 2019, "Subradiant states of quantum bits coupled to a one-dimensional waveguide," New J. Phys. **21**, 025003.

Andrei, N., 1980, "Diagonalization of the Kondo Hamiltonian," Phys. Rev. Lett. **45**, 379–382.

Andreoli, F., M. J. Gullans, A. A. High, A. Browaeys, and D. E. Chang, 2021, "Maximum Refractive Index of an Atomic Medium," Phys. Rev. X **11**, 011026.

Aoki, T., A. S. Parkins, D. J. Alton, C. A. Regal, B. Dayan, E. Ostby, K. J. Vahala, and H. J. Kimble, 2009, "Efficient Routing of Single Photons by One Atom and a Microtoroidal Cavity," Phys. Rev. Lett. **102**, 083601.

Arcari, M., *et al.*, 2014, "Near-Unity Coupling Efficiency of a Quantum Emitter to a Photonic Crystal Waveguide," Phys. Rev. Lett. **113**, 093603.

Arranz Regidor, S., G. Crowder, H. Carmichael, and S. Hughes, 2021, "Modeling quantum light-matter interactions in waveguide QED with retardation, nonlinear interactions, and a time-delayed feedback: Matrix product states versus a space-discretized waveguide model," Phys. Rev. Res. **3**, 023030.

Asenjo-Garcia, A., J. D. Hood, D. E. Chang, and H. J. Kimble, 2017, "Atom-light interactions in quasi-one-dimensional nanostructures: A Green's-function perspective," Phys. Rev. A **95**, 033818.

Asenjo-Garcia, A., M. Moreno-Cardoner, A. Albrecht, H. J. Kimble, and D. E. Chang, 2017, "Exponential Improvement in Photon Storage Fidelities Using Subradiance and 'Selective Radiance' in Atomic Arrays," Phys. Rev. X **7**, 031024gb.

Ashida, Y., A. İmamoğlu, and E. Demler, 2022, "Nonperturbative waveguide quantum electrodynamics," Phys. Rev. Res. **4**, 023194.

Ashida, Y., A. İmamoğlu, J. Faist, D. Jaksch, A. Cavalleri, and E. Demler, 2020, "Quantum Electrodynamic Control of Matter: Cavity-Enhanced Ferroelectric Phase Transition," Phys. Rev. X **10**, 041027.

Astafiev, O., A. M. Zagoskin, A. A. Abdumalikov, Y. A. Pashkin, T. Yamamoto, K. Inomata, Y. Nakamura, and J. S. Tsai, 2010, "Resonance fluorescence of a single artificial atom," Science **327**, 840–843.

Astafiev, O. V., A. A. Abdumalikov, A. M. Zagoskin, Y. A. Pashkin, Y. Nakamura, and J. S. Tsai, 2010, "Ultimate On-Chip Quantum Amplifier," Phys. Rev. Lett. **104**, 183603.

Ballantine, K. E., and J. Ruostekoski, 2020a, "Optical Magnetism and Huygens' Surfaces in Arrays of Atoms Induced by Cooperative Responses," Phys. Rev. Lett. **125**, 143604.

Ballantine, K. E., and J. Ruostekoski, 2020b, "Radiative Toroidal Dipole and Anapole Excitations in Collectively Responding Arrays of Atoms," Phys. Rev. Lett. **125**, 063201.

Ballantine, K. E., and J. Ruostekoski, 2020c, "Subradiance-protected excitation spreading in the generation of collimated photon emission from an atomic array," Phys. Rev. Res. **2**, 023086.

Barends, R., *et al.*, 2013, "Coherent Josephson Qubit Suitable for Scalable Quantum Integrated Circuits," Phys. Rev. Lett. **111**, 080502.

Barik, S., A. Karasahin, C. Flower, T. Cai, H. Miyake, W. DeGottardi, M. Hafezi, and E. Waks, 2018, "A topological quantum optics interface," Science **359**, 666–668.

Barik, S., A. Karasahin, S. Mittal, E. Waks, and M. Hafezi, 2020, "Chiral quantum optics using a topological resonator," Phys. Rev. B **101**, 205303.

Barredo, D., S. de Léséleuc, V. Lienhard, T. Lahaye, and A. Browaeys, 2016, "An atom-by-atom assembler of defect-free arbitrary two-dimensional atomic arrays," Science **354**, 1021–1023.

Batchelor, M. T., 2007, "The Bethe ansatz after 75 years," Phys. Today **60**, No. 1, 36–40.

Becker, J. N., and C. Becher, 2017, "Coherence properties and quantum control of silicon vacancy color centers in diamond," Phys. Status Solidi (a) **214**, 1700586.

Béguin, J.-B., J. Laurat, X. Luan, A. P. Burgers, Z. Qin, and H. J. Kimble, 2020, "Reduced volume and reflection for bright optical tweezers with radial Laguerre-Gauss beams," Proc. Natl. Acad. Sci. U.S.A. **117**, 26109–26117.

Bekenstein, R., I. Pikovski, H. Pichler, E. Shahmoon, S. F. Yelin, and M. D. Lukin, 2020, "Quantum metasurfaces with atom arrays," Nat. Phys. **16**, 676–681.

Bello, M., G. Platero, J. I. Cirac, and A. González-Tudela, 2019, "Unconventional quantum optics in topological waveguide QED," Sci. Adv. **5**, eaaw0297.

Belov, P. A., and C. R. Simovski, 2005, "Homogenization of electromagnetic crystals formed by uniaxial resonant scatterers," Phys. Rev. E **72**, 026615.

Belyansky, R., S. Whitsitt, R. Lundgren, Y. Wang, A. Vrajitoarea, A. A. Houck, and A. V. Gorshkov, 2021, "Frustration-induced anomalous transport and strong photon decay in waveguide QED," Phys. Rev. Res. **3**, L032058.

Benedict, M. G., A. M. Ermolaev, V. Malyshev, I. Sokolov, and E. D. Trifonov, 2018, *Super-radiance: Multiatomic Coherent Emission* (CRC Press, Boca Raton).

Bernevig, B., and T. Hughes, 2013, *Topological Insulators and Topological Superconductors* (Princeton University Press, Princeton, NJ).

Bettles, R. J., S. A. Gardiner, and C. S. Adams, 2016, "Enhanced Optical Cross Section via Collective Coupling of Atomic Dipoles in a 2D Array," Phys. Rev. Lett. **116**, 103602.

Bettles, R. J., M. D. Lee, S. A. Gardiner, and J. Ruostekoski, 2020, "Quantum and nonlinear effects in light transmitted through planar atomic arrays," Commun. Phys. **3**, 141.

Bettles, R. J., J. Minář, C. S. Adams, I. Lesanovsky, and B. Olmos, 2017, "Topological properties of a dense atomic lattice gas," Phys. Rev. A **96**, 041603.

Bhaskar, M., *et al.*, 2017, "Quantum Nonlinear Optics with a Germanium-Vacancy Color Center in a Nanoscale Diamond Waveguide," Phys. Rev. Lett. **118**, 223603.

Bilmes, A., A. Megrant, P. Klimov, G. Weiss, J. M. Martinis, A. V. Ustinov, and J. Lisenfeld, 2020, "Resolving the positions of defects in superconducting quantum bits," Sci. Rep. **10**, 3090.

Blais, A., A. L. Grimsmo, S. M. Girvin, and A. Wallraff, 2021, "Circuit quantum electrodynamics," Rev. Mod. Phys. **93**, 025005.

Bloch, I., J. Dalibard, and S. Nascimbène, 2012, "Quantum simulations with ultracold quantum gases," Nat. Phys. **8**, 267–276.

Blume, M., V. Emery, and A. Luther, 1970, "Spin-Boson Systems: One-Dimensional Equivalents and the Kondo Problem," Phys. Rev. Lett. **25**, 450.

Bothner, D., I. C. Rodrigues, and G. A. Steele, 2021, "Photon-pressure strong coupling between two superconducting circuits," Nat. Phys. **17**, 85.

Braak, D., 2011, "Integrability of the Rabi Model," Phys. Rev. Lett. **107**, 100401.

Brehm, J. D., A. N. Poddubny, A. Stehli, T. Wolz, H. Rotzinger, and A. V. Ustinov, 2021, "Waveguide bandgap engineering with an array of superconducting qubits," npj Quantum Mater. **6**, 10.

Burnett, J. J., A. Bengtsson, M. Scigliuzzo, D. Niepce, M. Kudra, P. Delsing, and J. Bylander, 2019, "Decoherence benchmarking of superconducting qubits," npj Quantum Inf. **5**, 54.

Calajó, G., and D. E. Chang, 2022, "Emergence of solitons from many-body photon bound states in quantum nonlinear media," Phys. Rev. Res. **4**, 023026.

Caneva, T., M. T. Manzoni, T. Shi, J. S. Douglas, J. I. Cirac, and D. E. Chang, 2015, "Quantum dynamics of propagating photons with strong interactions: A generalized input-output formalism," New J. Phys. **17**, 113001.

Carmichael, H. J., 1993, "Quantum Trajectory Theory for Cascaded Open Systems," Phys. Rev. Lett. **70**, 2273–2276.

Carollo, F., K. Brandner, and I. Lesanovsky, 2020, "Nonequilibrium Many-Body Quantum Engine Driven by Time-Translation Symmetry Breaking," Phys. Rev. Lett. **125**, 240602.

Carusotto, I., A. A. Houck, A. J. Kollár, P. Roushan, D. I. Schuster, and J. Simon, 2020, "Photonic materials in circuit quantum electrodynamics," Nat. Phys. **16**, 268–279.

Chang, D. E., J. I. Cirac, and H. J. Kimble, 2013, "Self-Organization of Atoms along a Nanophotonic Waveguide," Phys. Rev. Lett. **110**, 113606.

Chang, D. E., J. S. Douglas, A. González-Tudela, C.-L. Hung, and H. J. Kimble, 2018, "Colloquium: Quantum matter built from nanoscopic lattices of atoms and photons," Rev. Mod. Phys. **90**, 031002.

Chang, D. E., V. Vuletić, and M. D. Lukin, 2014, "Quantum non-linear optics—Photon by photon," Nat. Photonics **8**, 685–694.

Che, Y., C. Gneiting, T. Liu, and F. Nori, 2020, "Topological quantum phase transitions retrieved through unsupervised machine learning," Phys. Rev. B **102**, 134213.

Chumakov, A. I., G. V. Smirnov, A. Q. R. Baron, J. Arthur, D. E. Brown, S. L. Ruby, G. S. Brown, and N. N. Salashchenko, 1993, "Resonant Diffraction of Synchrotron Radiation by a Nuclear Multilayer," Phys. Rev. Lett. **71**, 2489–2492.

Coles, R. J., D. M. Price, J. E. Dixon, B. Royall, E. Clarke, P. Kok, M. S. Skolnick, A. M. Fox, and M. N. Makhonin, 2016, "Chirality of nanophotonic waveguide with embedded quantum emitter for unidirectional spin transfer," Nat. Commun. **7**, 11183.

Corzo, N. V., B. Gouraud, A. Chandra, A. Goban, A. S. Sheremet, D. V. Kupriyanov, and J. Laurat, 2016, "Large Bragg Reflection from One-Dimensional Chains of Trapped Atoms near a Nanoscale Waveguide," Phys. Rev. Lett. **117**, 133603.

Corzo, N. V., J. Raskop, A. Chandra, A. S. Sheremet, B. Gouraud, and J. Laurat, 2019, "Waveguide-coupled single collective excitation of atomic arrays," Nature (London) **566**, 359–362.

Das, S., V. E. Elfving, F. Reiter, and A. S. Sørensen, 2018, "Photon scattering from a system of multilevel quantum emitters. I. Formalism," Phys. Rev. A **97**, 043837.

Dayan, B., A. S. Parkins, T. Aoki, E. P. Ostby, K. J. Vahala, and H. J. Kimble, 2008, "A photon turnstile dynamically regulated by one atom," Science **319**, 1062–1065.

De Bernardis, D., Z.-P. Cian, I. Carusotto, M. Hafezi, and P. Rabl, 2021, "Light-Matter Interactions in Synthetic Magnetic Fields: Landau-Photon Polaritons," Phys. Rev. Lett. **126**, 103603.

Decker, M., N. Feth, C. M. Soukoulis, S. Linden, and M. Wegener, 2011, "Retarded long-range interaction in split-ring-resonator square arrays," Phys. Rev. B **84**, 085416.

Deutsch, I. H., R. J. C. Spreeuw, S. L. Rolston, and W. D. Phillips, 1995, "Photonic band gaps in optical lattices," Phys. Rev. A **52**, 1394–1410.

DeVoe, R. G., and R. G. Brewer, 1996, "Observation of Superradiant and Subradiant Spontaneous Emission of Two Trapped Ions," Phys. Rev. Lett. **76**, 2049–2052.

de Vries, P., D. V. van Coevorden, and A. Lagendijk, 1998, "Point scatterers for classical waves," Rev. Mod. Phys. **70**, 447–466.

Dicke, R. H., 1954, "Coherence in spontaneous radiation processes," Phys. Rev. **93**, 99.

Douglas, J. S., H. Habibian, C.-L. Hung, A. V. Gorshkov, H. J. Kimble, and D. E. Chang, 2015, "Quantum many-body models with cold atoms coupled to photonic crystals," Nat. Photonics **9**, 326–331.

Draine, B. T., and P. J. Flatau, 1994, "Discrete-dipole approximation for scattering calculations," J. Opt. Soc. Am. A **11**, 1491–1499.

Dreessen, C. L., C. Ouellet-Plamondon, P. Tighineanu, X. Zhou, L. Midolo, A. S. Sørensen, and P. Lodahl, 2018, "Suppressing phonon decoherence of high performance single-photon sources in nano-photonic waveguides," Quantum Sci. Technol. **4**, 015003.

Duan, L. M., M. D. Lukin, J. I. Cirac, and P. Zoller, 2001, "Long-distance quantum communication with atomic ensembles and linear optics," Nature (London) **414**, 413–418.

Ebadi, S., *et al.*, 2021, "Quantum phases of matter on a 256-atom programmable quantum simulator," Nature (London) **595**, 227–232.

Facchinetti, G., S. D. Jenkins, and J. Ruostekoski, 2016, "Storing Light with Subradiant Correlations in Arrays of Atoms," Phys. Rev. Lett. **117**, 243601.

Faddeev, L. D., 2013, "The new life of complete integrability," Phys. Usp. **56**, 465–472.

Faez, S., P. Türschmann, H. R. Haakh, S. Götzinger, and V. Sandoghdar, 2014, "Coherent Interaction of Light and Single Molecules in a Dielectric Nanoguide," Phys. Rev. Lett. **113**, 213601.

Fan, S., 2002, "Sharp asymmetric line shapes in side-coupled waveguide-cavity systems," Appl. Phys. Lett. **80**, 908.

Fang, Y.-L. L., F. Ciccarello, and H. U. Baranger, 2018, "Non-Markovian dynamics of a qubit due to single-photon scattering in a waveguide," New J. Phys. **20**, 043035.

Fang, Y.-L. L., H. Zheng, and H. U. Baranger, 2014, "One-dimensional waveguide coupled to multiple qubits: Photon-photon correlations," Eur. Phys. J. Quantum Technol. **1**, 3.

Fayard, N., L. Henriet, A. Asenjo-Garcia, and D. E. Chang, 2021, "Many-body localization in waveguide quantum electrodynamics," Phys. Rev. Res. **3**, 033233.

Fedorovich, G., D. Kornovan, A. Poddubny, and M. Petrov, 2022, "Chirality-driven delocalization in disordered waveguide-coupled quantum arrays," Phys. Rev. A **106**, 043723.

Figotin, A., and I. Vitebskiy, 2011, "Slow wave phenomena in photonic crystals," Laser Photonics Rev. **5**, 201–213.

Fiorelli, E., M. Marcuzzi, P. Rotondo, F. Carollo, and I. Lesanovsky, 2020, "Signatures of Associative Memory Behavior in a Multi-mode Dicke Model," Phys. Rev. Lett. **125**, 070604.

Fleischhauer, M., A. Imamoglu, and J. P. Marangos, 2005, "Electro-magnetically induced transparency: Optics in coherent media," Rev. Mod. Phys. **77**, 633–673.

Forn-Díaz, P., J. J. García-Ripoll, B. Peropadre, J.-L. Orgiazzi, M. Yurtalan, R. Belyansky, C. M. Wilson, and A. Lupascu, 2017, "Ultrastrong coupling of a single artificial atom to an electro-magnetic continuum in the nonperturbative regime," Nat. Phys. **13**, 39–43.

Foster, A. P., *et al.*, 2019, "Tunable Photon Statistics Exploiting the Fano Effect in a Waveguide," Phys. Rev. Lett. **122**, 173603.

Frisk Kockum, A., 2021, "Quantum optics with giant atoms—The first five years," in *International Symposium on Mathematics,*

Quantum Theory, and Cryptography, edited by T. Takagi, M. Wakayama, K. Tanaka, N. Kunihiro, K. Kimoto, and Y. Ikematsu (Springer, Singapore), pp. 125–146.

Frisk Kockum, A., P. Delsing, and G. Johansson, 2014, "Designing frequency-dependent relaxation rates and Lamb shifts for a giant artificial atom," Phys. Rev. A **90**, 013837.

Gardiner, C., and M. Collett, 1985, "Input and output in damped quantum systems: Quantum stochastic differential equations and the master equation," Phys. Rev. A **31**, 3761–3774.

Gardiner, C. W., 1993, "Driving a Quantum System with the Output Field from Another Driven Quantum System," Phys. Rev. Lett. **70**, 2269–2272.

Gheeraert, N., S. Kono, and Y. Nakamura, 2020, "Programmable directional emitter and receiver of itinerant microwave photons in a waveguide," Phys. Rev. A **102**, 053720.

Gippius, N. A., and S. G. Tikhodeev, 2009, "Application of the scattering matrix method for calculating the optical properties of metamaterials," Phys. Usp. **52**, 967–971.

Girardeau, M., 1960, "Relationship between systems of impenetrable bosons and fermions in one dimension," J. Math. Phys. (N.Y.) **1**, 516–523.

Gnutzmann, S., and U. Smilansky, 2006, "Quantum graphs: Applications to quantum chaos and universal spectral statistics," Adv. Phys. **55**, 527–625.

Goban, A., K. S. Choi, D. J. Alton, D. Ding, C. Lacroûte, M. Pototschnig, T. Thiele, N. P. Stern, and H. J. Kimble, 2012, "Demonstration of a State-Insensitive, Compensated Nanofiber Trap," Phys. Rev. Lett. **109**, 033603.

Goban, A., C.-L. Hung, J. Hood, S.-P. Yu, J. Muniz, O. Painter, and H. Kimble, 2015, "Superradiance for Atoms Trapped along a Photonic Crystal Waveguide," Phys. Rev. Lett. **115**, 063601.

Goban, A., *et al.*, 2014, "Atom-light interactions in photonic crystals," Nat. Commun. **5**, 3808.

Gonzalez-Tudela, A., D. Martin-Cano, E. Moreno, L. Martin-Moreno, C. Tejedor, and F. J. Garcia-Vidal, 2011, "Entanglement of Two Qubits Mediated by One-Dimensional Plasmonic Waveguides," Phys. Rev. Lett. **106**, 020501.

González-Tudela, A., and J. I. Cirac, 2018, "Exotic quantum dynamics and purely long-range coherent interactions in Dirac conelike baths," Phys. Rev. A **97**, 043831.

González-Tudela, A., C.-L. Hung, D. E. Chang, J. I. Cirac, and H. J. Kimble, 2015, "Subwavelength vacuum lattices and atom-atom interactions in two-dimensional photonic crystals," Nat. Photonics **9**, 320–325.

Gopalakrishnan, S., B. L. Lev, and P. M. Goldbart, 2011, "Frustration and Glassiness in Spin Models with Cavity-Mediated Interactions," Phys. Rev. Lett. **107**, 277201.

Gorshkov, A. V., A. André, M. Fleischhauer, A. S. Sørensen, and M. D. Lukin, 2007, "Universal Approach to Optimal Photon Storage in Atomic Media," Phys. Rev. Lett. **98**, 123601.

Gouraud, B., D. Maxein, A. Nicolas, O. Morin, and J. Laurat, 2015, "Demonstration of a Memory for Tightly Guided Light in an Optical Nanofiber," Phys. Rev. Lett. **114**, 180503.

Grankin, A., P. O. Guimond, D. V. Vasilyev, B. Vermersch, and P. Zoller, 2018, "Free-space photonic quantum link and chiral quantum optics," Phys. Rev. A **98**, 043825.

Greenberg, Y. S., A. A. Shtygashev, and A. G. Moiseev, 2021, "Waveguide band-gap *n*-qubit array with a tunable transparency resonance," Phys. Rev. A **103**, 023508.

Grimsmo, A. L., 2015, "Time-Delayed Quantum Feedback Control," Phys. Rev. Lett. **115**, 060402.

Grimsmo, A. L., B. Royer, J. M. Kreikebaum, Y. Ye, K. O'Brien, I. Siddiqi, and A. Blais, 2021, "Quantum Metamaterial for Broadband Detection of Single Microwave Photons," Phys. Rev. Appl. **15**, 034074.

Gross, M., and S. Haroche, 1982, "Superradiance: An essay on the theory of collective spontaneous emission," Phys. Rep. **93**, 301–396.

Gruner, T., and D.-G. Welsch, 1996, "Green-function approach to the radiation-field quantization for homogeneous and inhomogeneous Kramers-Kronig dielectrics," Phys. Rev. A **53**, 1818–1829.

Gu, X., A. F. Kockum, A. Miranowicz, Y. xi Liu, and F. Nori, 2017, "Microwave photonics with superconducting quantum circuits," Phys. Rep. **718–719**, 1–102.

Guerin, W., M. O. Araújo, and R. Kaiser, 2016, "Subradiance in a Large Cloud of Cold Atoms," Phys. Rev. Lett. **116**, 083601.

Guerin, W., M. Rouabah, and R. Kaiser, 2017, "Light interacting with atomic ensembles: Collective, cooperative and mesoscopic effects," J. Mod. Opt. **64**, 895–907.

Guimond, P.-O., A. Grankin, D. V. Vasilyev, B. Vermersch, and P. Zoller, 2019, "Subradiant Bell States in Distant Atomic Arrays," Phys. Rev. Lett. **122**, 093601.

Guimond, P.-O., B. Vermersch, M. L. Juan, A. Sharafiev, G. Kirchmair, and P. Zoller, 2020, "A unidirectional on-chip photonic interface for superconducting circuits," npj Quantum Inf. **6**, 32.

Guo, L., A. F. Kockum, F. Marquardt, and G. Johansson, 2020, "Oscillating bound states for a giant atom," Phys. Rev. Res. **2**, 043014.

Gustafsson, M. V., T. Aref, A. F. Kockum, M. K. Ekström, G. Johansson, and P. Delsing, 2014, "Propagating phonons coupled to an artificial atom," Science **346**, 207–211.

Haakh, H. R., S. Faez, and V. Sandoghdar, 2016, "Polaritonic normal-mode splitting and light localization in a one-dimensional nanoguide," Phys. Rev. A **94**, 053840.

Haber, J., J. Gollwitzer, S. Francoual, M. Tolkiehn, J. Strempfer, and R. Röhlsberger, 2019, "Spectral Control of an X-Ray *l*-Edge Transition via a Thin-Film Cavity," Phys. Rev. Lett. **122**, 123608.

Haber, J., X. Kong, C. Strohm, S. Willing, J. Gollwitzer, L. Bocklage, R. Rüffer, A. Pálffy, and R. Röhlsberger, 2017, "Rabi oscillations of x-ray radiation between two nuclear ensembles," Nat. Photonics **11**, 720–725.

Haber, J., *et al.*, 2016, "Collective strong coupling of x-rays and nuclei in a nuclear optical lattice," Nat. Photonics **10**, 445–449.

Hammerer, K., A. S. Sørensen, and E. S. Polzik, 2010, "Quantum interface between light and atomic ensembles," Rev. Mod. Phys. **82**, 1041–1093.

Hannon, J., and G. Trammell, 1999, "Coherent γ-ray optics," Hyperfine Interact. **123**, 127–274.

Hinney, J., A. S. Prasad, S. Mahmoodian, K. Hammerer, A. Rauschenbeutel, P. Schneeweiss, J. Volz, and M. Schemmer, 2021, "Unraveling Two-Photon Entanglement via the Squeezing Spectrum of Light Traveling through Nanofiber-Coupled Atoms," Phys. Rev. Lett. **127**, 123602.

Hoi, I.-C., A. F. Kockum, T. Palomaki, T. M. Stace, B. Fan, L. Tornberg, S. R. Sathyamoorthy, G. Johansson, P. Delsing, and C. M. Wilson, 2013, "Giant Cross–Kerr Effect for Propagating Microwaves Induced by an Artificial Atom," Phys. Rev. Lett. **111**, 053601.

Hoi, I.-C., T. Palomaki, J. Lindkvist, G. Johansson, P. Delsing, and C. M. Wilson, 2012, "Generation of Nonclassical Microwave States Using an Artificial Atom in 1D Open Space," Phys. Rev. Lett. **108**, 263601.

Hoi, I.-C., C. M. Wilson, G. Johansson, T. Palomaki, B. Peropadre, and P. Delsing, 2011, "Demonstration of a Single-Photon Router in the Microwave Regime," Phys. Rev. Lett. **107**, 073601.

Hopfield, J. J., 1982, "Neural networks and physical systems with emergent collective computational abilities," Proc. Natl. Acad. Sci. U.S.A. **79**, 2554–2558.

Hsu, C. W., B. Zhen, A. D. Stone, J. D. Joannopoulos, and M. Soljačić, 2016, "Bound states in the continuum," Nat. Rev. Mater. **1**, 16048.

Hung, C.-L., A. González-Tudela, J. I. Cirac, and H. J. Kimble, 2016, "Quantum spin dynamics with pairwise-tunable, long-range interactions," Proc. Natl. Acad. Sci. U.S.A. **113**, E4946–E4955.

Iorsh, I., A. Poshakinskiy, and A. Poddubny, 2020, "Waveguide Quantum Optomechanics: Parity-Time Phase Transitions in Ultrastrong Coupling Regime," Phys. Rev. Lett. **125**, 183601.

Ivchenko, E., A. Kavokin, V. Kochereshko, P. Kop'ev, and N. Ledentsov, 1992, "Exciton resonance reflection from quantum well, quantum wire and quantum dot structures," Superlattices Microstruct. **12**, 317–320.

Ivchenko, E. L., 1991, "Excitonic polaritons in periodic quantum-well structures," Sov. Phys. Solid State **33**, 1344–1346, https://www.mathnet.ru/php/archive.phtml?wshow=paper&jrnid=ftt&paperid=7009&option_lang=eng.

Ivchenko, E. L., 2005, *Optical Spectroscopy of Semiconductor Nanostructures* (Alpha Science International, Harrow, England).

Ivchenko, E. L., Y. Fu, and M. Willander, 2000, "Exciton polaritons in quantum-dot photonic crystals," Phys. Solid State **42**, 1756–1765.

Ivchenko, E. L., and A. V. Kavokin, 1992, "Light reflection from quantum well, quantum wire and quantum dot structures," Sov. Phys. Solid State **34**, 968–971, https://www.mathnet.ru/php/archive.phtml?wshow=paper&jrnid=ftt&paperid=7554&option_lang=en.

Ivchenko, E. L., A. I. Nesvizhskii, and S. Jorda, 1994a, "Resonant Bragg reflection from quantum-well structures," Superlattices Microstruct. **16**, 17–20.

Ivchenko, E. L., A. I. Nesvizhskii, and S. Jorda, 1994b, "Bragg reflection of light from quantum-well structures," Phys. Solid State **36**, 1156–1161, https://journals.ioffe.ru/articles/16569.

Iversen, O., and T. Pohl, 2021, "Strongly Correlated States of Light and Repulsive Photons in Chiral Chains of Three-Level Quantum Emitters," Phys. Rev. Lett. **126**, 083605, https://journals.ioffe.ru/articles/16569.

Iversen, O. A., and T. Pohl, 2022, "Self-ordering of individual photons in waveguide QED and Rydberg atom arrays," Phys. Rev. Res. **4**, 023002.

Jalali Mehrabad, M., A. P. Foster, R. Dost, E. Clarke, P. K. Patil, I. Farrer, J. Heffernan, M. S. Skolnick, and L. R. Wilson, 2020, "A semiconductor topological photonic ring resonator," Appl. Phys. Lett. **116**, 061102.

Javadi, A., *et al.*, 2018, "Spin-photon interface and spin-controlled photon switching in a nanobeam waveguide," Nat. Nanotechnol. **13**, 398–403.

Jen, H. H., 2020, "Disorder-assisted excitation localization in chirally coupled quantum emitters," Phys. Rev. A **102**, 043525.

Jen, H. H., 2021, "Bound and subradiant multiatom excitations in an atomic array with nonreciprocal couplings," Phys. Rev. A **103**, 063711.

Jones, R., G. Buonaiuto, B. Lang, I. Lesanovsky, and B. Olmos, 2020, "Collectively Enhanced Chiral Photon Emission from an Atomic Array near a Nanofiber," Phys. Rev. Lett. **124**, 093601.

Jung, P., A. V. Ustinov, and S. M. Anlage, 2014, "Progress in superconducting metamaterials," Supercond. Sci. Technol. **27**, 073001.

Kagan, Y., 1999, "Theory of coherent phenomena and fundamentals in nuclear resonant scattering," Hyperfine Interact. **123**, 83–126.

Kambe, K., 1967, "Theory of low-energy electron diffraction. I. Application of the cellular method of monatomic layers," Z. Naturforsch. Teil A **22**, 322.

Kannan, B., *et al.*, 2020, "Waveguide quantum electrodynamics with superconducting artificial giant atoms," Nature (London) **583**, 775–779.

Karg, T. M., B. Gouraud, C. T. Ngai, G.-L. Schmid, K. Hammerer, and P. Treutlein, 2020, "Light-mediated strong coupling between a mechanical oscillator and atomic spins 1 meter apart," Science **369**, 174–179.

Karg, T. M., B. Gouraud, P. Treutlein, and K. Hammerer, 2019, "Remote Hamiltonian interactions mediated by light," Phys. Rev. A **99**, 063829.

Kaur, K., T. Sépulcre, N. Roch, I. Snyman, S. Florens, and S. Bera, 2021, "Spin-Boson Quantum Phase Transition in Multilevel Superconducting Qubits," Phys. Rev. Lett. **127**, 237702.

Ke, Y., A. V. Poshakinskiy, C. Lee, Y. S. Kivshar, and A. N. Poddubny, 2019, "Inelastic Scattering of Photon Pairs in Qubit Arrays with Subradiant States," Phys. Rev. Lett. **123**, 253601.

Khanikaev, A. B., and G. Shvets, 2017, "Two-dimensional topological photonics," Nat. Photonics **11**, 763–773.

Khitrova, G., and H. M. Gibbs, 2007, "Quantum dots: Collective radiance," Nat. Phys. **3**, 84–86.

Kiilerich, A. H., and K. Mølmer, 2019, "Input-Output Theory with Quantum Pulses," Phys. Rev. Lett. **123**, 123604.

Kiilerich, A. H., and K. Mølmer, 2020, "Quantum interactions with pulses of radiation," Phys. Rev. A **102**, 023717.

Kim, E., X. Zhang, V. S. Ferreira, J. Banker, J. K. Iverson, A. Sipahigil, M. Bello, A. González-Tudela, M. Mirhosseini, and O. Painter, 2021, "Quantum Electrodynamics in a Topological Waveguide," Phys. Rev. X **11**, 011015.

Kivshar, Y., 2018, "All-dielectric meta-optics and non-linear nanophotonics," Natl. Sci. Rev. **5**, 144–158.

Kocabaş, Ş. E., 2016, "Effects of modal dispersion on few-photon–qubit scattering in one-dimensional waveguides," Phys. Rev. A **93**, 033829.

Koch, J., T. M. Yu, J. Gambetta, A. A. Houck, D. I. Schuster, J. Majer, A. Blais, M. H. Devoret, S. M. Girvin, and R. J. Schoelkopf, 2007, "Charge-insensitive qubit design derived from the Cooper pair box," Phys. Rev. A **76**, 042319.

Kockum, A. F., G. Johansson, and F. Nori, 2018, "Decoherence-Free Interaction between Giant Atoms in Waveguide Quantum Electrodynamics," Phys. Rev. Lett. **120**, 140404.

Kockum, A. F., A. Miranowicz, S. D. Liberato, S. Savasta, and F. Nori, 2019, "Ultrastrong coupling between light and matter," Nat. Rev. Phys. **1**, 19–40.

Kojima, K., H. F. Hofmann, S. Takeuchi, and K. Sasaki, 2003, "Nonlinear interaction of two photons with a one-dimensional atom: Spatiotemporal quantum coherence in the emitted field," Phys. Rev. A **68**, 013803.

Kornovan, D., R. Savelev, Y. Kivshar, and M. Petrov, 2021, "High-Q localized states in finite arrays of subwavelength resonators," ACS Photonics **8**, 3627–3632.

Kornovan, D. F., N. V. Corzo, J. Laurat, and A. S. Sheremet, 2019, "Extremely subradiant states in a periodic one-dimensional atomic array," Phys. Rev. A **100**, 063832.

Kornovan, D. F., A. S. Sheremet, and M. I. Petrov, 2016, "Collective polaritonic modes in an array of two-level quantum emitters coupled to an optical nanofiber," Phys. Rev. B **94**, 245416.

Koshelev, K., S. Kruk, E. Melik-Gaykazyan, J.-H. Choi, A. Bogdanov, H.-G. Park, and Y. Kivshar, 2020, "Subwavelength dielectric resonators for nonlinear nanophotonics," Science **367**, 288–292.

Koshino, K., and H. Ishihara, 2004, "Evaluation of Two-Photon Nonlinearity by a Semiclassical Method," Phys. Rev. Lett. **93**, 173601.

Kosobukin, V. A., 2003, "Exciton polaritons and their one-dimensional localization in disordered quantum-well structures," Phys. Solid State **45**, 1145–1153.

Kosobukin, V. A., and A. N. Poddubny, 2007, "Exciton-polariton absorption in periodic and disordered quantum-well chains," Phys. Solid State **49**, 1977–1987.

Kraus, Y. E., Y. Lahini, Z. Ringel, M. Verbin, and O. Zilberberg, 2012, "Topological States and Adiabatic Pumping in Quasicrystals," Phys. Rev. Lett. **109**, 106402.

Kuhlmann, A. V., J. H. Prechtel, J. Houel, A. Ludwig, D. Reuter, A. D. Wieck, and R. J. Warburton, 2015, "Transform-limited single photons from a single quantum dot," Nat. Commun. **6**, 8204.

Kuznetsov, A. I., A. E. Miroshnichenko, M. L. Brongersma, Y. S. Kivshar, and B. Luk'yanchuk, 2016, "Optically resonant dielectric nanostructures," Science **354**, 2472.

Kwon, J., Y. Kim, A. Lanuza, and D. Schneble, 2022, "Formation of matter-wave polaritons in an optical lattice," Nat. Phys. **18**, 657–661.

Laakso, M., and M. Pletyukhov, 2014, "Scattering of Two Photons from Two Distant Qubits: Exact Solution," Phys. Rev. Lett. **113**, 183601.

Lachance-Quirion, D., Y. Tabuchi, A. Gloppe, K. Usami, and Y. Nakamura, 2019, "Hybrid quantum systems based on magnonics," Appl. Phys. Express **12**, 070101.

Lalumière, K., B. C. Sanders, A. F. van Loo, A. Fedorov, A. Wallraff, and A. Blais, 2013, "Input-output theory for waveguide QED with an ensemble of inhomogeneous atoms," Phys. Rev. A **88**, 043806.

Lamprianidis, A. G., X. Zambrana-Puyalto, C. Rockstuhl, and I. Fernandez-Corbaton, 2022, "Directional coupling of emitters into waveguides: A symmetry perspective," Laser Photonics Rev. **16**, 2000516.

Lecocq, F., J. B. Clark, R. W. Simmonds, J. Aumentado, and J. D. Teufel, 2016, "Mechanically Mediated Microwave Frequency Conversion in the Quantum Regime," Phys. Rev. Lett. **116**, 043601.

Leggett, A. J., S. Chakravarty, A. T. Dorsey, M. P. A. Fisher, A. Garg, and W. Zwerger, 1987, "Dynamics of the dissipative two-state system," Rev. Mod. Phys. **59**, 1–85.

Le Hur, K., 2010, *Understanding Quantum Phase Transitions* (CRC Press, Boca Raton).

Le Jeannic, H., *et al.*, 2021, "Experimental Reconstruction of the Few-Photon Nonlinear Scattering Matrix from a Single Quantum Dot in a Nanophotonic Waveguide," Phys. Rev. Lett. **126**, 023603.

Le Kien, F., V. I. Balykin, and K. Hakuta, 2004, "Atom trap and waveguide using a two-color evanescent light field around a subwavelength-diameter optical fiber," Phys. Rev. A **70**, 063403.

Le Kien, F., S. Dutta Gupta, V. I. Balykin, and K. Hakuta, 2005, "Spontaneous emission of a cesium atom near a nanofiber: Efficient coupling of light to guided modes," Phys. Rev. A **72**, 032509.

Le Kien, F., and A. Rauschenbeutel, 2014, "Propagation of nanofiber-guided light through an array of atoms," Phys. Rev. A **90**, 063816.

Le Kien, F., and A. Rauschenbeutel, 2015, "Electromagnetically induced transparency for guided light in an atomic array outside an optical nanofiber," Phys. Rev. A **91**, 053847.

Lentrodt, D., K. P. Heeg, C. H. Keitel, and J. Evers, 2020, "*Ab initio* quantum models for thin-film x-ray cavity QED," Phys. Rev. Res. **2**, 023396.

Leonforte, L., A. Carollo, and F. Ciccarello, 2021, "Vacancy-like Dressed States in Topological Waveguide QED," Phys. Rev. Lett. **126**, 063601.

Leong, W. S., M. Xin, Z. Chen, S. Chai, Y. Wang, and S.-Y. Lan, 2020, "Large array of Schrödinger cat states facilitated by an optical waveguide," Nat. Commun. **11**, 5295.

Leung, P. M., and B. C. Sanders, 2012, "Coherent Control of Microwave Pulse Storage in Superconducting Circuits," Phys. Rev. Lett. **109**, 253603.

Liang, Y., and A. Czarnecki, 2012, "Photon-photon scattering: A tutorial," Can. J. Phys. **90**, 11.

Liao, J.-Q., and C. K. Law, 2010, "Correlated two-photon transport in a one-dimensional waveguide side-coupled to a nonlinear cavity," Phys. Rev. A **82**, 053836.

Lieb, E. H., and W. Liniger, 1963, "Exact analysis of an interacting Bose gas. I. The general solution and the ground state," Phys. Rev. **130**, 1605–1616.

Liu, F., *et al.*, 2018, "High Purcell factor generation of indistinguishable on-chip single photons," Nat. Nanotechnol. **13**, 835–840.

Lodahl, P., S. Mahmoodian, and S. Stobbe, 2015, "Interfacing single photons and single quantum dots with photonic nanostructures," Rev. Mod. Phys. **87**, 347.

Lodahl, P., S. Mahmoodian, S. Stobbe, A. Rauschenbeutel, P. Schneeweiss, J. Volz, H. Pichler, and P. Zoller, 2017, "Chiral quantum optics," Nature (London) **541**, 473–480.

Lodahl, P., A. F. Van Driel, I. S. Nikolaev, A. Irman, K. Overgaag, D. Vanmaekelbergh, and W. L. Vos, 2004, "Controlling the dynamics of spontaneous emission from quantum dots by photonic crystals," Nature (London) **430**, 654–657.

Mahan, G. D., and G. Obermair, 1969, "Polaritons at surfaces," Phys. Rev. **183**, 834–841.

Mahmoodian, S., 2019, "Chiral Light-Matter Interaction beyond the Rotating-Wave Approximation," Phys. Rev. Lett. **123**, 133603.

Mahmoodian, S., G. Calajó, D. E. Chang, K. Hammerer, and A. S. Sørensen, 2020, "Dynamics of Many-Body Photon Bound States in Chiral Waveguide QED," Phys. Rev. X **10**, 031011.

Mahmoodian, S., M. Čepulkovskis, S. Das, P. Lodahl, K. Hammerer, and A. S. Sørensen, 2018, "Strongly Correlated Photon Transport in Waveguide Quantum Electrodynamics with Weakly Coupled Emitters," Phys. Rev. Lett. **121**, 143601.

Malpuech, G., and A. Kavokin, 1999, "Absorption of light by inhomogeneously broadened excitons in quantum wells," Semicond. Sci. Technol. **14**, 1031–1033.

Manasi, P., and D. Roy, 2018, "Light propagation through one-dimensional interacting open quantum systems," Phys. Rev. A **98**, 023802.

Manzoni, M. T., L. Mathey, and D. E. Chang, 2017, "Designing exotic many-body states of atomic spin and motion in photonic crystals," Nat. Commun. **8**, 14696.

Manzoni, M. T., M. Moreno-Cardoner, A. Asenjo-Garcia, J. V. Porto, A. V. Gorshkov, and D. E. Chang, 2018, "Optimization of photon storage fidelity in ordered atomic arrays," New J. Phys. **20**, 083048.

Marques, Y., I. A. Shelykh, and I. V. Iorsh, 2021, "Two-dimensional chiral-waveguide quantum electrodynamics: Long-range qubit correlations and flat-band dark polaritons," Phys. Rev. A **103**, 033702.

Masson, S. J., I. Ferrier-Barbut, L. A. Orozco, A. Browaeys, and A. Asenjo-Garcia, 2020, "Many-Body Signatures of Collective Decay in Atomic Chains," Phys. Rev. Lett. **125**, 263601.

Mehrabad, M. J., A. P. Foster, R. Dost, E. Clarke, P. K. Patil, A. M. Fox, M. S. Skolnick, and L. R. Wilson, 2020, "Chiral topological photonics with an embedded quantum emitter," Optica **7**, 1690–1696.

Mirhosseini, M., E. Kim, V. S. Ferreira, M. Kalaee, A. Sipahigil, A. J. Keller, and O. Painter, 2018, "Superconducting metamaterials for waveguide quantum electrodynamics," Nat. Commun. **9**, 3706.

Mirhosseini, M., E. Kim, X. Zhang, A. Sipahigil, P. B. Dieterle, A. J. Keller, A. Asenjo-Garcia, D. E. Chang, and O. Painter, 2019, "Cavity quantum electrodynamics with atom-like mirrors," Nature (London) **569**, 692–697.

Mirza, I. M., J. G. Hoskins, and J. C. Schotland, 2017, "Chirality, band structure, and localization in waveguide quantum electrodynamics," Phys. Rev. A **96**, 053804.

Mirza, I. M., and J. C. Schotland, 2018, "Influence of disorder on electromagnetically induced transparency in chiral waveguide quantum electrodynamics," J. Opt. Soc. Am. B **35**, 1149.

Mitsch, R., C. Sayrin, B. Albrecht, P. Schneeweiss, and A. Rauschenbeutel, 2014, "Quantum state-controlled directional spontaneous emission of photons into a nanophotonic waveguide," Nat. Commun. **5**, 5713.

Mittal, S., E. A. Goldschmidt, and M. Hafezi, 2018, "A topological source of quantum light," Nature (London) **561**, 502–506.

Moreno-Cardoner, M., D. Goncalves, and D. E. Chang, 2021, "Quantum Nonlinear Optics Based on Two-Dimensional Rydberg Atom Arrays," Phys. Rev. Lett. **127**, 263602.

Muthukrishnan, A., G. S. Agarwal, and M. O. Scully, 2004, "Inducing Disallowed Two-Atom Transitions with Temporally Entangled Photons," Phys. Rev. Lett. **93**, 093002.

Nieddu, T., V. Gokhroo, and S. N. Chormaic, 2016, "Optical nanofibres and neutral atoms," J. Opt. **18**, 053001.

Niemczyk, T., *et al.*, 2010, "Circuit quantum electrodynamics in the ultrastrong-coupling regime," Nat. Phys. **6**, 772–776.

Noh, C., and D. G. Angelakis, 2017, "Quantum simulations and many-body physics with light," Rep. Prog. Phys. **80**, 016401.

Olmos, B., C. Liedl, I. Lesanovsky, and P. Schneeweiss, 2021, "Bragg condition for scattering into a guided optical mode," Phys. Rev. A **104**, 043517.

Omran, A., *et al.*, 2019, "Generation and manipulation of Schrödinger cat states in Rydberg atom arrays," Science **365**, 570–574.

Orús, R., 2014, "A practical introduction to tensor networks: Matrix product states and projected entangled pair states," Ann. Phys. (Amsterdam) **349**, 117–158.

Ozawa, T., *et al.*, 2019, "Topological photonics," Rev. Mod. Phys. **91**, 015006.

Paris-Mandoki, A., C. Braun, J. Kumlin, C. Tresp, I. Mirgorodskiy, F. Christaller, H. P. Büchler, and S. Hofferberth, 2017, "Free-Space Quantum Electrodynamics with a Single Rydberg Superatom," Phys. Rev. X **7**, 041010.

Patnaik, A. K., J. Q. Liang, and K. Hakuta, 2002, "Slow light propagation in a thin optical fiber via electromagnetically induced transparency," Phys. Rev. A **66**, 063808.

Perczel, J., J. Borregaard, D. E. Chang, H. Pichler, S. F. Yelin, P. Zoller, and M. D. Lukin, 2017, "Topological Quantum Optics in Two-Dimensional Atomic Arrays," Phys. Rev. Lett. **119**, 023603.

Perczel, J., J. Borregaard, D. E. Chang, S. F. Yelin, and M. D. Lukin, 2020, "Topological Quantum Optics Using Atomlike Emitter Arrays Coupled to Photonic Crystals," Phys. Rev. Lett. **124**, 083603.

Perczel, J., and M. D. Lukin, 2020, "Theory of dipole radiation near a Dirac photonic crystal," Phys. Rev. A **101**, 033822.

Peropadre, B., D. Zueco, D. Porras, and J. J. García-Ripoll, 2013, "Nonequilibrium and Nonperturbative Dynamics of Ultrastrong Coupling in Open Lines," Phys. Rev. Lett. **111**, 243602.

Piasotski, K., and M. Pletyukhov, 2021, "Diagrammatic approach to scattering of multiphoton states in waveguide QED," Phys. Rev. A **104**, 023709.

Pichler, H., and P. Zoller, 2016, "Photonic Circuits with Time Delays and Quantum Feedback," Phys. Rev. Lett. **116**, 093601.

Pivovarov, V., L. Gerasimov, J. Berroir, T. Ray, J. Laurat, A. Urvoy, and D. Kupriyanov, 2021, "Single collective excitation of an atomic array trapped along a waveguide: A study of cooperative emission for different atomic chain configurations," Phys. Rev. A **103**, 043716.

Pivovarov, V. A., A. S. Sheremet, L. V. Gerasimov, V. M. Porozova, N. V. Corzo, J. Laurat, and D. V. Kupriyanov, 2018, "Light scattering from an atomic array trapped near a one-dimensional nanoscale waveguide: A microscopic approach," Phys. Rev. A **97**, 023827.

Pletyukhov, M., and V. Gritsev, 2012, "Scattering of massless particles in one-dimensional chiral channel," New J. Phys. **14**, 095028.

Poddubny, A., and E. Ivchenko, 2013, "Resonant diffraction of electromagnetic waves from solids (a review)," Phys. Solid State **55**, 905–923.

Poddubny, A. N., 2020, "Quasiflat band enabling subradiant two-photon bound states," Phys. Rev. A **101**, 043845.

Poshakinskiy, A., A. Poddubny, L. Pilozzi, and E. Ivchenko, 2014, "Radiative Topological States in Resonant Photonic Crystals," Phys. Rev. Lett. **112**, 107403.

Poshakinskiy, A. V., and A. N. Poddubny, 2016, "Biexciton-mediated superradiant photon blockade," Phys. Rev. A **93**, 033856.

Poshakinskiy, A. V., and A. N. Poddubny, 2021, "Dimerization of Many-Body Subradiant States in Waveguide Quantum Electrodynamics," Phys. Rev. Lett. **127**, 173601.

Poshakinskiy, A. V., A. N. Poddubny, and S. A. Tarasenko, 2012, "Reflection of short polarized optical pulses from periodic and aperiodic multiple quantum well structures," Phys. Rev. B **86**, 205304.

Poshakinskiy, A. V., J. Zhong, Y. Ke, N. A. Olekhno, C. Lee, Y. S. Kivshar, and A. N. Poddubny, 2021, "Quantum Hall phases emerging from atom-photon interactions," npj Quantum Inf. **7**, 34.

Poshakinskiy, A. V., J. Zhong, and A. N. Poddubny, 2021, "Quantum Chaos Driven by Long-Range Waveguide-Mediated Interactions," Phys. Rev. Lett. **126**, 203602.

Prasad, A. S., J. Hinney, S. Mahmoodian, K. Hammerer, S. Rind, P. Schneeweiss, A. S. Sørensen, J. Volz, and A. Rauschenbeutel, 2020, "Correlating photons using the collective nonlinear response of atoms weakly coupled to an optical mode," Nat. Photonics **14**, 719.

Ramos, T., H. Pichler, A. J. Daley, and P. Zoller, 2014, "Quantum Spin Dimers from Chiral Dissipation in Cold-Atom Chains," Phys. Rev. Lett. **113**, 237203.

Rice, P., and H. Carmichael, 1988, "Single-atom cavity-enhanced absorption. I. Photon statistics in the bad-cavity limit," IEEE J. Quantum Electron. **24**, 1351–1366.

Richerme, P., Z.-X. Gong, A. Lee, C. Senko, J. Smith, M. Foss-Feig, S. Michalakis, A. V. Gorshkov, and C. Monroe, 2014, "Non-local propagation of correlations in quantum systems with long-range interactions," Nature (London) **511**, 198–201.

Rigetti, C., *et al.*, 2012, "Superconducting qubit in a waveguide cavity with a coherence time approaching 0.1 ms," Phys. Rev. B **86**, 100506.

Ringel, M., M. Pletyukhov, and V. Gritsev, 2014, "Topologically protected strongly correlated states of photons," New J. Phys. **16**, 113030.

Rodriguez-Fortuno, F. J., G. Marino, P. Ginzburg, D. O'Connor, A. Martinez, G. A. Wurtz, and A. V. Zayats, 2013, "Near-field interference for the unidirectional excitation of electromagnetic guided modes," Science **340**, 328–330.

Röhlsberger, R., and J. Evers, 2021, "Quantum optical phenomena in nuclear resonant scattering," in *Modern Mössbauer Spectroscopy*,

Topics in Applied Physics Vol. 137, edited by Y. Yoshida and G. Langouche (Springer Nature, Singapore), pp. 105–171, 10.1007/978-981-15-9422-9_3.

Röhlsberger, R., K. Schlage, B. Sahoo, S. Couet, and R. Rüffer, 2010, "Collective Lamb shift in single-photon superradiance," Science 328, 1248–1251.

Röhlsberger, R., H.-C. Wille, K. Schlage, and B. Sahoo, 2012, "Electromagnetically induced transparency with resonant nuclei in a cavity," Nature (London) 482, 199–203.

Rosario Hamann, A., C. Müller, M. Jerger, M. Zanner, J. Combes, M. Pletyukhov, M. Weides, T. M. Stace, and A. Fedorov, 2018, "Nonreciprocity Realized with Quantum Nonlinearity," Phys. Rev. Lett. 121, 123601.

Rotondo, P., M. Cosentino Lagomarsino, and G. Viola, 2015, "Dicke Simulators with Emergent Collective Quantum Computational Abilities," Phys. Rev. Lett. 114, 143601.

Roy, D., 2010, "Few-photon optical diode," Phys. Rev. B 81, 155117.

Roy, D., 2011, "Two-Photon Scattering by a Driven Three-Level Emitter in a One-Dimensional Waveguide and Electromagnetically Induced Transparency," Phys. Rev. Lett. 106, 053601.

Roy, D., 2013a, "Cascaded two-photon nonlinearity in a one-dimensional waveguide with multiple two-level emitters," Sci. Rep. 3, 2337.

Roy, D., 2013b, "Two-photon scattering of a tightly focused weak light beam from a small atomic ensemble: An optical probe to detect atomic level structures," Phys. Rev. A 87, 063819.

Roy, D., 2017, "Critical features of nonlinear optical isolators for improved nonreciprocity," Phys. Rev. A 96, 033838.

Roy, D., and N. Bondyopadhaya, 2014, "Statistics of scattered photons from a driven three-level emitter in a one-dimensional open space," Phys. Rev. A 89, 043806.

Roy, D., C. M. Wilson, and O. Firstenberg, 2017, "Colloquium: Strongly interacting photons in one-dimensional continuum," Rev. Mod. Phys. 89, 021001.

Royer, B., A. L. Grimsmo, A. Choquette-Poitevin, and A. Blais, 2018, "Itinerant Microwave Photon Detector," Phys. Rev. Lett. 120, 203602.

Rui, J., D. Wei, A. Rubio-Abadal, S. Hollerith, J. Zeiher, D. M. Stamper-Kurn, C. Gross, and I. Bloch, 2020, "A subradiant optical mirror formed by a single structured atomic layer," Nature (London) 583, 369.

Rupasov, V., and V. Yudson, 1984, "Exact Dicke superradiance theory: Bethe wavefunctions in the discrete atom model," Sov. Phys. JETP 59, 478, http://www.jetp.ras.ru/cgi-bin/e/index/e/59/3/p478?a=list.

Rybin, M. V., D. S. Filonov, K. B. Samusev, P. A. Belov, Y. S. Kivshar, and M. F. Limonov, 2015, "Phase diagram for the transition from photonic crystals to dielectric metamaterials," Nat. Commun. 6, 10102.

Sánchez-Burillo, E., L. Martín-Moreno, J. J. García-Ripoll, and D. Zueco, 2019, "Single Photons by Quenching the Vacuum," Phys. Rev. Lett. 123, 013601.

Sánchez-Burillo, E., D. Zueco, J. Garcia-Ripoll, and L. Martin-Moreno, 2014, "Scattering in the Ultrastrong Regime: Nonlinear Optics with One Photon," Phys. Rev. Lett. 113, 263604.

Saravi, S., A. N. Poddubny, T. Pertsch, F. Setzpfandt, and A. A. Sukhorukov, 2017, "Atom-mediated spontaneous parametric down-conversion in periodic waveguides," Opt. Lett. 42, 4724–4727.

Sayrin, C., C. Clausen, B. Albrecht, P. Schneeweiss, and A. Rauschenbeutel, 2015, "Storage of fiber-guided light in a nanofiber-trapped ensemble of cold atoms," Optica 2, 353.

Scarpelli, L., *et al.*, 2019, "99% beta factor and directional coupling of quantum dots to fast light in photonic crystal waveguides determined by spectral imaging," Phys. Rev. B 100, 035311.

Scheucher, M., A. Hilico, E. Will, J. Volz, and A. Rauschenbeutel, 2016, "Quantum optical circulator controlled by a single chirally coupled atom," Science 354, 1577–1580.

Schilke, A., C. Zimmermann, P. W. Courteille, and W. Guerin, 2011, "Photonic Band Gaps in One-Dimensionally Ordered Cold Atomic Vapors," Phys. Rev. Lett. 106, 223903.

Schneider, M. P., T. Sproll, C. Stawiarski, P. Schmitteckert, and K. Busch, 2016, "Green's-function formalism for waveguide QED applications," Phys. Rev. A 93, 013828.

Scholl, P., *et al.*, 2021, "Quantum simulation of 2D antiferromagnets with hundreds of Rydberg atoms," Nature (London) 595, 233–238.

Schollwöck, U., 2011, "The density-matrix renormalization group in the age of matrix product states," Ann. Phys. (Amsterdam) 326, 96–192.

Sedov, D. D., V. K. Kozin, and I. V. Iorsh, 2020, "Chiral Waveguide Optomechanics: First Order Quantum Phase Transitions with Z_3 Symmetry Breaking," Phys. Rev. Lett. 125, 263606.

Shahmoon, E., and G. Kurizki, 2013, "Nonradiative interaction and entanglement between distant atoms," Phys. Rev. A 87, 033831.

Shahmoon, E., D. S. Wild, M. D. Lukin, and S. F. Yelin, 2017, "Cooperative Resonances in Light Scattering from Two-Dimensional Atomic Arrays," Phys. Rev. Lett. 118, 113601.

Shen, J.-T., and S. Fan, 2007a, "Strongly correlated multiparticle transport in one dimension through a quantum impurity," Phys. Rev. A 76, 062709.

Shen, J.-T., and S. Fan, 2007b, "Strongly Correlated Two-Photon Transport in a One-Dimensional Waveguide Coupled to a Two-Level System," Phys. Rev. Lett. 98, 153003.

Shi, T., D. E. Chang, and J. I. Cirac, 2015, "Multiphoton-scattering theory and generalized master equations," Phys. Rev. A 92, 053834.

Shi, T., Y. Chang, and J. J. García-Ripoll, 2018, "Ultrastrong Coupling Few-Photon Scattering Theory," Phys. Rev. Lett. 120, 153602.

Shi, T., S. Fan, and C. P. Sun, 2011, "Two-photon transport in a waveguide coupled to a cavity in a two-level system," Phys. Rev. A 84, 063803.

Shi, T., and C. P. Sun, 2009, "Lehmann-Symanzik-Zimmermann reduction approach to multiphoton scattering in coupled-resonator arrays," Phys. Rev. B 79, 205111.

Shi, T., Y.-H. Wu, A. González-Tudela, and J. I. Cirac, 2018, "Effective many-body Hamiltonians of qubit-photon bound states," New J. Phys. 20, 105005.

Shi, Y., Z. Yu, and S. Fan, 2015, "Limitations of nonlinear optical isolators due to dynamic reciprocity," Nat. Photonics 9, 388–392.

Silbey, R., and R. A. Harris, 1984, "Variational calculation of the dynamics of a two level system interacting with a bath," J. Chem. Phys. 80, 2615–2617.

Simovski, C. R., P. A. Belov, and M. S. Kondratjev, 1999, "Electromagnetic interaction of chiral particles in three-dimensional arrays," J. Electromagn. Waves Appl. 13, 189.

Sinev, I. S., A. A. Bogdanov, F. E. Komissarenko, K. S. Frizyuk, M. I. Petrov, I. S. Mukhin, S. V. Makarov, A. K. Samusev, A. V. Lavrinenko, and I. V. Iorsh, 2017, "Chirality driven by magnetic dipole response for demultiplexing of surface waves," Laser Photonics Rev. 11, 1700168.

Sipahigil, A., *et al.*, 2016, "An integrated diamond nanophotonics platform for quantum-optical networks," Science 354, 847–850.

Skoff, S. M., D. Papencordt, H. Schauffert, B. C. Bayer, and A. Rauschenbeutel, 2018, "Optical-nanofiber-based interface for single molecules," Phys. Rev. A **97**, 043839.

Smilansky, U., 2004, "Irreversible quantum graphs," Waves Random Media **14**, S143–S153.

Solano, P., P. Barberis-Blostein, F. K. Fatemi, L. A. Orozco, and S. L. Rolston, 2017, "Super-radiance reveals infinite-range dipole interactions through a nanofiber," Nat. Commun. **8**, 1857.

Söllner, I., *et al.*, 2015, "Deterministic photon-emitter coupling in chiral photonic circuits," Nat. Nanotechnol. **10**, 775–778.

Solomons, Y., and E. Shahmoon, 2021, "Multi-channel waveguide QED with atomic arrays in free space," arXiv:2111.1151.

Song, C., *et al.*, 2019, "Generation of multicomponent atomic Schrödinger cat states of up to 20 qubits," Science **365**, 574–577.

Song, G.-Z., J.-L. Guo, W. Nie, L.-C. Kwek, and G.-L. Long, 2021, "Optical properties of a waveguide-mediated chain of randomly positioned atoms," Opt. Express **29**, 1903–1917.

Song, G.-Z., L.-C. Kwek, F.-G. Deng, and G.-L. Long, 2019, "Microwave transmission through an artificial atomic chain coupled to a superconducting photonic crystal," Phys. Rev. A **99**, 043830.

Song, G.-Z., E. Munro, W. Nie, F.-G. Deng, G.-J. Yang, and L.-C. Kwek, 2017, "Photon scattering by an atomic ensemble coupled to a one-dimensional nanophotonic waveguide," Phys. Rev. A **96**, 043872.

Song, G.-Z., E. Munro, W. Nie, L.-C. Kwek, F.-G. Deng, and G.-L. Long, 2018, "Photon transport mediated by an atomic chain trapped along a photonic crystal waveguide," Phys. Rev. A **98**, 023814.

Sørensen, H. L., J.-B. Béguin, K. W. Kluge, I. Iakoupov, A. S. Sørensen, J. H. Müller, E. S. Polzik, and J. Appel, 2016, "Coherent Backscattering of Light off One-Dimensional Atomic Strings," Phys. Rev. Lett. **117**, 133604.

Spitzer, F., *et al.*, 2018, "Routing the emission of a near-surface light source by a magnetic field," Nat. Phys. **14**, 1043–1048.

Srakaew, K., P. Weckesser, S. Hollerith, D. Wei, D. Adler, I. Bloch, and J. Zeiher, 2023, "A subwavelength atomic array switched by a single Rydberg atom," Nat. Phys. **27**, 864.

Stannigel, K., P. Rabl, and P. Zoller, 2012, "Driven-dissipative preparation of entangled states in cascaded quantum-optical networks," New J. Phys. **14**, 063014.

Stiesdal, N., H. Busche, K. Kleinbeck, J. Kumlin, M. G. Hansen, H. P. Büchler, and S. Hofferberth, 2021, "Controlled multi-photon subtraction with cascaded Rydberg superatoms as single-photon absorbers," Nat. Commun. **12**, 4328.

Stiesdal, N., J. Kumlin, K. Kleinbeck, P. Lunt, C. Braun, A. Paris-Mandoki, C. Tresp, H. P. Büchler, and S. Hofferberth, 2018, "Observation of Three-Body Correlations for Photons Coupled to a Rydberg Superatom," Phys. Rev. Lett. **121**, 103601.

Strack, P., and S. Sachdev, 2011, "Dicke Quantum Spin Glass of Atoms and Photons," Phys. Rev. Lett. **107**, 277202.

Taubert, R., D. Dregely, T. Stroucken, A. Christ, and H. Giessen, 2012, "Octave-wide photonic band gap in three-dimensional plasmonic Bragg structures and limitations of radiative coupling," Nat. Commun. **3**, 691.

Thyrrestrup, H., *et al.*, 2018, "Quantum optics with near-lifetime-limited quantum-dot transitions in a nanophotonic waveguide," Nano Lett. **18**, 1801–1806.

Tsvelick, A., and P. Wiegmann, 1983, "Exact results in the theory of magnetic alloys," Adv. Phys. **32**, 453–713.

Türschmann, P., H. L. Jeannic, S. F. Simonsen, H. R. Haakh, S. Götzinger, V. Sandoghdar, P. Lodahl, and N. Rotenberg, 2019, "Coherent nonlinear optics of quantum emitters in nanophotonic waveguides," Nanophotonics **8**, 1641–1657.

Uppu, R., L. Midolo, X. Zhou, J. Carolan, and P. Lodahl, 2021, "Quantum-dot-based deterministic photon-emitter interfaces for scalable photonic quantum technology," Nat. Nanotechnol. **16**, 1308–1317.

van Loo, A. F., A. Fedorov, K. Lalumiere, B. C. Sanders, A. Blais, and A. Wallraff, 2013, "Photon-mediated interactions between distant artificial atoms," Science **342**, 1494–1496.

Vermersch, B., T. Ramos, P. Hauke, and P. Zoller, 2016, "Implementation of chiral quantum optics with Rydberg and trapped-ion setups," Phys. Rev. A **93**, 063830.

Versteegh, M., M. E. Reimer, K. D. Jöns, D. Dalacu, P. J. Poole, A. Gulinatti, A. Giudice, and V. Zwiller, 2014, "Observation of strongly entangled photon pairs from a nanowire quantum dot," Nat. Commun. **5**, 5298.

Vetsch, E., D. Reitz, G. Sagué, R. Schmidt, S. Dawkins, and A. Rauschenbeutel, 2010, "Optical Interface Created by Laser-Cooled Atoms Trapped in the Evanescent Field Surrounding an Optical Nanofiber," Phys. Rev. Lett. **104**, 203603.

Vigman, P. B., 1980, "Exact solution of *s-d* exchange model at $T = 0$," JETP Lett. **31**, 364, http://jetpletters.ru/ps/1353/article_20434.shtml.

Vinu, A., and D. Roy, 2020, "Amplification and cross-Kerr nonlinearity in waveguide quantum electrodynamics," Phys. Rev. A **101**, 053812.

Vladimirova, M. R., E. L. Ivchenko, and A. V. Kavokin, 1998, "Exciton polaritons in long-period quantum-well structures," Semiconductors **32**, 90–95.

Voronov, M., E. Ivchenko, M. Erementchouk, L. Deych, and A. Lisyansky, 2007, "Photoluminescence spectroscopy of one-dimensional resonant photonic crystals," J. Lumin. **125**, 112–117.

Wall, M. L., A. Safavi-Naini, and A. M. Rey, 2016, "Simulating generic spin-boson models with matrix product states," Phys. Rev. A **94**, 053637.

Walls, D. F., and G. J. Milburn, 2007, *Quantum Optics* (Springer Science+Business Media, New York).

Wang, D.-W., R.-B. Liu, S.-Y. Zhu, and M. O. Scully, 2015, "Superradiance Lattice," Phys. Rev. Lett. **114**, 043602.

Wang, Z., T. Jaako, P. Kirton, and P. Rabl, 2020, "Supercorrelated Radiance in Nonlinear Photonic Waveguides," Phys. Rev. Lett. **124**, 213601.

Windpassinger, P. J., D. Oblak, P. G. Petrov, M. Kubasik, M. Saffman, C. L. G. Alzar, J. Appel, J. H. Müller, N. Kjærgaard, and E. S. Polzik, 2008, "Nondestructive Probing of Rabi Oscillations on the Cesium Clock Transition near the Standard Quantum Limit," Phys. Rev. Lett. **100**, 103601.

Xu, S., and S. Fan, 2015, "Input-output formalism for few-photon transport: A systematic treatment beyond two photons," Phys. Rev. A **91**, 043845.

Yanik, M. F., W. Suh, Z. Wang, and S. Fan, 2004, "Stopping Light in a Waveguide with an All-Optical Analog of Electromagnetically Induced Transparency," Phys. Rev. Lett. **93**, 233903.

Yılmaz, S. T., P. Fallahi, and A. Imamoğlu, 2010, "Quantum-Dot-Spin Single-Photon Interface," Phys. Rev. Lett. **105**, 033601.

Yudson, V. I., 1985, "Dynamics of integrable quantum systems," Sov. Phys. JETP **61**, 1043, http://www.jetp.ras.ru/cgi-bin/e/index/e/61/5/p1043?a=list.

Yudson, V. I., and P. Reineker, 2008, "Multiphoton scattering in a one-dimensional waveguide with resonant atoms," Phys. Rev. A **78**, 052713.

Yugova, I. A., M. M. Glazov, E. L. Ivchenko, and A. L. Efros, 2009, "Pump-probe Faraday rotation and ellipticity in an ensemble of singly charged quantum dots," Phys. Rev. B **80**, 104436.

Zanner, M., T. Orell, C. M. F. Schneider, R. Albert, S. Oleschko, M. L. Juan, M. Silveri, and G. Kirchmair, 2022, "Coherent control of a multi-qubit dark state in waveguide quantum electrodynamics," Nat. Phys. **18**, 538–543.

Zhang, L., V. Walther, K. Mølmer, and T. Pohl, 2022, "Photon-photon interactions in Rydberg-atom arrays," Quantum **6**, 674.

Zhang, Y.-X., and K. Mølmer, 2019, "Theory of Subradiant States of a One-Dimensional Two-Level Atom Chain," Phys. Rev. Lett. **122**, 203605.

Zhang, Y.-X., and K. Mølmer, 2020, "Subradiant Emission from Regular Atomic Arrays: Universal Scaling of Decay Rates from the Generalized Bloch Theorem," Phys. Rev. Lett. **125**, 253601.

Zhang, Y.-X., C. Yu, and K. Mølmer, 2020, "Subradiant bound dimer excited states of emitter chains coupled to a one dimensional waveguide," Phys. Rev. Res. **2**, 013173.

Zheng, H., and H. U. Baranger, 2013, "Persistent Quantum Beats and Long-Distance Entanglement from Waveguide-Mediated Interactions," Phys. Rev. Lett. **110**, 113601.

Zhong, J., N. A. Olekhno, Y. Ke, A. V. Poshakinskiy, C. Lee, Y. S. Kivshar, and A. N. Poddubny, 2020, "Photon-Mediated Localization in Two-Level Qubit Arrays," Phys. Rev. Lett. **124**, 093604.

Zhong, J., and A. N. Poddubny, 2021, "Classification of three-photon states in waveguide quantum electrodynamics," Phys. Rev. A **103**, 023720.